

# FLOW BEHAVIOUR AND FRICTIONAL CHARACTERISTICS OF SUPERCRITICAL CARBON DIOXIDE IN VANELESS RADIAL AND CONICAL DIFFUSERS

## Master Thesis

Delft University of Technology Faculty of Aerospace Engineering Propulsion and Power Delft, June 2025

Author:

Mateusz Dabrowski \*

Supervisors:

Prof. Matteo Pini \* Prof. Jürg Schiffmann †

Advisor:

Konstantin Jacoby †



\* Delft University of Technology † École Polytechnique Fédérale de Lausanne

The night stared me in the face, amorphous, blind, infinite, without frontiers. Not a single start relieved the darkness behind the glass.

–Stanislaw Lem, Solaris

#### ACKNOWLEDGMENT

I would like to express my sincere gratitude to EPFL and the LAMD laboratory for the opportunity to conduct my research within their facilities. Being part of such a dynamic and intellectually stimulating environment has been a rewarding experience. The collaborative spirit and valuable input from many researchers in the lab significantly supported my progress and enriched the quality of this work. I am particularly grateful to Prof. Jürg Schiffmann for hosting me at the laboratory during the course of my thesis.

I also wish to extend my heartfelt appreciation to my supervisor from my home university, TU Delft, Prof. Matteo Pini, for his scientific expertise, insightful feedback, and continuous guidance throughout this project. His constructive input helped shape the direction of the research and strengthened the academic quality of the final outcome.

Most importantly, I am deeply thankful to my advisor, Konstantin Jacoby, whose unwavering support, insightful mentorship, and encouragement were instrumental to the successful completion of this thesis. His patience, technical guidance, and consistent engagement throughout the project have been invaluable, and I am truly grateful for the opportunity to work under his supervision.



### Abstract

This thesis investigates the performance of vaneless radial and conical diffusers operating with supercritical carbon dioxide (SC-CO2) under various geometric configurations. The motivation arises from the growing interest in compact, high-efficiency turbomachinery suitable for supercritical fluid cycles. The study employs a combination of one-dimensional modelling (1D) and computational fluid dynamics (CFD) to analyse pressure recovery in view of frictional effects and flow separation. All the CFD simulations were conducted using commercial software Ansys CFX 2024 and 2025 integrated into Ansys Workbench (3) and all the coding, including 1D modelling and post-processing was done with Matlab 2024. The performance of SC-CO2 operating diffusers was compared against air simulations at ambient conditions at matched Mach regime. The results show the advantageous pressure recovery of SC-CO2. Furthermore, the comparison between 1D and CFD modelling shows acceptable agreement for low expanding diffusers but reveals significant deviations in outcomes close to separated flow conditions.



# Contents

| A        | ckno                   | wledgements   | iii           |
|----------|------------------------|---|---------------|
| Su       | ımm                    | ary   | v             |
| Li       | $\operatorname{st}$ of | Figures   | х             |
| Li       | ${ m st}$ of           | Tables  | xi            |
| Li       | ${ m st}$ of           | Symbols   | xi            |
| 1        | Intr                   | roduction   | 1             |
|          | 1.1                    | Motivation and Background                             | 1             |
|          |                        | 1.1.1 Role of a diffuser                              | $\frac{1}{2}$ |
|          |                        | 1.1.3 Introduction to supercritical CO2               | 6             |
|          | 1.2                    | Nature of the issue                                   | 7             |
|          |                        | 1.2.1 Gas modelling                                   | 7             |
|          |                        | 1.2.2 Diffuser performance modelling                  | 8             |
|          | 1.3                    | Objectives and Scope                                  | 10            |
| <b>2</b> | Met                    | thodology   | 11            |
|          | 2.1                    | Diffuser terminology and assessment                   | 11            |
|          | 2.2                    | 1D Meanline Model                                     | 11            |
|          |                        | 2.2.1 Frictional effects                              | 11            |
|          |                        | 2.2.2 Separation prediction                           | 13            |
|          | 2.3                    | CFD model   | 14            |
| 3        | Res                    | sults and Discussions                                 | 17            |
|          | 3.1                    | 1D Model  | 17            |
|          |                        | 3.1.1 Conical diffuser                                | 17            |
|          |                        | 3.1.2 Radial diffuser                                 | 20            |
|          | 3.2                    | CFD   | 22            |
|          |                        | 3.2.1 Conical diffuser                                | 23            |
|          |                        | 3.2.2 Conical geometry based study SC-CO2 vs. Air     | 28            |
|          |                        | 3.2.3 Radial diffuser                                 | 30            |
|          |                        | 3.2.4 Effect of Inlet Flow Angle on Pressure Recovery | 34            |
|          |                        | 3.2.5 Radial geometry based study SC-CO2 vs. Air      | 35            |
|          | 3.3                    | 1D vs. CFD Performance Prediction Comparison          | 36            |
|          |                        | 3.3.1 Friction Coefficient in Axial Flow              | 36            |
|          |                        | 3.3.2 Conical geometry based study 1D vs. CFD         | 38            |
|          |                        | 3.3.3 Friction Coefficient in Radial Flow             | 39            |
|          |                        | 3.3.4 Radial geometry based study 1D vs CFD           | 40            |
| 4        | Fina                   | al thoughts on modelling assessment                   | 42            |
|          | 4.1                    | 1D Model Assessment                                   | 42            |
|          | 4.2                    | CFD Model Assessment                                  | 43            |
| 5        | Cor                    | nclusions and Suggestions                             | 44            |

| 1  | _   |    |      |      |    |   |
|----|-----|----|------|------|----|---|
| ι, | ( ) | Ν΄ | L.H. | ; IN | T۶ | • |

| <b>TU</b> Delft  | ΞP |   |
|------------------|----|---|
| <b>I U</b> Delft |    | ļ |

| A            | Ideal Pressure Recovery            | 47         |
|--------------|------------------------------------|------------|
| В            | Cross-sectional area in diffusers  | 48         |
| $\mathbf{C}$ | Stanitz Radial Diffuser Flow Model | 48         |
| D            | Use of non-ideal gas model         | 49         |
| ${f E}$      | Idealised Real Gas                 | <b>5</b> 0 |
| $\mathbf{F}$ | Stratford criterion                | 51         |
| $\mathbf{G}$ | CFD                                | <b>5</b> 4 |
|              | G.1 Conical diffuser               | 54         |
|              | G 2 Radial diffuser                | 55         |



# LIST OF FIGURES

| 1.1  | Deflecting streamline in radial diffuser flow   | 2   |
|------|---|-----|
| 1.2  | A Adverse pressure profile along surface. B Corresponding boundary layer velocity   | c   |
| 1.3  | profiles  | 6   |
| 1.5  | from Renau et al. with permission $(20)$  | 6   |
| 1.4  | Magnitude of compressibility factor $Z$ as a function of thermodynamic conditions.  | Ü   |
|      | Adopted from Guardone et al. under CC BY 4.0.(13)   | 7   |
| 1.5  | Outlet properties of isentropic SC-CO2 flow with inlet at $T=305$ [K], $p=74$ [bar] and $M=0.5$ evaluated with different gas models as a function of area ratio. <b>A</b> shows the magnitude of density variation and <b>B</b> shows the non-dimensionalised values against inlet conditions   | 8   |
| 2.1  | Sketches of diffuser geometries with parametrisation, shown with side and cross-section views. (A) Conical diffuser with radii and length denoted as R in, R out and L shown with blue arrows indicating direction of streamlines entering and leaving. (B.1) Radial diffuser with radii and widths denoted as R in, R out, B in and B out shown with blue arrows indicating direction of streamlines entering and leaving, and red lines indicating streamlines within the diffuser. |     |
|      | (B.2) Definition of inlet flow angle in radial diffuser   | 12  |
| 2.2  | Flowchart of the 1D meanline model routine for evaluating flow properties   | 13  |
| 2.3  | Barotropic models polytropic efficiency (A) Conical and (B) Radial diffuser   | 15  |
| 2.4  | An example of a mesh used for CFD simulation of a conical diffuser  | 16  |
| 2.5  | An example of a mesh used for CFD simulation of a radial diffuser   | 16  |
| 3.1  | Results from the 1D meanline model of SC-CO2 for a conical diffusers with length $NW=3$ , using the friction correlation from Fang (2012). Inlet conditions are: velocity $V_{\rm in}=58.3[{\rm m/s}]$ , pressure $P_{\rm in}=80.1[{\rm bar}]$ , and temperature $T_{\rm in}=310[{\rm K}]$ . The plots illustrate: ( <b>A</b> ) Static pressure, ( <b>B</b> ) Velocity, ( <b>C</b> ) Total pressure, and ( <b>D</b> ) Entropy   |     |
| 3.2  | distributions along the diffuser  | 18  |
|      | permission $(20)$   | 19  |
| 3.3  | Results from the 1D meanline model of SC-CO2 for radial diffusers with length $NW = 5.42$ , using the friction correlation from Wang (2014). Inlet conditions are: velocity $C_{\rm in} = 135  [{\rm m/s}]$ , pressure $P_{\rm in} = 130.71  [{\rm bar}]$ , and temperature $T_{\rm in} = 364  [{\rm K}]$ . The plots illustrate: ( <b>A</b> ) Static pressure, ( <b>B</b> ) Velocity, ( <b>C</b> ) Total pressure, and ( <b>D</b> ) Entropy  | 10  |
|      | distributions along the diffuser  | 20  |
| 3.4  | Separation in a radial channel - red dot indicates stall and green lack of stall  | 22  |
| 3.5  | Boundary conditions for CFD simulations   | 23  |
| 3.6  | SC-CO2 flows in conical diffusers with $NW=3$ and fully attached $AR=1.6$ (1) and   |     |
|      | separated $AR = 3$ (2). Fields of: Pressure (A), Velocity (B)   | 24  |
| 3.7  | SC-CO2 flows in conical diffusers with $NW=3$ and fully attached $AR=1.6$ (1) and   |     |
|      | separated $AR = 3$ (2). Field of Total Pressure (C)   | 25  |
| 3.8  | SC-CO2 CFD Results for NW = 3 at the middle of the profile. Plots of: (A) Pressure,   |     |
|      | (B) Velocity, (C) Total Pressure where dashed line is mass-flow-averaged and solid is   | 2.0 |
| 0.0  | area-averaged result  | 26  |
| 3.9  | CFD Parametric study for $M_{in} = 0.3$ (A) SC-CO2 and (B) Air  | 28  |
| 3.10 | [ 9]  |     |
|      | = 1.00 (1) and separated AR = 2.00 (2). Fields of: (A) Pressure, (B) Velocity, (C)  | 91  |
|      | Total Pressure. Black and red lines are flow 2D and 3D streamlines respectively   | 31  |



| 3.11 | SC-CO2 CFD Results for $NW = 5.42$ at the centreline of the profile. Plots of: (A)   |    |
|------|--|----|
|      | Pressure, (B) Velocity, (C) Total Pressure where dashed line is mass-flow-averaged and   |    |
|      | solid is area-averaged result  | 33 |
| 3.12 | Effect of inlet angle $\alpha_{in}$ on pressure coefficient in radial diffuser with AR = 1 and   |    |
|      | $NW = 5.42 \dots \dots$  | 35 |
| 3.13 | CFD Parametric study for $M_{in}=0.5$ at $\alpha_{in}=65[\deg]$ (A) SC-CO2 and (B) Air   | 35 |
| 3.14 | Comparison of friction coefficient $Cf$ along a pipe for SC-CO2 flow. Result CFD 1   |    |
|      | calculates $Cf$ from the total pressure drop between monitoring stations, while CFD  |    |
|      | Case 2 derives $Cf$ from the wall shear stress. Additional $Cf$ values were obtained   |    |
|      | using friction models from literature, based on the same inlet flow conditions as the  |    |
|      | CFD simulations  | 37 |
| 3.15 | Pressure recovery as a function of AR, comparison with 1D model results with $Cf$  |    |
|      | models from literature. (A) $NW = 3$ (B) $NW = 5$  | 38 |
| 3.16 | Comparison of friction coefficient $Cf$ along radius of radial diffuser for SC-CO2 flow.   |    |
|      | Result CFD derives $Cf$ from the wall shear stress. Additional $Cf$ values were obtained   |    |
|      | using friction models from literature, based on the same inlet flow conditions as the  |    |
|      | CFD simulations  | 39 |
| 3.17 | Pressure recovery as a function of AR at $\alpha_{in} = 65[\text{deg}]$ , comparison with 1D model   |    |
|      | results with Cf models from literature.( $\mathbf{A}$ ) NW = 5.42 ( $\mathbf{B}$ ) NW = 6.25   | 40 |
| 3.18 | Pressure recovery as a function of AR, CFD comparison with 1D model results with a   |    |
|      | new Cf model.( $\mathbf{A}$ ) NW = 5.42 ( $\mathbf{B}$ ) NW = 6.25   | 41 |
| G.1  | SC-CO2 (in green) and Air (in blue) flows comparison of CFD results (A) Inlet Alpha  |    |
|      | $= 70[\deg], (\mathbf{B}) \text{ Inlet Alpha} = 73.8[\deg].  \dots $ | 56 |



# LIST OF TABLES

| 3.1 | Conical diffuser   | 23 |
|-----|--|----|
| 3.2 | Radial diffuser  | 23 |
| 3.3 | Conical Diffuser inlet properties for selected design points | 23 |
| 3.4 | Radial Diffuser Alpha = $65[\deg]$ inlet properties          | 30 |



## LIST OF SYMBOLS

 $C_r$ radial velocity component [m/s]  $C_{\theta}$ tangential velocity component [m/s] Cabsolute velocity in radial flow [m/s] Henthalpy [J] MaMach number [ - ] ReReynolds number [ - ] Uinternal energy [J] Vabsolute velocity in axial flow [m/s] β Stratford empirical factor [-] Relative roughness [-]  $\frac{\epsilon}{D}$ dynamic viscosity [Pa  $\cdot s$ ]  $\mu$ kinematic viscosity [m<sup>2</sup>/s]  $\nu$ boundary layer power coefficient [-] npressure [bar] pdensity  $[kg/m^3]$ ρ shear stress [Pa]  $\tau$ x component velocity [m/s] uARarea ratio [ - ] AArea [m<sup>2</sup>] Ddiameter [m] Llength [m] NWlength to width ratio [ - ] RRradius outlet to inlet ratio [ - ] diffuser radius [m] Rbdiffuser width [m] radial coordinate [m] r $\theta$ tangential coordinate [rad] x coordinate [m]  $\boldsymbol{x}$ y coordinate [m] y



## 1 Introduction

This work is a part of research stream focusing on supecritical carbon dioxide (SC-CO2) applications in turbomachinery. In this study, the non-ideal characteristics of the SC-CO2 were addressed and plausible ways of simulating a turbomachinery component - diffuser, examined. The current paper is split into five sections. The first, current one, presents fundamentals of diffuser operations and non-ideal compressible fluid dynamics. It outlines also the key challenges of simulating SC-CO2 diffusers. The second section, Methodology, describes what was done to alleviate the challenges of SC-CO2. It presents two modelling methods, one dimensional modelling (1D model) and full application of Navier-Stokes equations via CFD. The third section, Results and Discussions, portrays what was achieved with the two models and how they compare. In the fourth section, final thoughts on the models are given, where they are critically assessed. Finally, in Conclusions and Suggestions, what ensues from the study is explained and what are recommendations for future research in this domain.

#### 1.1 MOTIVATION AND BACKGROUND

In modern times, the threat of global warming and its consequences significantly shape our technology. With the current emphasis on producing more efficient and less polluting designs, supercritical carbon dioxide (SC-CO2) cycles have emerged as a promising alternative to conventional power generation or heat pumps. Due to the unique properties of SC-CO2 fluid, supercritical thermodynamic cycles offer high thermal efficiency, high power density, and compact infrastructure requirements, making single-stage turbines or pumps feasible (11). Notably, the application of SC-CO2 is being pursued in heat pumps, nuclear engineering, and enhanced oil recovery processes.

Despite the great potential of SC-CO2 for reducing the carbon footprint, its application is unfortunately hindered by challenges in the design process. The same characteristics that make SC-CO2 attractive also make it difficult to model in turbomachinery, where in some cases the working fluid has even been assumed to be incompressible (15).

In the spirit of addressing some of these challenges, the present work is undertaken. It re-examines diffuser modelling and provides insight into the flow phenomena inherent to SC-CO2 that will influence the design process.

#### 1.1.1 Role of a diffuser

A diffuser, whether conical or radial, is an inherent part of a compressor system. Whereas an impeller adds energy to the flow by rotating, increasing the flow's velocity, and as such increasing the total properties of the fluid, a diffuser is tasked with recovering as much static pressure from the flow as possible. It converts part of the flow's energy contained in its kinetic movement into other form of energy, embedded in pressure. This exchange is possible thanks to the flow expansion and deceleration in changing cross-sectional area of a diffuser. Thermodynamic cycles rely on high pressures at which heat is added to achieve better performance. Thus, achieving high pressure by a diffuser is crucial to their operation.

In this work two types of diffusers were considered - conical and vanless radial. The conical diffuser has fully axial inflow and the flow travels through a cylindrical geometry with increasing diameter. The radial diffuser, in its simplest form, resembles a disc. The flow enters through the direction of origin of that disk and leaves outwards in the plane of the disk in each direction. The two geometries are presented in the Figure 2.1.



#### 1.1.2 Fundamentals of Diffuser Operation

As seen in Figure 2.1, diffusers are passages with increasing cross-sectional areas. They manipulate the flow through their shape to make it expand and slow down. The deceleration leads to increase in pressure as governed by momentum conservation equation, which for inviscid flow can be simplified to Euler equation(2):

$$dp = -\rho V dV. (1.1)$$

By further introducing incompressibility assumption it can be simplified to Bernoulli equation:

$$p + \frac{1}{2}\rho V^2 = const. \tag{1.2}$$

The sum of the Bernoulli equation is equal to total (or stagnation) pressure in incompressible flow, denoted by  $P_0$ . By analogy, the first term p is referred to as static pressure and the second  $\frac{1}{2}\rho V^2$  dynamic pressure. Together, they show that increase in one will result in decrease in the other. This relation is the fundamental principle behind diffuser operation. For a case where flow has no losses, no work nor heat addition the value of  $P_0$  remains constant along a streamline (or in special cases entire flow domain).

Using the Equation 1.2 together with continuity equation, an expression for ideal pressure recovery in inviscid, incompressible flow can be analytically derived. For ease of comparison of diffuser performance, the magnitude of pressure recovered is non dimensionalised via use of pressure coefficient Cp defined in Equation 1.3.

$$Cp = \frac{p - p_{\infty}}{\frac{1}{2}\rho_{\infty}V_{\infty}^2} \tag{1.3}$$

Using this definition, in a conical diffuser, Cp is a function of only final to initial area ratio - AR:

$$Cp_{ideal} = 1 - \frac{1}{AR^2} \tag{1.4}$$

The relation for radial diffuser is different due to the flow inlet angle  $\alpha_{in}$ . As the flow swirls inside a radial diffuser, the flow angle  $\alpha$  changes, shown in the Figure 1.1.

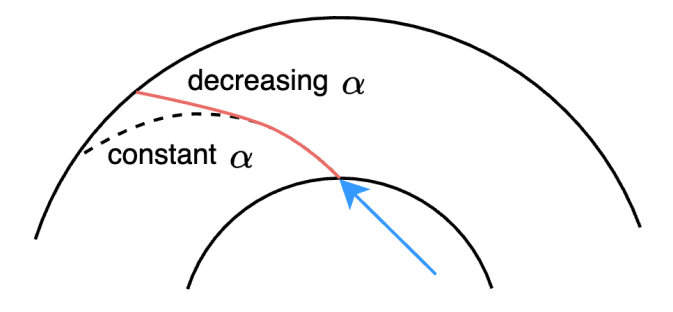
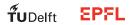


Figure 1.1: Deflecting streamline in radial diffuser flow

By recalling continuity equation in radial flow:

$$\dot{m} = \rho C \cos \alpha A \tag{1.5}$$

where  $\cos \alpha A$  is the effective area, it becomes clear that the velocity C decreases not only due to increasing A, but also due to decreasing  $\alpha$ . Moreover, the longer the diffuser, the higher the deflection of the streamline will be. Thus, the Cp in radial diffuser needs to capture the effect of the length of the passage, hence Equation 1.6.



$$Cp_{ideal} = cos^{2}(\alpha_{in})(1 - \frac{1}{AR^{2}}) + sin^{2}(\alpha_{in})(1 - \frac{1}{RR^{2}})$$
 (1.6)

If the inlet  $\alpha_{in}$  reduces to  $\alpha_{in} = 0^{\circ}$  the Cp becomes the same expression found for conical diffuser.

However, in real operation of a diffuser, losses do occur and cannot be neglected in a design. They result in decrease of  $P_0$ , rendering Equation 1.2 inadequate. The losses in diffusers, specifically vanless radial ones, can be classified based on their origin (17):

- Wake mixing losses
- Secondary flow losses
- Boundary layer losses.

Starting with the first category, wake mixing losses relate to mixing of jet and wake flows leaving the impeller. One, is the stream that leaves the pressure side of the impeller blade and the other the suction side. After those two streams mix, the flow is considered to be mixed out. Simplified models assume a fixed mass flow ratio between streams and solve for the mixed out state (28). Although mixing is a very pertinent loss mechanism in diffuser study, it occurs rapidly after impeller discharge (25) and depends strongly on rotor geometry (17). Accurately capturing this would require additional assumptions. Therefore, in this study, the flow entering the diffuser is assumed to be fully mixed.

The second type of losses, being secondary flow, relates again to the discharge of the impeller. Due to non-uniform distribution of velocity the flow will engage in secondary vorticity. This will have an effect on boundary layer thickness, however, as it also depends on the geometry of the impeller, in this work is omitted.

Lastly, the boundary layer losses, relate to all aspects that occur due to the boundary layer formation. Thus, the primary effects of viscosity are covered by this category. Those mechanisms can be further divided into friction and separation. In design of a diffuser, those are the leading considerations. Assuming a diffuser inlet flow is uniform, the friction and separation are the major effects on the diffuser performance and are hence the core of this research. Thus, a brief explanation of both is provided below.

#### **Friction**

Friction effects, as mentioned before, are actually due to viscosity. In real flow, due to interaction with a surface such as diffuser wall, a boundary layer will develop. The flow velocity at the wall is always assumed to be zero (called no-slip condition) and due to effect of viscosity the next streamline cannot already have the velocity of the flow due to shear stresses experienced from the layer of fluid at zero velocity. The shear stress for laminar flow, denoted as  $\tau$ , is directly proportional to viscosity and is given by:

$$\tau = \mu \frac{\delta u}{\delta y} \tag{1.7}$$

This shear stress is referred to as friction when it is evaluated at the wall -  $\tau_{wall}$ . However, there is also another aspect that influences the friction magnitude in a flow, namely turbulence. Despite not being an actual transport property, it has a similar effect to viscosity due to velocity fluctuations inclusion in the momentum equation. It may lower the value of  $P_0$  same as  $\mu$ . The stress exerted by the presence of turbulence is referred to as Reynolds stress and increases the  $\tau$  compared to Equation 1.7(19). The total shear stress due to viscosity and turbulence is:

$$\tau_t = \mu \frac{\partial \overline{u}}{\partial y} - \rho \overline{u'v'} \tag{1.8}$$



where u' and v' are velocity fluctuations. The effect of turbulence is quite complex and there is no general analytical expression that could be used to directly model its effect on friction. Thus, reliance on (at least some) empirical data is necessary when modelling turbulent friction coefficient or in general boundary layer.

In non dimensional form,  $\tau_{wall}$  is shown via friction coefficient Cf defined as

$$Cf = \frac{\tau_{wall}}{\frac{1}{2}\rho V^2} \tag{1.9}$$

The value for Cf can be found analytically for certain simple shapes (such as a flat plate), however for more complex surfaces (especially with turbulent flow) it is obtained empirically. A widely used model in air operating radial diffusers was proposed by Japikse(28):

$$C_f = k(1.8e5/Re)^{0.2}. (1.10)$$

With the definition of Equation 1.9 the stress exerted by the wall on the flow can be integrated to obtain for instance skin friction drag on an airfoil or in application to diffusers, it can be used in momentum equation to find balance between flow momentum and the wall resistance. The effect of the Cf will be directly experienced as a loss by lowering  $P_0$  and increasing entropy. Moreover, as the friction is a direct effect of interaction with the wall, the losses will be proportional to the area of the wall. Thus, in a diffuser, longer passage increases friction losses due to larger wall surface area. This is the first key consideration for a diffuser design, the length of the diffuser needs to be minimised in order to decrease the losses due to viscosity at the wall - friction.

Another way of looking at friction losses stems directly from experiments performed in straight pipes. It was observed that pressure decreases as the flow progresses, indicating loss. This effect is a direct consequence of viscosity and it can be attributed to friction. From measuring pressure difference  $\Delta P$  between two stations in a pipe, another characteristic property called friction factor f was derived:

$$f = \frac{\Delta P}{\frac{1}{2}\rho V^2} \cdot \frac{D}{L} \tag{1.11}$$

where L is the segment length and D the pipe diameter (18). This semi-empirical relation, referred to as Darcy - Weisbach formula, points to increasing losses with length of the passage. Additionally, it provides insight into the influence of the diameter. Moreover, there exists a relation between friction factor and friction coefficient, shown in the Equation 1.12.

$$f = 4Cf \tag{1.12}$$

From experiments with supercritical flows, relations for f were postulated to fit the results. As they treated turbulent flows, they are all functions of Re and include effect of wall roughness  $\frac{\epsilon}{d}(8)$ . In this work, three expressions were considered. The first one chosen in this study was put forward by Fang et al. in 2011 (10):

$$f = 1.613 \left( log(0.234 \left( \frac{\epsilon}{d} \right)^{1.1007} - \frac{60.525}{Re^{1.1105}} + \frac{56.291}{Re^{1.0712}} \right)^{-2}$$
 (1.13)

another, developed by Wang et al. (27) is defined as:

$$\frac{1}{\sqrt{f}} = -2.34 \times \log\left(\frac{1}{1.72}\frac{\epsilon}{d} - \frac{9.26}{Re} \times \log\left(\left(\frac{1}{29.36}\frac{\epsilon}{d}\right)^{0.95} + \left(\frac{18.35}{Re}\right)^{1.108}\right)\right) \tag{1.14}$$



and the last one, by Fang et al. in 2019 (9) suggested introducing a dimensionless factor Ch, shown in Equation 1.15, that would improve accuracy over a function just of Re and  $\frac{\epsilon}{d}$ .

$$Ch = \frac{p}{\frac{\dot{m}}{A}\sqrt{\Delta h_0}} \tag{1.15}$$

Here A stands for cross-sectional area through which the flow is passing and  $h_0$  is the difference in enthalpy of the supercritical fluid and its reference state of saturated liquid at T = 273, 15[K]. The final expression follows:

$$f = 0.0127 \left[ \ln(650(\frac{\epsilon}{D})^{0.67} + (\frac{99000}{Re})^{1.32} + 0.066Ch) \right]. \tag{1.16}$$

Using the definition from Equation 1.9 the momentum equation can be appended by friction and together with continuity, energy and equation of state solved analytically. Such a model was proposed by Stanitz(25) and is described in detail in the appendix.

#### Separation

In intended operation, pressure increases as the flow progresses through the diffuser. Thus, the flow encounters resistance from higher pressure zone. This is referred to as adverse pressure gradient and is especially important in boundary layer formation. It increases the boundary layer thickness, which reduces the available area where flow can expand and in critical case will lead to flow reversal. This is called separation, where flow can no longer follow the wall resulting in reduction of pressure recovery. The mathematical definition of separation is defined as:

$$\left(\frac{du}{dy}\right)_{y=0} = 0 

(1.17)$$

where y is the normal distance measured from the wall and u is the velocity component in x direction. Predicting the maximum adverse pressure gradient that the flow can withstand is the crucial design consideration. It is subject of many analytical and experimental investigations. The analytical models are mostly based on the Prandtl boundary layer theory or its derivatives. Already by applying the Prandtl equations (shown in appendix) it is possible to derive a meaningful, general conclusion for the boundary layer shape in adverse pressure gradient. The "first compatibility equation" in laminar flow, which is the application of momentum equation at the wall, shown in Equation 1.18 dictates that the shape of the boundary layer is initially concave for adverse pressure gradient.

$$\mu \left(\frac{\delta^2 u}{\delta y^2}\right)_{y=0} = \frac{dp}{dx} \tag{1.18}$$

The magnitude of the pressure gradient, will determine if the boundary separates. The influence of the gradient is best portrayed in the Figure 1.2.



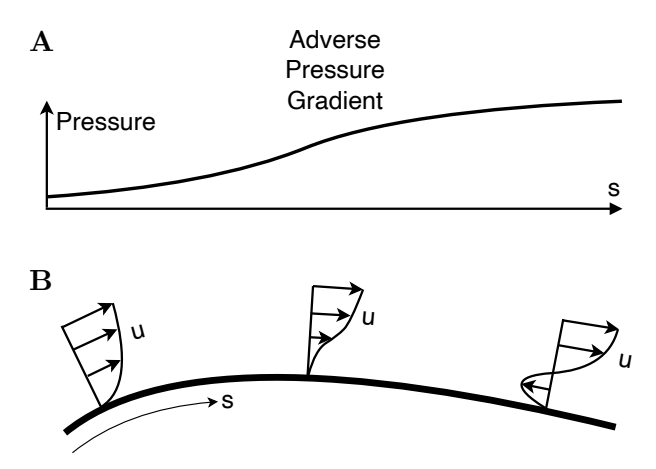


Figure 1.2: A Adverse pressure profile along surface. B Corresponding boundary layer velocity profiles.

The key takeaway from the separation losses is that the higher the pressure gradient, the higher the likelihood of separation that leads to uncontrolled growth of boundary layer and decrease in pressure recovered.

Thus, a design of diffuser needs to balance between friction losses that are proportional to the length of the passage and separation (and boundary layer growth) losses that are inversely proportional to length. The objective is to design such a diffuser that will convert the kinematic energy of the flow as fast as possible without leading to flow separation (7). From experimental data it was observed that as separation (referred to as stall in diffuser nomencalture) is approached, the pressure gain is diminishing and reaches its peak slightly after the separation occurs ( $2\theta$ ). This is shown in the Figure 1.3.

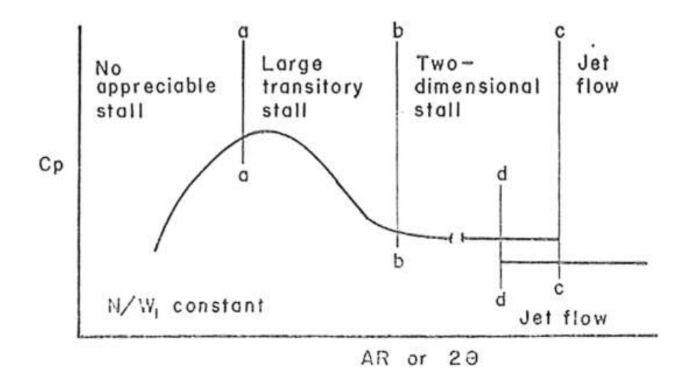
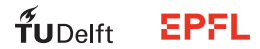


Figure 1.3: Pressure Coefficient as a function of AR leading to four distinct flow regimes. Adopted from Renau et al. with permission( $2\theta$ )

#### 1.1.3 Introduction to supercritical CO2

A fluid is referred to as supercritical when its temperature and pressure simultaneously exceed the critical point, defined for carbon dioxide at  $T_c = 304.21[K]$  and  $p_c = 73.773[bar]$ . What makes the fluid at such conditions remarkable is its dual nature of having very high liquid-like density and relatively low gas-like viscosity. This allows the fluid to expand more, like gas, which is very promising for turbomachinery applications (6).

In SC-CO2, the thermophysical properties fluctuate significantly, especially in the vicinity of the critical point. The thermophysical gradients are non-linear and the compressibility of the flow is much



higher than given by ideal gas law. Moreover, the enthalpy H and internal energy U are no longer functions of just temperature but also pressure (shown with Maxwell relations in appendix). Those characteristics render use of the conventional ideal gas EOS inappropriate.

The non-ideal behaviour of SC-CO2 can be visualised by compressibility factor Z that defines how actual density deviates from its ideal value (13). It is shown with specific volume v in the Equation 1.19.

$$Z = \frac{v}{v_{ideal}} \tag{1.19}$$

The value of Z will vary depending on the conditions of the flow, as critical point is approached, not only its value decreases but also the rate of that decrease is higher. The Figure 1.4 shows the compressibility factor variation throughout thermodynamic domain.

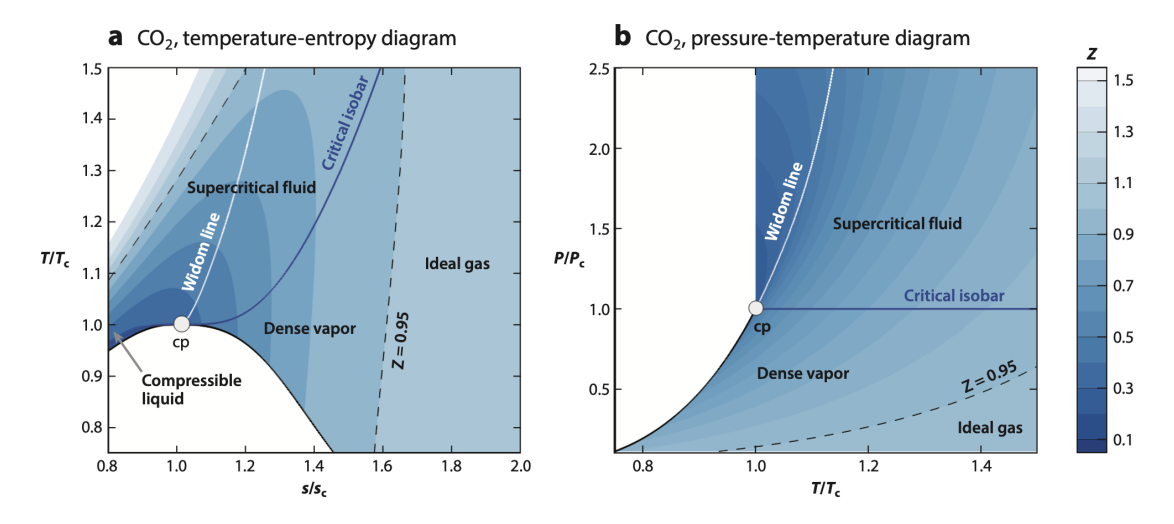


Figure 1.4: Magnitude of compressibility factor Z as a function of thermodynamic conditions. Adopted from Guardone et al. under CC BY 4.0.(13)

All those aspects make the conventional modelling methods highly unsuitable for calculating flow properties of SC-CO2. However, irrespectively of the gas properties, the fundamental conservation equations of fluid dynamics and thermodynamics still hold. Thus, for an inviscid flow (with no losses) the entropy remains constant which can be used to solve a non ideal gas problem via total properties conservation, analogous to isentropic relations (12). The detailed description of non ideal gas dynamics can be found in appendix.

#### 1.2 Nature of the issue

The core issue of designing a diffuser suitable for working with SC-CO2 is that the design guidelines were all developed for air or fluids that can be expressed with ideal gas law. Furthermore, the experimental database for SC-CO2 turbomachinery is scarce and no paper focusing on the design of SC-CO2 vaneless radial diffuser exists to the best author's knowledge. Thus, a comprehensive study is necessary that would address such flows.

The author distinguishes two main challenges when evaluating SC-CO2 flow characteristics, one related to the model of the gas and the other to ensuing non-ideal gas dynamics.

#### 1.2.1 Gas modelling

As shown in previous section, the SC-CO2 is characterised by highly non-linear thermophysical gradients and non-ideal compressibility which render ideal gas law highly inaccurate for both meanline

1D modelling and CFD applications.

One way to alleviate non-ideal compressibility is to use the compressibility factor Z in the ideal equation of state:

$$pv = ZRT (1.20)$$

With this assumption, the isentropic relations can be re-evaluated and used in the same fashion as the standard relations for ideal gas. However, they rely on the simplification that at a given point the compressibility Z does not change between static and total conditions, which depending on the flow regime and vicinity to the critical point may provide less accurate results. As shown in Figure 1.4 constant Z approximation is suitable only for limited range.

In order to capture full thermodynamic effects of supercritical flow, a model of Span-Wagner can be applied (24). This model is considered to be state of art in current research trends and is included in NIST database throughout a REFPROP software that allows for extracting all gas properties based on two variables (16).

A comparison for outlet properties of an isentropic SC-CO2 flow evaluated with different gas models is shown in the Figure 1.5.

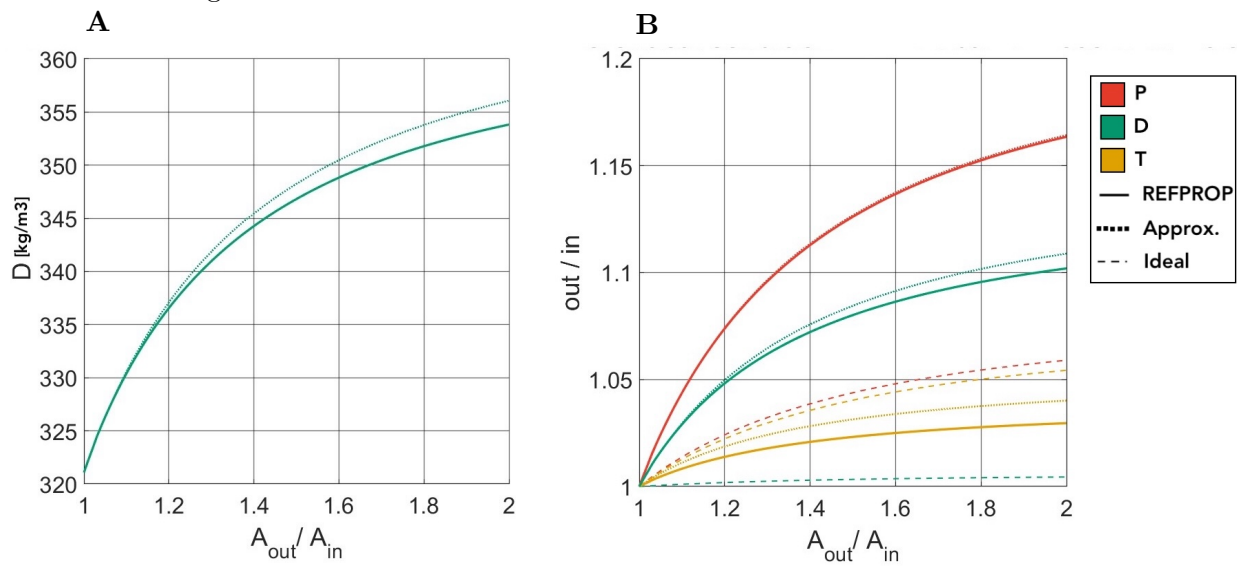


Figure 1.5: Outlet properties of isentropic SC-CO2 flow with inlet at T=305 [K], p=74 [bar] and M=0.5 evaluated with different gas models as a function of area ratio. **A** shows the magnitude of density variation and **B** shows the non-dimensionalised values against inlet conditions

In the Figure 1.5 the ideal result stands for use of ideal EOS, the Approx. is the model with Z and REFPROP uses the Span and Wagner model via a REFPROP library. The use of the constant Z approximation provides some relevant insight into the flow characterises as portrayed by the figure  $\mathbf{B}$ , where pressure variation is almost indistinguishable from REFPROP result. However, investigating temperature, reveals large deviations. Also, the density as shown in figure  $\mathbf{A}$ , reveals shortcomings of the approximation.

This is the first challenge related to SC-CO2 flows. Instead of using conventional 1D and CFD modelling methods where EOS can be applied directly as a single equation, properties from REFPROP library must be incorporated, significantly increasing computational effort.

#### 1.2.2 Diffuser performance modelling

Conventional one-dimensional (1D) meanline models, such as the Stanitz model (25), require an equation of state (EOS) in explicit form to allow for analytical solutions. However, the REFPROP library



does not support direct analytical use, which necessitates adaptations to the 1D model. Agromayor et al. proposed one such adaptation (1), but their approach introduces additional limitations. Specifically, the authors caution against using friction coefficient correlations in radial diffusers that were not developed for swirling flows. Another researchers even postulated building an artificial neural network in search of a data-drived approach that will produce a Cf most suitable for vaneless diffuser flow(23). While this limitation does not affect conical diffuser modelling, it significantly complicates the accurate simulation of radial diffusers with SC-CO2.

Another challenge arises from the uncertainty regarding which friction correlation, among those presented in Equation 1.13–1.16, is most suitable for application in the 1D model. Each of those expressions was derived from experimental data based on different supercritical fluids and operating conditions, and as such, variations in their predictions are expected when applied specifically to SC-CO2 flow scenarios.

The prediction of flow separation and its associated losses further compounds the modelling complexity. Accurately capturing boundary layer reversal is difficult, and as such, diffuser design still relies heavily on empirical guidelines. These guidelines are based on extensive experimental research involving air-breathing diffusers and may not be directly applicable to SC-CO2 due to its distinct thermophysical properties.

Lastly, resorting to CFD modelling to provide more insight into flow behaviour, will also pose serious challenges. Changing the gas model to the SW, can be done by inclusion of "Real Gas Properties" (RGP) tables(5). However, use of those significantly increases the computational time as each thermphysical property needs to be interpolated from the tables at each iteration.

To alleviate the cumbersome process of calling RGP tables in CFD simulations, a barotropic gas model can be deployed. It assumes that the thermophysical properties are only a function of pressure (14). Through expression statements, a predefined relation between density and pressure  $\rho$  - p as well as viscosity and pressure  $\mu$  - p can be imposed in the solver. As such, the energy equation is switched off, and the model solves only the continuity, Navier-Stokes, and turbulence equations. Thus, this is a simplification and as a result the effect of viscous work is neglected and the flow losses (through entropy increase) are imposed due to  $\rho - p$  coupling.

Furthermore, accurate modelling of SC-CO2 with CFD requires a mesh of higher resolution. Due to higher thermophysical gradients, the changes are expected to be more pronounced. Also, higher turbulence resulting from high  $\rho$  and low  $\mu$  suggests that the element height for  $y^+=1$  needs to be much lower than for air. This results in a mesh having overall more elements for SC-CO2 than for air for the same geometry, directly increasing the computational effort

M. Dabrowski 9 of 56 June 2025



#### 1.3 Objectives and Scope

The objective of the present research was to investigate the flow behaviour and frictional characteristics of supercritical SC-CO2 in vaneless radial and conical diffusers, using both one-dimensional meanline modelling and CFD. The scope of the work is outlined as follows:

#### Meanline Modelling:

- Implementation of a thermodynamic model for SC-CO2.
- $\bullet$  Inclusion of frictional effects specific to SC-CO2 flow by use of Cf expression in conical and radial diffusers.
- Integration of a separation prediction method based on the Stratford criterion.

#### **CFD Simulations:**

- Incorporation of a non-ideal gas model for SC-CO2 via a barotropic model.
- CFD analysis of vaneless radial and conical diffusers operating with air and SC-CO2 at matching Mach number
- Extraction of friction coefficients in axial and radial flow.

#### **Research Contributions:**

- Identification of the most appropriate friction factor model for various simulation conditions.
- Determination of the maximum achievable diffuser expansion ratio before flow separation occurs.
- Proposal of design guidelines for SC-CO2 diffusers based on the combined insights from meanline and CFD analyses.



#### 2 METHODOLOGY

This section provides insight into methods used to achieve the objectives of the research. It firstly covers the design space and the parameters that were chosen. Secondly, it explains how 1D meanline modelling was achieved. Lastly, it delves into the properties of the CFD simulations that were necessary to successfull evaluate SC-CO2 flow in a diffuser.

#### 2.1 Diffuser terminology and assessment

The scope of this research was narrowed down to only consider diffusers with straight profiles. With this assumptions, the geometry of a diffuser can be fully defined by the parameters shown in Figure 2.1.

Based on the nomenclature above, two ratios used for benchmarking diffusers are introduced: area ratio (AR) and length over width (NW). Those two fully determine straight wall diffuser geometry. Whereas the effect of AR is mostly responsible for the pressure recovery, the varying NW will be changed to balance friction and separation losses. As length is crucial in determination of the friction losses and pressure gradient responsible for separation. In the conical diffuser those parameters are obtained as follows:

$$AR = \frac{R_{out}^2}{R_{in}^2} \tag{2.1}$$

$$NW = \frac{L}{2R_{in}} \tag{2.2}$$

and in radial diffuser:

$$AR = \frac{R_{out}B_{out}}{R_{in}B_{in}} \tag{2.3}$$

$$NW = \frac{R_{out} - R_{in}}{B_{in}} \tag{2.4}$$

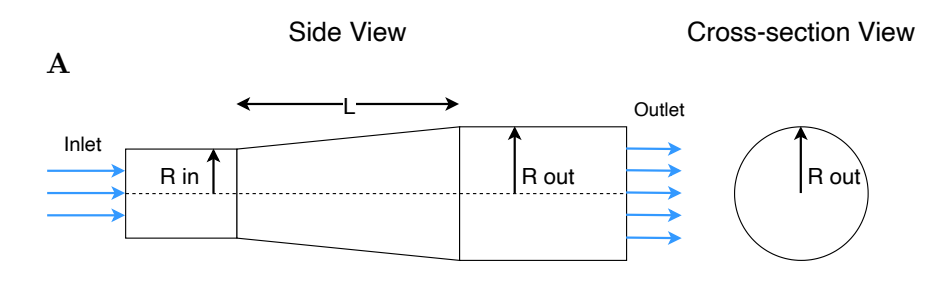
#### 2.2 1D Meanline Model

#### 2.2.1FRICTIONAL EFFECTS

The first step in designing a diffuser (and in general turbomachinery) is often simplified calculations assuming one dimensional flow, hence the name 1D Meanline Model. As mentioned before, the model developed by Stanitz and updated by Agromayor et al. is not suitable for use with Cf expressions found in literature for SC-CO2 flow. Instead a model based on evaluation of total properties is applied that follows the idea presented in appendix in iterative routine shown by Grossman (12). This model, designed with operation of radial diffuser in mind (with few alterations can be used for conical as well) is property of LAMD and is a part of a larger meanline model of a compressor (21). It is a matlab script that iteratively finds gas properties that satisfy the flow constraints.

The working principle of the 1D model is shown in the flow chart in Figure 2.2. To apply this method, the diffuser should be split into many sections and the routine from the chart should be applied iteratively.

The solver starts with inlet properties that comprise: static thermophysical values, flow velocity and  $\alpha_{in}$ . Based on them, the inlet total values are evaluated. Next, the outlet total value are derived as follows. The flow is assumed to be completely adiabatic with no work exchanged, thus, the value of total enthalpy  $H_0$  is taken to be constant. Then, to evaluate the value of outlet  $P_0$  the pressure drop  $dP_0$  is calculated from frictional losses that are calculated via the Equation 1.11 and one of the



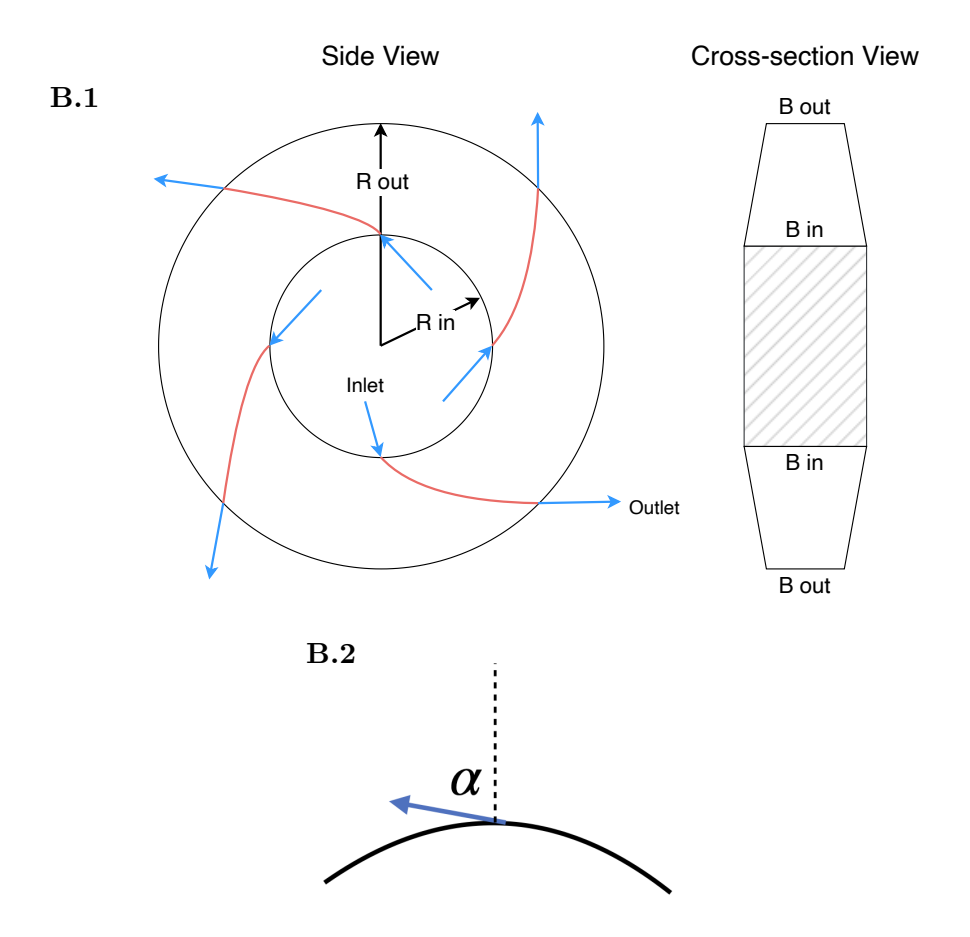


Figure 2.1: Sketches of diffuser geometries with parametrisation, shown with side and cross-section views. (A) Conical diffuser with radii and length denoted as **R** in, **R** out and **L** shown with blue arrows indicating direction of streamlines entering and leaving. (B.1) Radial diffuser with radii and widths denoted as **R** in, **R** out, **B** in and **B** out shown with blue arrows indicating direction of streamlines entering and leaving, and red lines indicating streamlines within the diffuser. (B.2) Definition of inlet flow angle in radial diffuser.

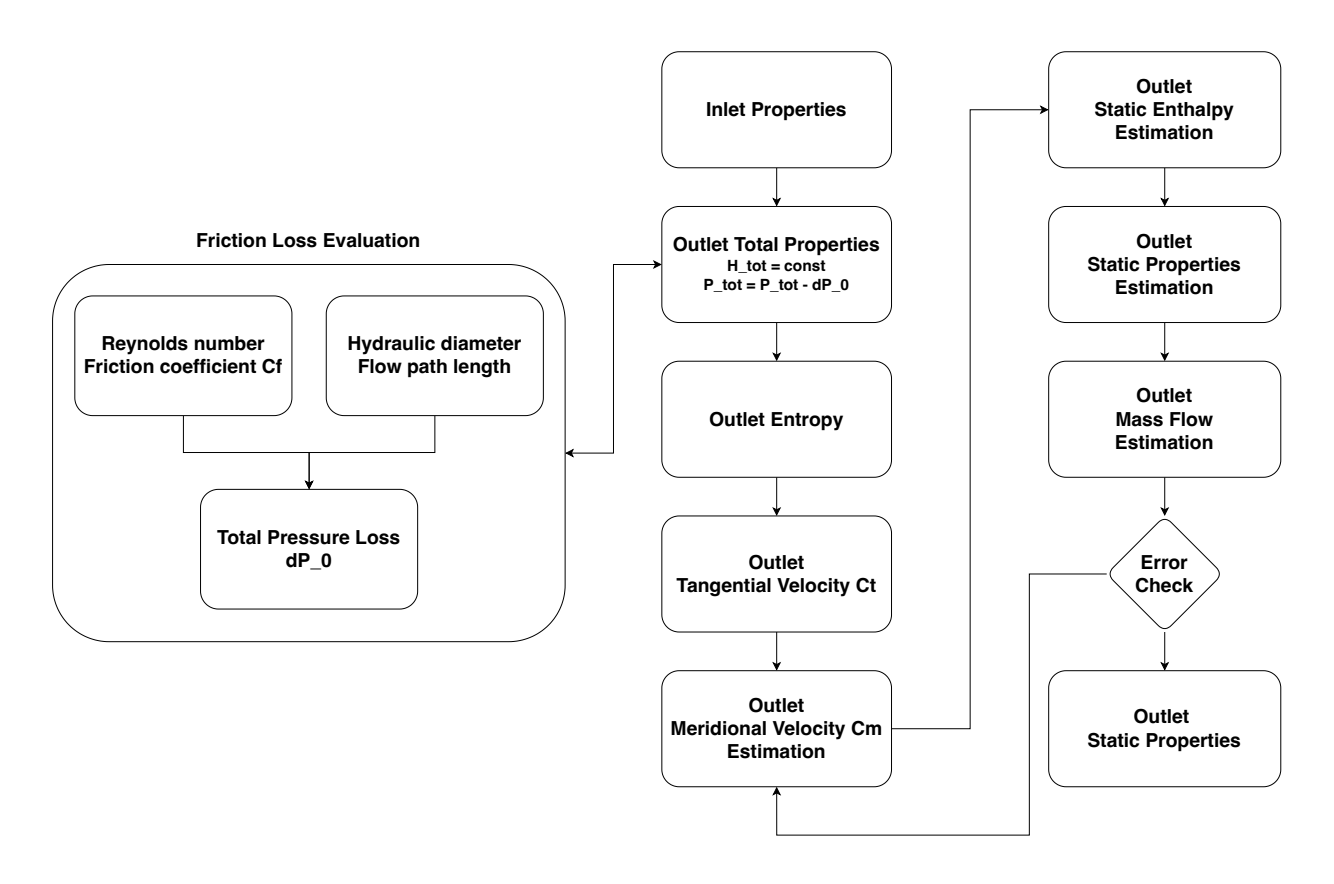


Figure 2.2: Flowchart of the 1D meanline model routine for evaluating flow properties

experimental expressions for Cf. The diameter D is taken as the hydraulic diameter and the length L as the flow path length. Based on the tangential momentum conservation from Stanitz model, the tangential velocity  $C_{\theta}$  is computed (in conical diffuser this step is omitted). Subsequently, the meridional velocity Cr (or for conical diffuser absolute velocity V) is estimated through incompressible flow relation. Based on the estimate, absolute velocity is calculated and from that static enthalpy at outlet is computed. Having, the estimate for static enthalpy and known entropy at outlet, from REFPROP database other static thermophysical properties can be derived, notably density. With new density, mass flow is evaluated. If the mass flow difference between inlet and outlet is deemed to be acceptable, the solution is found. If the error for mass flow is too high, another estimate for Cr can be taken and the calculations are done again. To increase convergence speed, this is done with a Newton's method.

#### 2.2.2 Separation prediction

Separation, a consequence of flow reversal, takes effect due to adverse pressure gradient. In diffuser design it is important to determine the critical value of adverse pressure gradient that the boundary layer can withstand without reversal. An important aspect that will influence that is the turbulence of the flow. Due to higher mixing and more energetic flow, the turbulent boundary layer can withstand higher pressure gradients, shown with turbulent "first compatibility equation":

$$\mu \left( \frac{\delta^2 \overline{u}}{\delta y^2} \right)_{y=0} = \frac{d\overline{p}}{dx} + \frac{\delta}{\delta y} (\rho \overline{u'v'})$$
 (2.5)

Analogously to laminar flow expression in Equation 1.18, this expression was derived from boundary layer equations model, here assuming turbulent flow (22). What Equation 2.5 shows, it that the



concave shape of the boundary layer (determined by second derivative of u) in turbulent flow is not only subject of pressure gradient but also fluctuating velocity terms (i.e. turbulence). The effect of positive first term (adverse pressure gradient) is countered by the second in turbulent flow, which conveniently, is negative in boundary layer. This is a clear evidence that separation prediction in diffuser flow needs to include turbulence.

The intent was to include separation prediction in a 1D meanline model, without changing much the nature of the code. As such, instead of lengthy process of iteratively finding boundary layer equations solution that satisfies the core flow, a simplified model assuming independent core flow of boundary layer was used. One of the most famous general models for prediction of boundary layer reversal is due to Stratford (26). This method makes the following assumptions:

- 1. Incompressible boundary layer,
- 2. Similarity of boundary layer shape to a flat plate case,
- 3. Divides boundary layer into two sublayers,
- 4. Due to adverse pressure gradient: outer sublayer does not change its shape but only magnitude, inner sublayer changes shape.

Stratford provides analytical expressions for both sublayers and verifies if they can coexist within the boundary layer thickness. The critical value of Cp for which they can be merged is then derived to take the form of Equation 2.6. The full derivation is explained in the appendix.

$$(2Cp)^{\frac{n-2}{4}} \left( x \frac{dCp}{dx} \right)^{\frac{1}{2}} = 1.06\beta (10^{-6}Re)^{\frac{1}{10}} \quad \text{for } \left( Cp \le \frac{n-2}{n+1} \right)$$
 (2.6)

The factor  $\beta$  is an empirical property derived from pertinent experiments and n is the factor used in power law describing outer shape of boundary layer. The condition above, can be programmed into the 1D meanline code to check at each iteration if the Cp increase is not too high, leading to separation. The condition also takes into account boundary layer development and predicts that for increasing boundary layer length, the  $\left(\frac{Cp}{dx}\right)_{max}$  is decreased. The separation criterion attractiveness stems from its simplicity and ease of inclusion in 1D meanline code, without performing entire boundary layer calculations.

However, as the Stratford criterion is a simplification, it will suffer from the following limitations:

- 1. Cannot predict separation accurately for significantly curved surfaces,
- 2. Relies on experimental factor  $\beta$  that was determined for ideal gas like fluids,
- 3. Does not account for boundary layer growth and consequent decrease in Cp (due to lower expansion area for the flow) just before the separation,
- 4. Cannot evaluate pressure recovered after separation occurred.

#### 2.3 CFD MODEL

To validate the findings from 1D meanline model, CFD simulations were performed. To conduct simulations, commercial software ANSYS CFX was used(3). Using the definition of geometry from Figure 2.1 CADs of the diffusers were created and meshed. In order to limit the effect of numerical diffusion, structured meshes were designed. For the conical diffuser an O-grid mesh with inflation layer at the walls. The mesh element size at the wall was evaluated to aim at a given  $y^+$  value by applying one of the Cf expressions(19). In radial diffuser mesh, to save computational resources the domain was decreases to a 45° slice. To make it work, the boundary conditions were selected as periodic, meaning that the result on one will be directly copied to the other. The mesh for conical diffuser is shown in Figure 2.4 and for radial diffuser in Figure 2.5. The turbulence model selected for the study was k-omega SST due to its good performance on prediction of separation(5).



To model the thermophysical properties of the gas, a barotropic approach was employed in place of RGP tables. This method was selected as it is more robust. Close to critical point the thermphysical gradients make the isotherms and isobars in T - s diagram parallel, meaning that a minute change in a property will result in very high change in entropy. This limits the accuracy of prediction as the solver struggles to find an appropriate solution. As a result, the simulations with barotropic model that does not call entropy, demonstrated greater numerical stability than those using RGP tables for SC-CO2. Moreover, the barotropic model inherently simplifies property variations outside the expected solution domain, which further contributes to improved convergence behaviour.

The incorporation of barotropic model in CFX was done via "expressions" functionality. In material creation, instead of providing a constant value for density and viscosity, an expression linking it to pressure can be inserted. The other information necessary is the molar mass and specific heat. The material model does not contain as such information on entropy or temperature. Thus the simulations do not solve the energy equation.

The disadvantage of using the barotropic model is that it provides less accurate solution. Through imposed relation between pressure and density, efficiency of the process is imposed. Moreover, the effects related to viscosity in energy equations, such as viscous work or heating, are not included (5). Lastly, as the model does not have access to entropy information, the total pressure values are evaluated as if they were incompressible through Equation 1.2 which makes the total pressure results less reliable (4).

The selection of the exact barotropic model relies on selection of process efficiency. As the Iso-Thermal and Iso-Enthalpic process were actually predicting decrease in entropy for increasing pressure in SC-CO2, they were discarded as potential candidates for use in CFD. Instead, process with imposed polytropic efficiency were explored. However, as it is generally not known a priori which efficiency is most suitable for a diffuser flow, another process was derived from 1D meanline model solution. By knowing pressure and density evolution along the diffuser, it is possible to extract a T-s process by use of REFPROP library. The chosen process for barotropic model are shown for conical (**A**) and radial (**B**) diffusers in Figure 2.3.

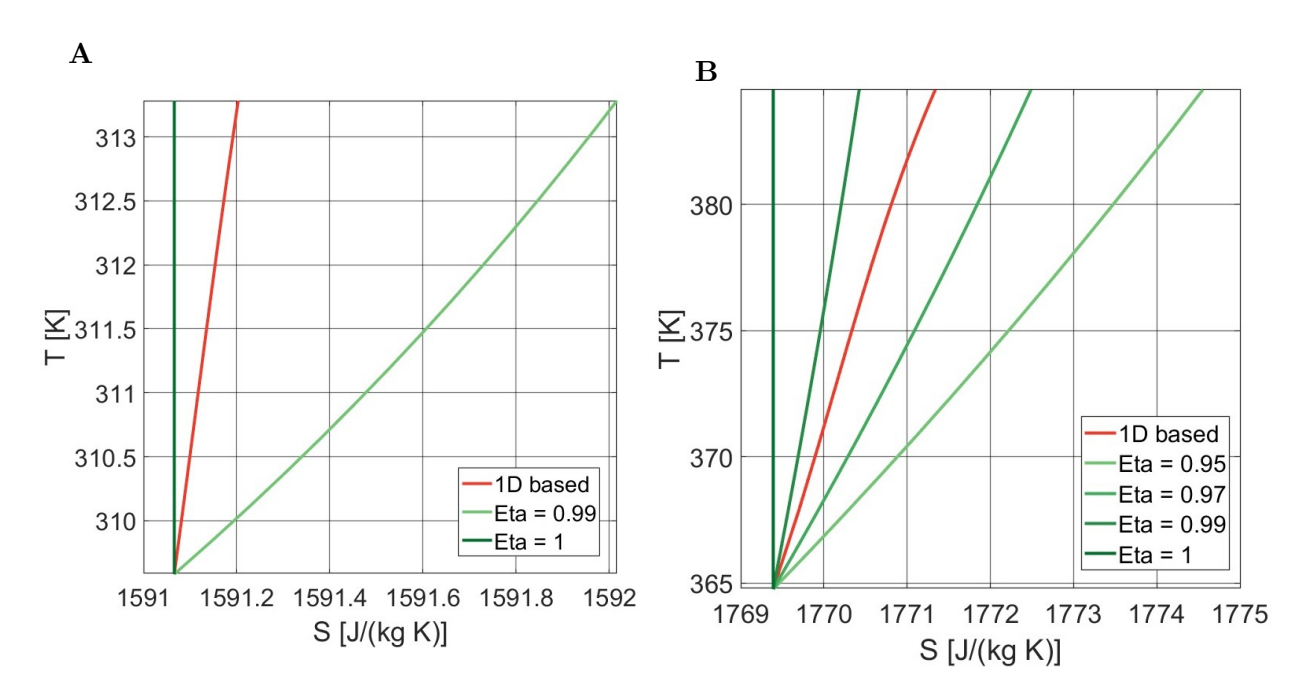


Figure 2.3: Barotropic models polytropic efficiency (A) Conical and (B) Radial diffuser.

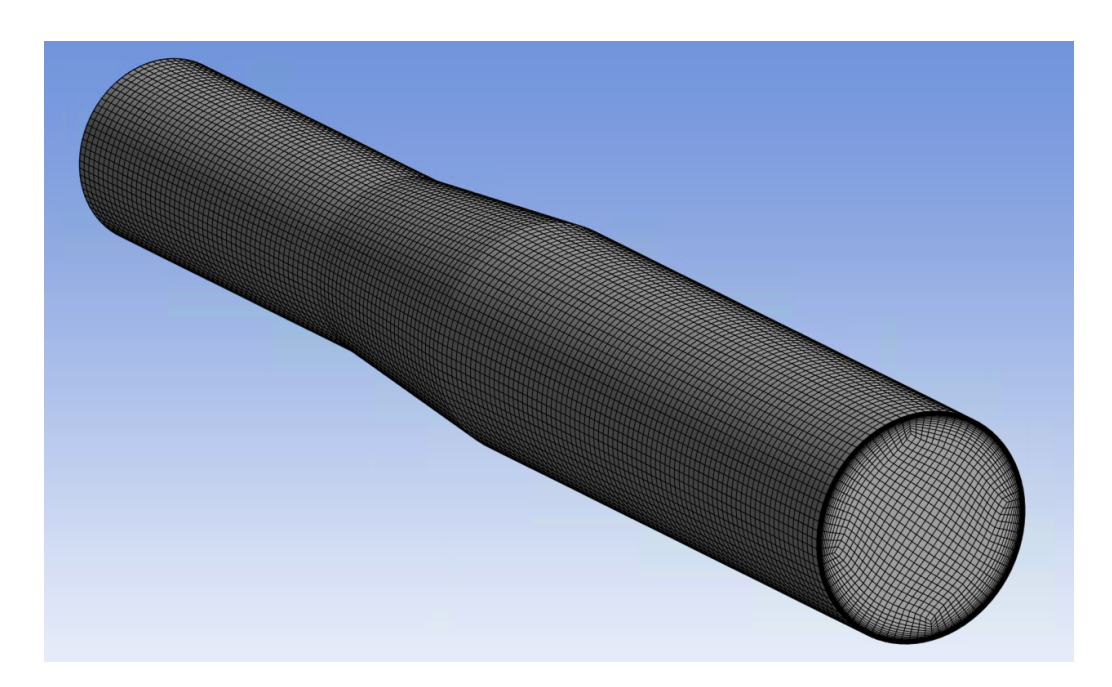


Figure 2.4: An example of a mesh used for CFD simulation of a conical diffuser

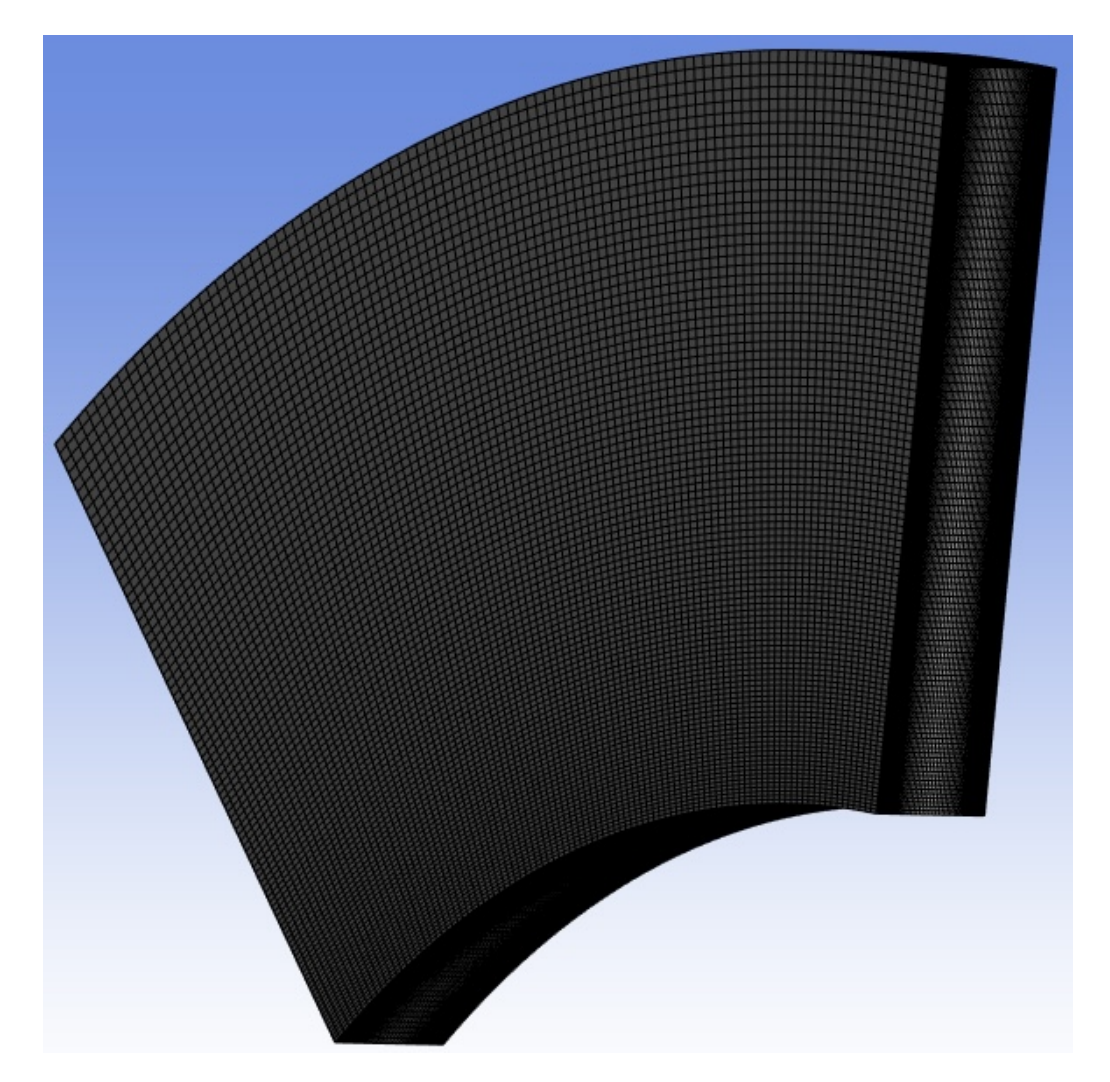


Figure 2.5: An example of a mesh used for CFD simulation of a radial diffuser



## 3 Results and Discussions

In this section, the results of two approaches: 1D model and CFD, are presented for conical and radial diffusers operating with SC-CO2. Throughout the study, more than one hundred different geometries were tested in spirit of assessing a parametric performance aiming to provide design guidelines.

To provide insight into flow phenomena and limitations of 1D approach, three geometries were chosen (for radial and conical each). The first is when the flow undergoes benign change due to low AR, second is when the flow achieves its maximum Cp value as predicted by CFD and the last when flow is separated. All tested geometries were assumed to have the same inlet geometries and thermodynamic conditions.

Having looked in detail into flow phenomena differences in 1D and CFD, results of parametric study are revealed. Using the Cp metric, the CFD SC-CO2 results are systematically compared with their corresponding air-based cases to highlight the influence of non ideal gas effects on flow behaviour.

Furthermore, the CFD analysis includes an evaluation of the Cf in SC-CO2 for fully developed flow in a straight pipe and a radial diffuser and compares it against the Cf models from literature.

#### 3.1 1D Model

#### 3.1.1 Conical diffuser

The three geometries that were chosen in conical diffuser are: AR equals 1.6, 2.4 and 3 with fixed length of the diffuser - 0.06[m] making NW equal 3. Furthermore diffuser was taken to have inlet of 0.05[m] length and outlet 0.08[m]. Inlet and outlet have constant area. Plots of properties found in conical diffuser with 1D meanline model as a function of the diffuser length were derived with Cf model of Fang et al. presented in the Equation 1.13. Whereas the absolute values of the results vary depending on Cf model, the overall trends are maintained. This section aims to discover limitations of the 1D nature of the model, details on selection of an appropriate Cf will be considered later.

Figure 3.1 shows results for those three geometries as a function of the axial location. In order to best assess the performance of the 1D model, each plot will be discussed separately. Starting with observations of the Figure 3.1 plot  $\mathbf{A}$ , showing evolution of static pressure, the following can be said. Pressure initially decreases in the inlet region, followed by rapid increase in pressure in the expansion region. Lastly, pressure decreases in the outlet region, however less steeply than at inlet. The same trends are shown regardless of AR.

The reason for predicting pressure decrease in a constant area channel (straight pipe) is due to effect of friction incurred by the surrounding walls. This is a direct implication of including the Cf in the simulation. Next, the crucial section of the diffuser begins, where pressure recovery occurs. The flow slows down to be able to fill up the passage. This decrease of kinetic energy is manifested by increase in static pressure as the simplified momentum equation in 1.1 shows. Lastly, the outlet is again a straight pipe, so frictional effects decrease the pressure. The reason for the lower gradient than in the inlet can be seen in Equation 1.11, which shows that the pressure drop is proportional to the square of velocity and inversely proportional to the diameter of the pipe. At the outlet, the diameter is the largest, and the velocity the lowest. Hence the lower pressure loss. The same explanation can be give to why the gradient of outlet pressure for AR = 3 is the lowest.

In the Figure 3.1 plot  ${\bf B}$  evolution of axial velocity along the diffuser is plotted. In constant area sections, inlet and outlet, the velocity remains constant. In the expanding part, the flow decelerates. With changing the AR, flow reaches different velocities as can be expected.

Lack of change of the velocity in the inlet and outlet is a numerical limitation. In general, the solver is able to predict increase in velocity in constant area pipes, however, in SC-CO2 application, the accuracy of the error check, neglects that effect. In reality, due to pressure decrease, the density

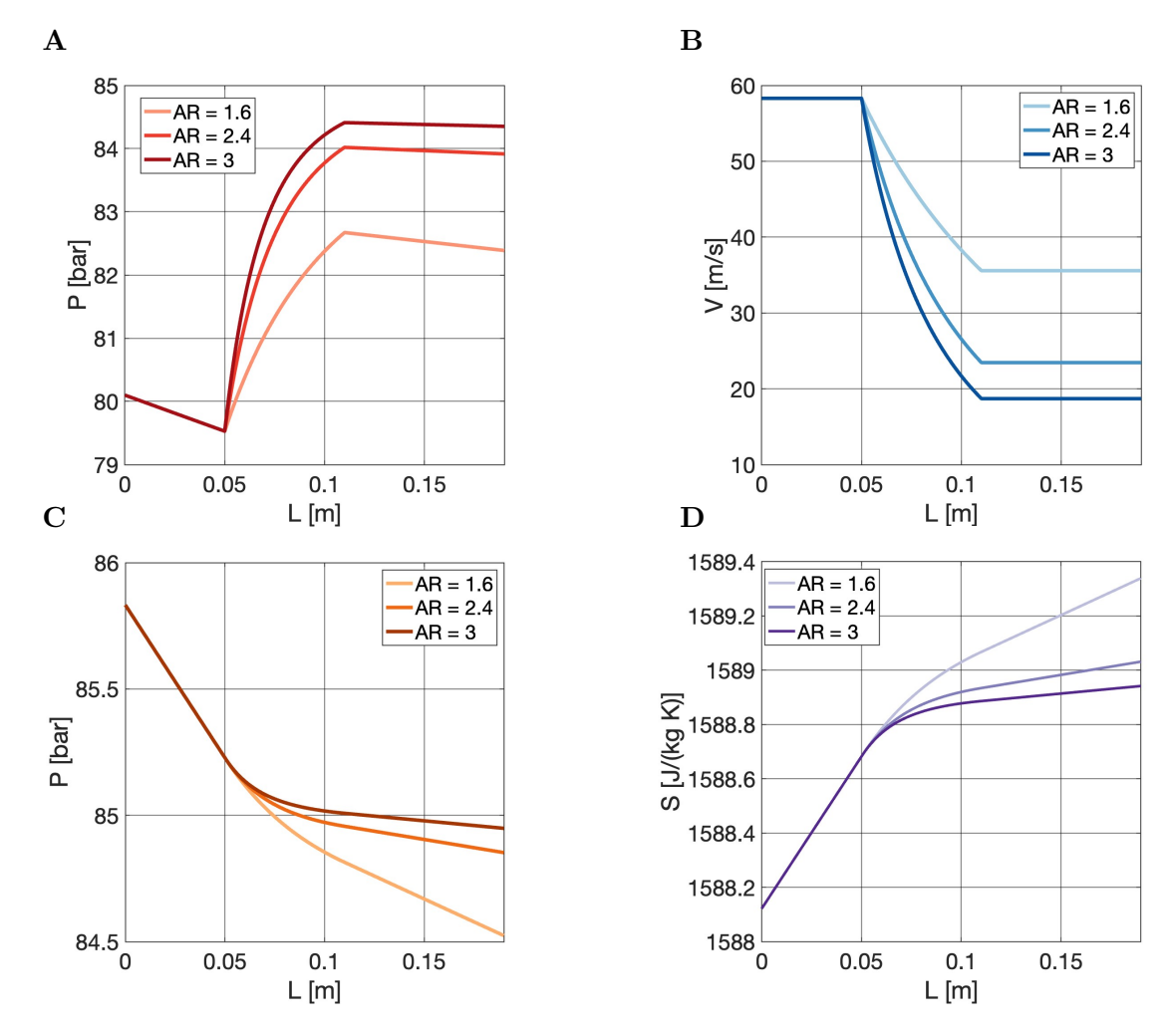


Figure 3.1: Results from the 1D meanline model of SC-CO2 for a conical diffusers with length NW=3, using the friction correlation from Fang (2012). Inlet conditions are: velocity  $V_{\rm in}=58.3$  [m/s], pressure  $P_{\rm in}=80.1$  [bar], and temperature  $T_{\rm in}=310$  [K]. The plots illustrate: (A) Static pressure, (B) Velocity, (C) Total pressure, and (D) Entropy distributions along the diffuser.

is also lowered, and that leads to increase in velocity due to continuity equation. Regarding, the deceleration in the expanding section, the fundamental assumption of 1D model is that the flow is indeed one dimensional and fills up the entire passage. Consequently, by expanding the cross sectional area, the flow is forced to slow down to be able to fill up the entire passage. As density does not decrease (actually increases), the velocity has to decrease to satisfy the continuity. Thus, increasing cross section area decreases the velocity of the flow. This is also the reason for lower final velocity reached for higher AR designs.

The total pressure plot in the Figure 3.1 plot C shows  $P_0$  decreasing throughout the domain. Initially, the decrease is the steepest, gradually flattening. At the point where inlet ends, the curves diverge and follow different gradients. The evolution of  $P_0$  is a direct consequence of the geometry. As shown in 1D model flow chart in Figure 2.2, this is the very first property that is evaluated. It is weakly dependent on Re and primarily a subject to geometry - diameter, through Equation 1.11. Thus, for larger cross section area the loss will be lower.

To benchmark the efficiency of the process, the entropy plot in Figure 3.1  $\mathbf{D}$  can be addressed. Its result is tightly linked to that for total pressure. For the lowest AR, the highest loss is predicted as the diameter is the lowest. The entropy values were called from REFPROP, based on total enthalpy and total pressure, as the second property evaluated through 1D model. Thus, they again depend almost

3.1 1D Model

exclusively on geometry, through total pressure. Looking at the absolute values, all three results are of comparable magnitudes. However, for a CFD simulation using the barotropic model to be more accurate, the model parameters should ideally be derived from a 1D meanline analysis conducted on the same geometry.

Regarding the evolution of other properties such as density or temperature, they are extracted from REFPROP too. They follow the same trends that pressure plot does, however their magnitudes vary. The density evolution was used in construction of barotropic model but other than that, they do not provide more insight into this section, and hence were omitted here.

As is visible, in the plots above, 1D model as taken from Figure 2.2 does not predict pressure drop due to flow separation at AR = 3. Without lengthy boundary layer calculations and iterative solving of the flow domain, predicting flow recovery after separation is not possible. What can be done however, is to use the Stratford condition to provide a limit to which solution is possible to be achieved.

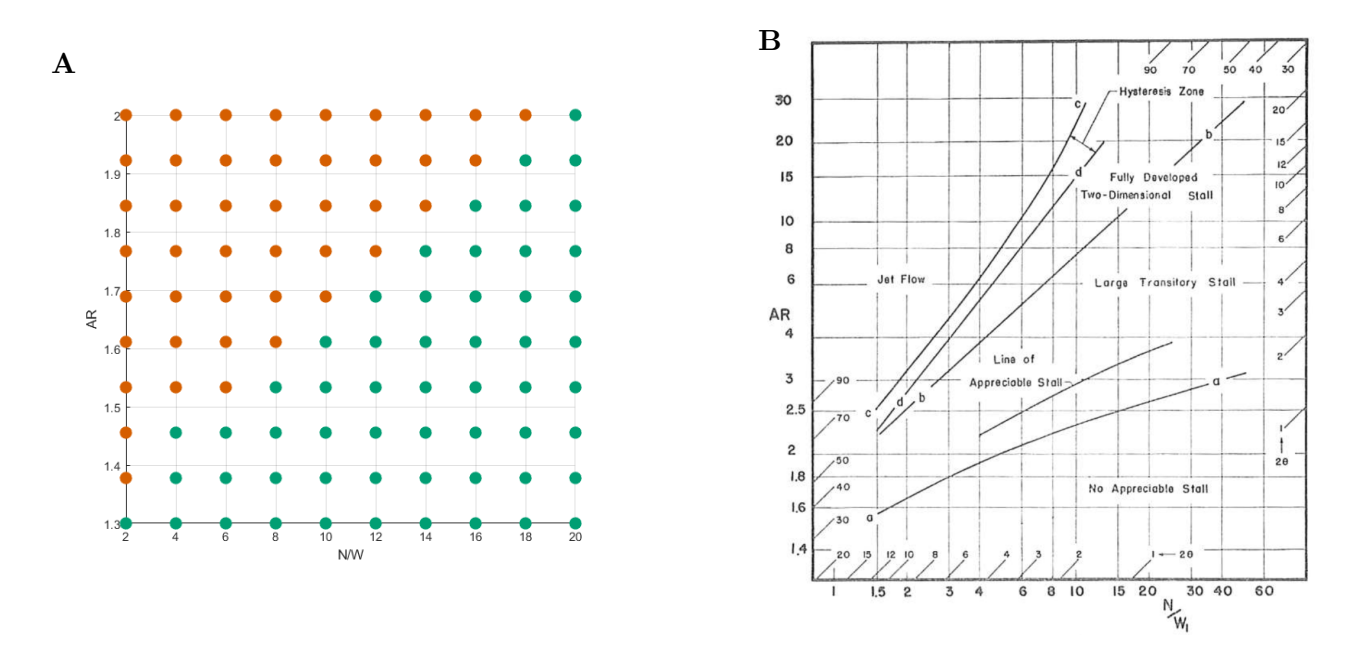


Figure 3.2: Separation in a conical diffuser: (**A**) Prediction of 1D code - red dot indicates stall and green lack of stall. (**B**) Experimental data of Renau et al. 1967, adopted with permission ( $2\theta$ )

In the Figure 3.2 A, a binary plot shows whether the given combination of AR and NW results in separation (red dot) or not (green dot). This figure was obtained for specific inlet conditions and geometry. It portrays similar trend to the experimental results in B, where a-a line indicated the appearance of stall. The separation limit line predicted by the model exhibits an approximately linear trend. This behaviour aligns well with theoretical expectations, indicating useful prediction framework. Flow separation is primarily governed by the adverse pressure gradient, and the accuracy of its prediction is sensitive to two key factors: the inlet boundary layer thickness (specifically, the momentum thickness) and the empirical Stratford parameter,  $\beta$ . The Stratford criterion assumes a boundary layer development analogous to that over a flat plate; however, in highly curved geometries, such as in high AR diffusers, the boundary layer may grow more rapidly, potentially affecting separation onset. In the case of conical diffusers, both the channel length and the outlet area influence the pressure gradient, which is the dominant driver of separation as described by Stratford's theory.

However, upon further testing, the Stratford criterion proved to be not fully adequate. The main issue is that its applicability is limited by the theoretical boundary layer thickness over a flat plate. To satisfy that, the maximum Cp condition was given. For diffusers with higher AR it often breached

TuDelft EPFL

that value. Thus, the Stratford condition can only be used under specific flow regimes.

#### 3.1.2 Radial diffuser

For the radial diffuser, three geometries that were selected are: AR equals 1, 1.65, and 2 with NW = 5.42. To obtain these results, the friction factor model proposed by Wang et al. (from Equation 1.14) was applied. Similarly to the conical diffuser case, the choice of friction model affects the absolute values of the results, but not the overall trends. The outcomes of the 1D model are presented in Figure 3.3 as functions of radial location.

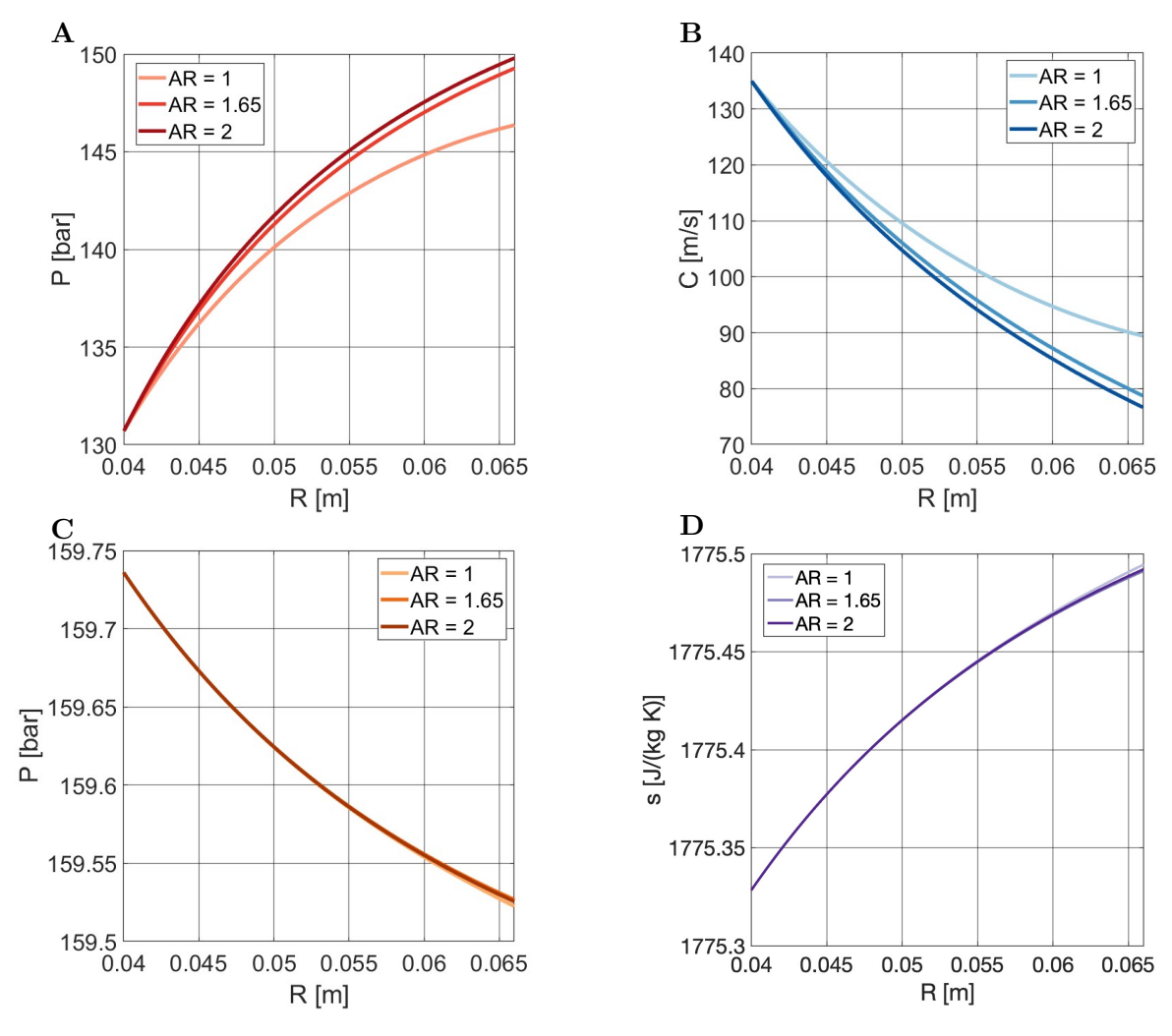


Figure 3.3: Results from the 1D meanline model of SC-CO2 for radial diffusers with length NW = 5.42, using the friction correlation from Wang (2014). Inlet conditions are: velocity  $C_{\rm in} = 135 \, [{\rm m/s}]$ , pressure  $P_{\rm in} = 130.71 \, [{\rm bar}]$ , and temperature  $T_{\rm in} = 364 \, [{\rm K}]$ . The plots illustrate: (**A**) Static pressure, (**B**) Velocity, (**C**) Total pressure, and (**D**) Entropy distributions along the diffuser.

The results for the radial diffuser configurations reveal several notable trends across different area ratios. Starting with the plot **A** in Figure 3.3, the static pressure increases along the radial direction, with the steepest gradient occurring at the beginning. Beyond an AR of 1.65, the gain in pressure recovery is marginal. Another important finding is that pressure recovery occurs also for case where geometric area at the outlet is the same as at inlet - AR = 1.

This behaviour is consistent with the theoretical relationship shown in Equation 1.6, where pressure recovery scales non-linearly with both AR (which could be viewed as a function of radius AR(R) shown

1D Model 3.1

in appendix) and diffuser length NW (expressed through the radius ratio, RR). As the geometry was taken to have straight walls, the area does not scale linearly with radius. Instead, it increases the most at the beginning, hence the steepest profile there.

The ultimate pressure recovery for those three geometries differs only due to AR as they have the same length (again shown by Equation 1.6). Thus by looking at the term  $\left(1 - \frac{1}{AR^2}\right)$  it is clearly visible that final pressure recovered is not linearly dependent on AR, hence marginal benefit of AR = 2 over AR = 1.65.

Lastly, the reason for having pressure increase in a diffuser with AR = 1 is due to effect of  $\alpha$  and RR as shown in the Equation 1.6. As the flow travels throughout the diffuser, 1D model (as well as an ideal one) suggest that, its angle  $\alpha$  changes making flow leave more radially than when it entered. As mass flow needs to be conserved in the system, the absolute velocity C must decrease. It can be seen by inspecting the continuity equation for radial diffuser stated in Equation 3.1.

$$\dot{m} = \rho \cos{(\alpha)} CA \tag{3.1}$$

If the angle  $\alpha$  decreases then  $\cos(\alpha)$  increases and finally the absolute velocity C must decrease and as such provide pressure recovery despite area being constant. This explanation holds for a compressible case and for a case with friction, albeit they require other expressions to fully evaluate the flow.

Similar findings and conclusions are found for the velocity evolution in plot **B** in Figure 3.3. The velocity decreases gradually throughout the radius of the the diffuser, being the steepest at the beginning. This again is attributed to the area changing the most at the beginning. Moreover, the same trends for different final AR is present as in pressure plots. Changing AR beyond 1.65 has minimal effect. The pressure and velocity plots complement each other according to the momentum equation. Again, the exchange between kinetic energy and pressure, like in Equation 1.1 is portrayed.

Moving to the plot C Figure 3.3, the total pressure decrease is the property that can be seen as the sign showing how much the pressure recovery deviates from its ideal form of Equation 1.1. Similarly to the results in conical diffuser, the value of  $P_0$  is the first property that 1D code evaluates. However, an expression for hydraulic diameter is very different to a conical case. In radial it is defined as follows from the Equation 3.2.

$$Dh = 2\sqrt{2R_{in}B_{out}} (3.2)$$

As the variation in diffuser width B does not change significantly throughout the diffuser and between the designs with different AR, the effect of different Dh is marginal, leading to similar values in all three geometries.

Lastly, entropy from Figure 3.3 D is discussed. Entropy increases in a manner inversely proportional to the decrease in total pressure, and again, the impact of AR on this trend is minimal. Entropy was directly calculated from total pressure and total enthalpy using REFPROP. As total enthalpy was assumed constant, the entropy distribution effectively mirrors the total pressure profile, like in the conical case. The diffuser losses predicted by the 1D model show limited sensitivity to changes in geometry. As a result, efficiency estimates are nearly independent of final AR, supporting the use of the simplified barotropic gas model derived from one geometry in all radial simulations.

As with the conical diffuser, the 1D model does not account for the effects of boundary layer reversal on pressure recovery. The highest AR provides highest pressure recovery, which is not the case in reality. To address this limitation, the Stratford criterion was applied in the radial direction to estimate the upper limit of pressure recovery before flow separation occurs. Only the radial component of the flow path was considered in evaluating the pressure gradient, focusing on the pressure rise along the radius. This approach is hypothesized to implicitly incorporate the influence of the inlet flow angle  $\alpha_{in}$ .

The analysis, shown in Figure 3.4 indicates that increasing the length NW leads to a reduction in the maximum area ratio  $AR_{max}$  achievable without flow separation. This trend contrasts with that observed in conical diffusers and runs counter to initial expectations. However, this does not imply

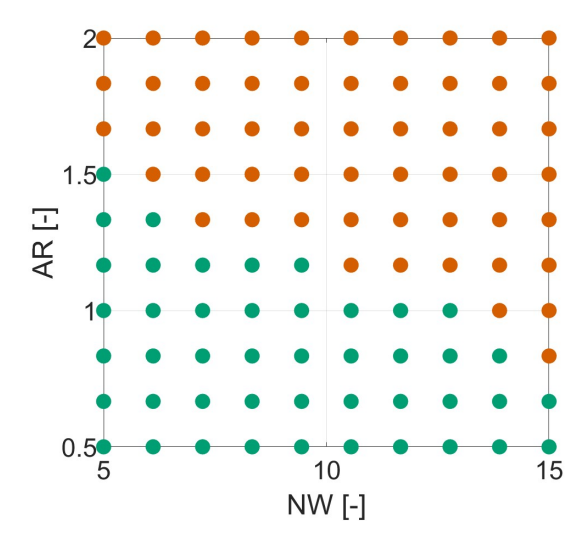


Figure 3.4: Separation in a radial channel - red dot indicates stall and green lack of stall

a decrease in the maximum pressure recovery coefficient  $Cp_{max}$ , as the prediction still supports that higher Cp values can be obtained with longer diffusers at a fixed AR. This is due to the fact that pressure recovery in radial diffusers, as shown with  $Cp_{ideal}$ , is also a function of NW through the radius ratio (RR). Yet still, due to the complex nature of flow separation and stall phenomena in radial diffusers, the Stratford criterion appears to be insufficient for accurately predicting the stall limit. The model lacks the representation of boundary layer–core flow interactions that appear to be more significant than in conical diffusers, thereby oversimplifying the actual flow behaviour.

#### 3.2 CFD

The same geometries evaluated using the 1D model were replicated with the CFD simulations. Inlet conditions were chosen to closely match those used in the 1D analysis, ensuring consistency in the flow regime. The simulations employed barotropic models, as described in section 2.3. The primary motivation for performing CFD on the same design points was to gain deeper insight into the flow behaviour and to assess the limitations of the 1D model, particularly its inability to predict stall phenomena in radial diffusers. Moreover, to assess the benefits of SC-CO2, reference cases were run with air.

Setting up a model with high quality mesh and properly stated boundary conditions takes time and is often a trial-and-error process, especially for SC-CO2. The boundary conditions outlined in Figure 3.5, represent the configurations under which the simulations achieved desirable convergence and numerical stability. Although, in principle, any physically admissible set of boundary conditions should be valid (as suggested by CFX documentation), practical implementation is often constrained by solver-specific factors such as relaxation parameters and iteration step sizes. These numerical considerations can lead to the solution entering unstable regimes, producing non-physical results. For instance, in the case of the radial diffuser, a boundary condition prescribing mass flow proved overly permissive, resulting in excessively high Mach numbers prior to simulation failure.

Table 3.1: Conical diffuser

|                                  | Air      | SC-CO2   |
|----------------------------------|----------|----------|
| $P_{0 \ in} \ [Pa]$              | 107417   | 8569011  |
| $\dot{m}_{out}  [\mathrm{kg/s}]$ | 0.037928 | 6.000489 |

Table 3.2: Radial diffuser

|                      | Air           | SC-CO2        |
|----------------------|---------------|---------------|
| $C_{in}$ [m/s]       | 136           | 136           |
| $\alpha_{in} [\deg]$ | 73.78, 70, 65 | 73.78, 70, 65 |
| $P_{out}$ [Pa]       | 105507.8      | 15000000      |

Figure 3.5: Boundary conditions for CFD simulations

#### 3.2.1 Conical diffuser

The three design points from section subsubsection 3.1.1 evaluated with 1D model are replicated with CFD. The results of those simulations are shown in this section. To compare the CFD results with 1D model results faithfully, it was aimed to select the same inlet conditions for both. However, as shown above, specifying boundary conditions in CFD software differs from imposing inlet values in 1D. Thus, the resulting inlet values vary slightly as shown in Table 3.3. However, as the deviation is negligible, the comparison is deemed to be valid.

| AR  | NW | V [m/s] | M [ - ] | P [ <b>Pa</b> ] | T [K] |
|-----|----|---------|---------|-----------------|-------|
| 1.6 | 3  | 58.4    | 0.3     | 80.1 e5         | 310   |
| 2.4 | 3  | 58.3    | 0.3     | 80.1 e5         | 310   |
| 3.0 | 3  | 58.3    | 0.3     | 80.1 e5         | 310   |

Table 3.3: Conical Diffuser inlet properties for selected design points

To provide deeper insight into the flow development within the diffuser, CFD contour plots are presented in Figure 3.6 and Figure 3.7. Three flow variables are visualized: static pressure, axial velocity, and total pressure. These results are shown for two geometries—one exhibiting gradual changes in area ratio and flow conditions (AR = 1.6), and another where flow reversal was observed and consequent decrease in pressure recovery(AR = 3).

Starting with the solution for fully attached flow, the CFD results in contour (**B.1**) Figure 3.6 indicate that the boundary layer develops along the wall, but no flow reversal is observed, as the axial velocity remains positive throughout the domain. From (**A.1**) Figure 3.6, the static pressure field exhibits a gradual, nearly one-dimensional distribution, with the outlet and inlet pressures remaining almost uniform. Furthermore, the total pressure field in (**C.1**) Figure 3.7 closely follows the velocity field, consistent with the expectation that dynamic pressure scales with the square of the velocity. However, upon closer look, it is visible that the values increase slightly at the core of the flow.

These observations suggest that the uniformity of the pressure field and no noticeable upstream effects make this case more amenable to accurate prediction by the 1D model. Although the velocity and total pressure distributions exhibit some two-dimensional characteristics due to thin boundary layer, it is deemed to be local and its effects captured by friction approximation. Moreover, the variation of the total pressure in the core flow can be attributed to the inability of the CFD software with barotropic model to evaluate total pressure values for compressible flow.



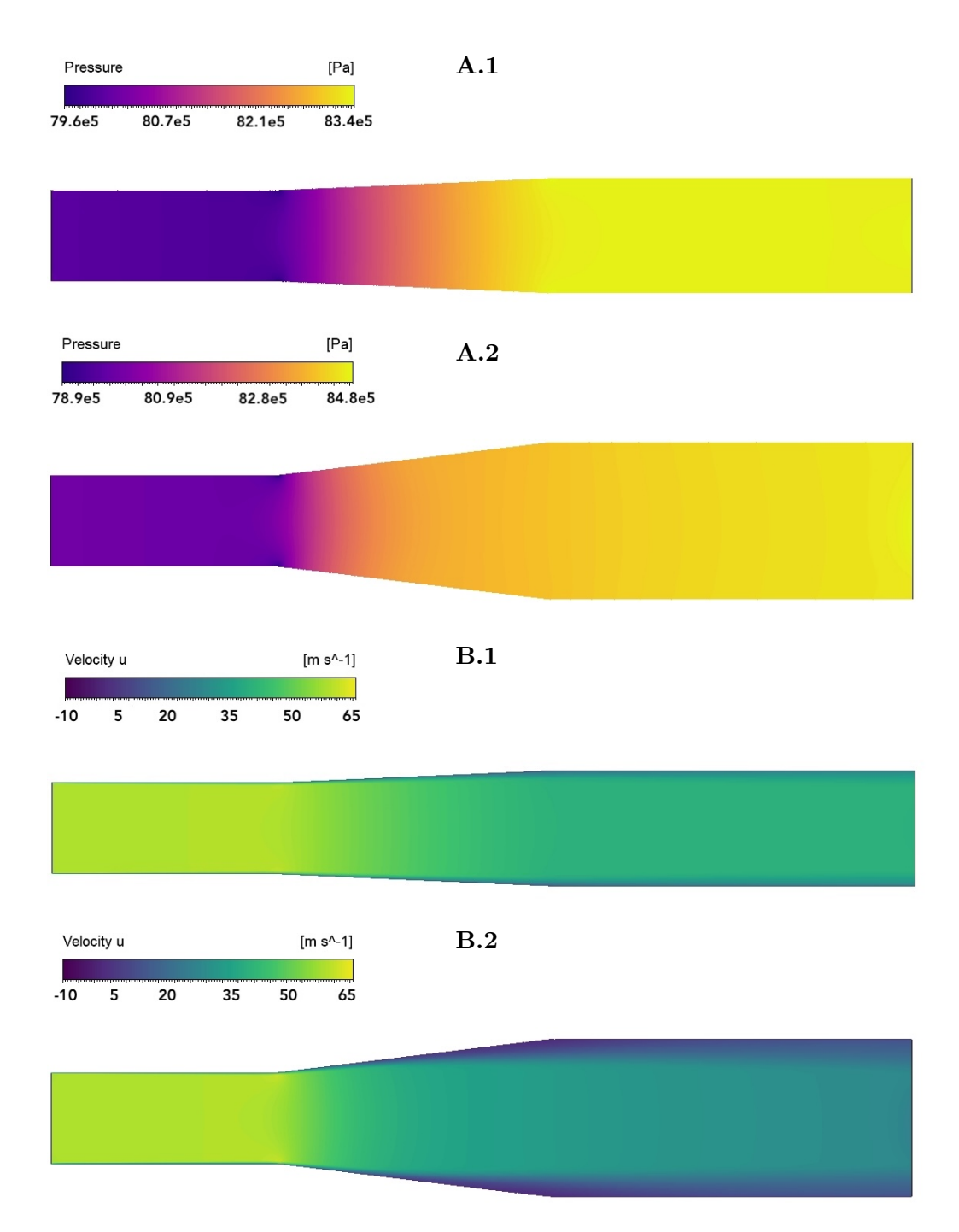


Figure 3.6: SC-CO2 flows in conical diffusers with NW=3 and fully attached AR=1.6 (1) and separated AR=3 (2). Fields of: Pressure (A), Velocity (B)

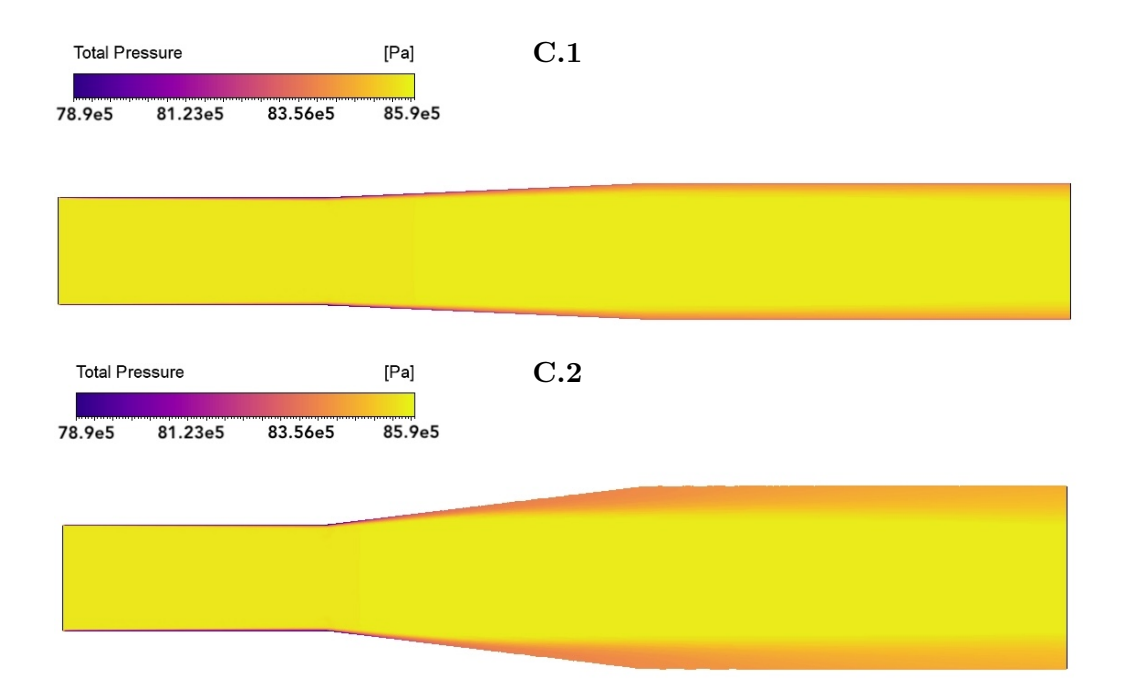


Figure 3.7: SC-CO2 flows in conical diffusers with NW=3 and fully attached AR=1.6 (1) and separated AR=3 (2). Field of Total Pressure (C).

Moving to the assessment of the flow field in a diffuser with separated flow, in Figure 3.6 (A.2), pressure field exhibits a nearly one-dimensional distribution normal to the diffuser walls, indicating uniformity across the cross-section. Looking at the end of the inlet, some upstream effects are visible. Another key observation is that, some pressure recovery still occurs at the outlet with constant area.

The 1D characteristics of pressure supports the underlying assumption in boundary layer theory that the pressure gradient normal to the wall  $(\frac{dp}{dy})$  is negligible, even in cases where the boundary layer appears separated. In inlet some upstream effect is visible due to significantly higher pressure occurring at the expanding section and slowing down the flow already before it leaves inlet. Finally, the continued pressure rise in the outlet is due to further flow expansion, as the walls no longer diverge significantly and thus allow the flow to reoccupy the passage.

In terms of boundary layer behaviour, best visible in Figure 3.6 (**B.2**), the simulation shows significant thickening of the boundary layer beginning roughly one-third into the expansion region. Near that point, areas of reversed flow (i.e. negative axial velocity) become apparent, indicating the onset of separation as given by the definition in Equation 1.17. However, as the flow proceeds into the outlet, the reversed velocity transitions back to positive, suggesting at least partial reattachment. This behaviour is consistent with boundary layer separation followed by gradual recovery, as the passage area ceases to increase and the flow is able to expand. This explains why there is noticeable pressure recovery in the outlet.

Lastly, the total pressure distribution in Figure 3.7 (C.2) reveals a distinctly two-dimensional profile, analogous to the velocity one. The core flow maintains a nearly constant total pressure, with a slight increase observed, likely due to barotropic model assuming an incompressible relation for total pressure. This region exhibits minimal viscous and turbulence (as was verified with eddy viscosity contour) losses, resembling ideal, inviscid behaviour where the conversion between static and dynamic pressure closely follows Euler's equation (Equation 1.1). In contrast, the boundary layer near the walls shows the most significant total pressure loss, attributed to high velocity gradients and high turbulence leading to associated shear stress. These mechanical energy losses dominate in the region of boundary layer separation, particularly in the expansion zone, where the lowest total pressure values



are observed. As the flow reattaches downstream, a partial recovery in total pressure is evident, further confirming the dynamic interaction between flow expansion, boundary layer development, and viscous dissipation.

To facilitate comparison between the 1D model results from Figure 3.1 and CFD results, two plots showing core flow values and one with averaged values are presented in Figure 3.8.

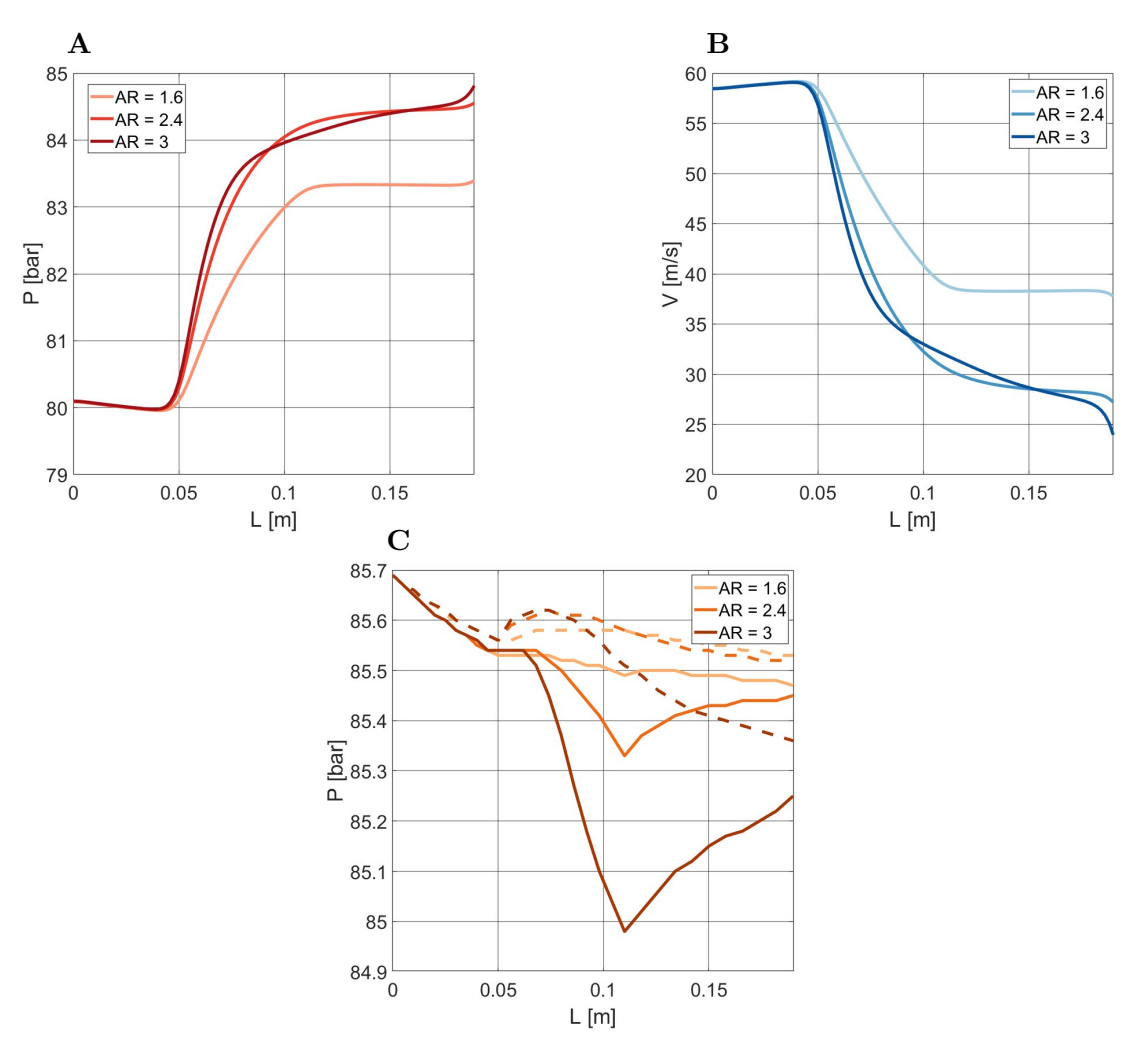


Figure 3.8: SC-CO2 CFD Results for NW = 3 at the middle of the profile. Plots of: (**A**) Pressure, (**B**) Velocity, (**C**) Total Pressure where dashed line is mass-flow-averaged and solid is area-averaged result.

The pressure distribution shown in Figure 3.8 (**A**) across the diffuser shows several notable trends. Initially, pressure decreases at the inlet region for all geometries, primarily due to wall friction, an effect consistent with predictions from the 1D model. However, 1D model overestimated largely the magnitude of that pressure drop. Within the expansion section, a steep pressure rise is observed, corresponding to the deceleration of flow as the cross section area increases. The gradient of this pressure recovery is strongly dependent on the rate of area change: for instance, at the highest area ratio (AR = 3), the pressure gradient is the steepest until around one third of length of the diffuser where boundary layer separation was identified in Figure 3.6 (**B.2**).

At the outlet, the pressure field behaves differently depending on AR. For AR = 1.6, pressure becomes nearly constant, suggesting that almost all of the flow expansion has already occurred within the designated expansion section. The losses due to friction are reduced compared to inlet due to the increased diameter and lower velocity. Thus, they do not manifest themselves as pressure drop,



as suggested by the 1D prediction. For AR = 2.4, gradual expansion continues beyond the formal expansion section, indicating that the flow did not reach its maximum expansion within the designated region. However, the pressure curve remains smooth, indicating no flow separation. This effect, is not visible in the 1D prediction. In the AR = 3 case, the pressure profile reveals a change in gradient within the expansion section, signalling the onset of boundary layer separation. Although pressure remains relatively uniform afterwards, further expansion continues until the diffuser exit, allowing some degree of pressure recovery despite the separation.

A consistent pressure rise is observed just before the outlet across all geometries; this is a numerical artifact attributed to boundary conditions at the outlet, where the solver resolves slightly higher core pressure than in the surrounding flow (as evidenced in Figure 3.6, particularly upon close inspection).

It is important to note that diffuser performance is evaluated between the inlet and outlet of the expansion section, excluding entrance and outlet effects. This approach isolates the intrinsic performance of the expansion geometry and ensures meaningful comparisons across designs.

From plot (B) Figure 3.8, velocity behaviour in core flow is investigated. The velocity profiles mirror the pressure distributions due to their coupling through the momentum equation. Regions of slower flow correspond to regions of higher pressure. The flow decelerates as the cross-sectional area increases, thereby enabling pressure recovery in accordance with diffuser function. As pressure decreases in inlet section, leading to higher density, velocity increases to satisfy continuity. This effect was not captured by 1D due to its accuracy.

For the geometry AR = 3, again, the trend indicating separation is clear. Around the same location where the gradient of pressure changes visibly, significant change of gradient of velocity takes place, again, pointing to pressure - kinetic energy exchange in core flow.

Whereas the pressure and velocity distributions can be reasonably discussed using core flow values, the total pressure at the core is not particularly meaningful in this context. It even shows a slight increase, due to implementation of the barotropic model. Therefore, to enable a more meaningful comparison with the 1D model predictions, area-averaged and mass-flow-averaged total pressure values are considered in Figure 3.8 plot  $(\mathbf{C})$  instead.

Due to lack of entropy information in the gas model, the total pressure is calculated by CFX from Equation 1.2. As barotropic model further assumes fixed relation between pressure and density, the total pressure is essentially a function of velocity and pressure fields. The values, when averaged across the cross-section, reveal distinct differences between area-averaged and mass-flow-averaged results. For all AR cases, area-averaged values are consistently lower. This is because the boundary layer, which is characterised by low total pressure values, occupies a larger proportion of the cross section area than the proportion of the mass carried within the boundary layer compared to the entire mass flow passing through the section.

In the inlet region, the boundary layer develops while the core flow accelerates slightly and decreases its pressure. As the velocity - pressure exchange occurs in core flow without significant losses, the low total pressure values will induce a modest but consistent drop in both area and mass-flow-averaged total pressure, nearly identical across all AR values due to having identical inlets.

A notable shift in total pressure trends occurs at the transition between the inlet and expansion sections. In the very initial portion of the expansion section (roughly until 0.07[m]), the area-averaged total pressure remains relatively constant—velocity drops while static pressure and density rise. However beyond the initial section of the expansion zone, as the boundary layer grows more significantly, it introduces a broader region of low total pressure, thereby reducing the area-averaged values. In contrast, the mass-flow-averaged total pressure initially increases in the expansion section. This occurs because the central core, which carries the majority of the mass, experiences increased static pressure and density, and the boundary layer remains relatively thin. As explained before, due to inaccuracy of CFD in calculating total pressure, the core values are overpredicted, hence, showing increasing values.



However, later as the boundary layer thickens further downstream and velocity is dissipated, both averages begin to decrease, with mass-flow one, continuing until the end.

Moving to the outlet zone, the area-averaged result produces a sharp change in two larger AR designs at the entrance to the outlet. This is an effect caused by the fact that the cross-sectional area of the outlet is constant and the boundary layer can finally start recovering. Thus, the values in boundary layer become higher again. Interestingly, the final values for the flows which did not experience separation (AR 1.6 and 2.4) converge to almost the same values. This could be explained by the fact that their losses could be almost solely attributed to friction. Furthermore, the slightly lower value for AR = 2.4 is consistent with expectations, as the wall length is longer due to the larger expansion angle (horizontal diffuser length remains fixed, but actual wall length increases with  $\alpha_{exp}$ , following  $L/\cos(\alpha_{exp})$ ).

Lastly, when referring to the results from 1D model in Figure 3.1, the values for total pressure in AR 1.6 and 2.4 are of similar magnitudes, however, 1D model puts higher emphasis on effect of hydraulic diameter than length, hence the prediction of lower final total pressure for lower expansion, opposite to the CFD result. This is the same effect that predicted significantly higher pressure drop in the inlet section.

## 3.2.2 Conical geometry based study SC-CO2 vs. Air

Finally, one of the key findings of the study can be presented. Using the CFD model, a series of simulations were performed for both SC-CO2 and air. To evaluate and compare the performance of these working fluids, the pressure recovery coefficient  $C_p$  was selected as the primary metric. Figure 3.9 shows two plots illustrating results for identical geometries using each fluid. Both simulations were carried out at the same inlet Mach number to ensure a consistent basis for comparison.

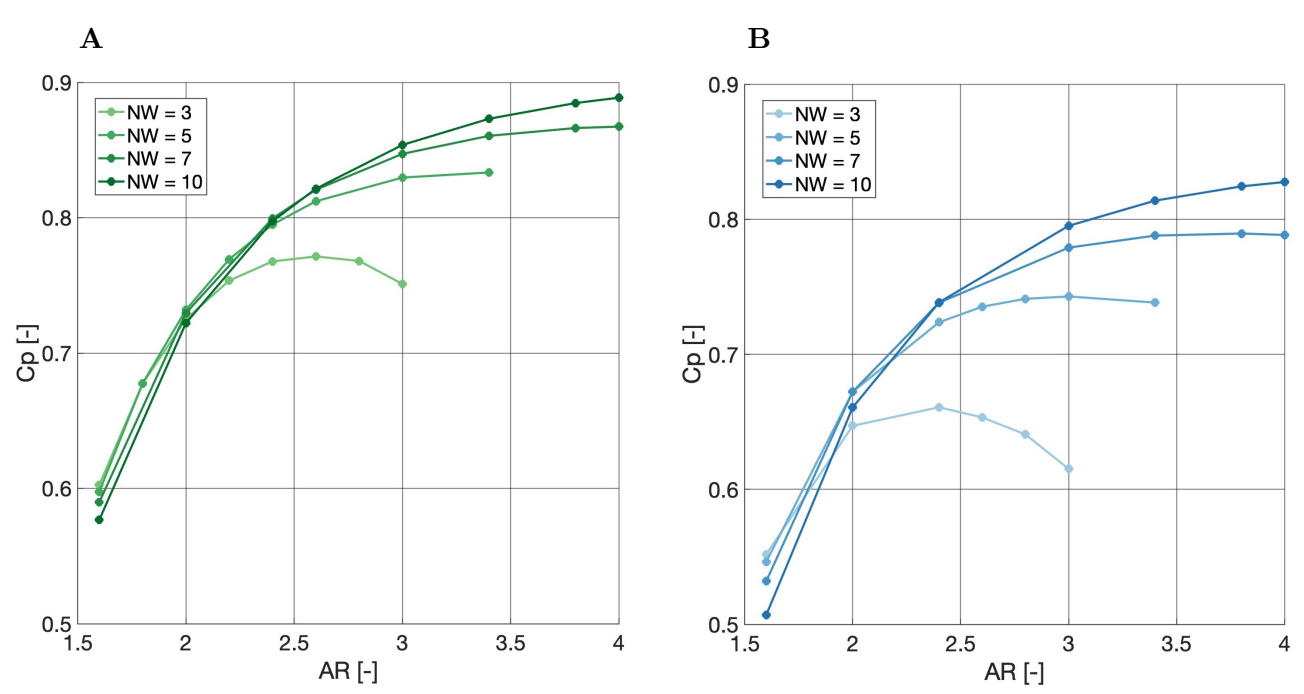


Figure 3.9: CFD Parametric study for  $M_{in} = 0.3$  (**A**) SC-CO2 and (**B**) Air.

To begin, the relationship between the pressure recovery coefficient  $C_p$  and the area ratio AR is examined. For each NW, the observed trends reflect the combined influence of wall friction and flow separation. For clarity, first the results corresponding to NW = 3 in  $\mathbf{A}$  are considered. At low area ratios AR < 2, the flow remains fully attached, and the boundary layer is relatively thin. Under these conditions, pressure losses are primarily attributable to wall friction. In contrast, when the same AR

**EPFL** 3.2 CFD

value is considered for a longer diffuser, such as the case with NW = 10, the resulting  $C_p$  values are noticeably lower. This reduction is a direct consequence of increased frictional losses associated with the larger wall surface, highlighting the sensitivity of  $C_p$  to diffuser length even when geometric expansion remains constant. The same trends are visible in the results with air.

However, as  $Cp_{max}$  is approached for NW=3 geometry, at AR=2.6, the curve starts flattening. This is due to the boundary layer being thicker with higher AR and finally reaching its maximum thickness before separating, shown in the Figure 3.6 (B.2). The AR for separation can be increased to achieve an overall higher Cp by decreasing the gradient of the pressure in axial direction. Thus, by choosing a design with a longer diffuser, the separation occurs later, with a much higher Cp. For instance for NW = 5 it is possible to reach AR = 3.4 without separation and achieve  $Cp \approx 0.82$ .

Thus, as explained in the introduction, on one hand, longer diffuser accumulated more frictional losses, but due to lower pressure gradient, the separation limit is delayed, enabling it to reach overall higher Cp.

By comparing the results for SC-CO2 in Figure 3.9 (A) with those for air under ambient-like conditions in Figure 3.9 (B), two key observations can be made. First, the pressure recovery coefficient Cp achieved with SC-CO2 is consistently higher across all geometries. Second, for a given NW, the onset of flow separation in SC-CO2 appears to occur at slightly higher area ratios AR compared to air. These two characteristics—enhanced pressure recovery and delayed separation—underscore the performance advantages of SC-CO2 and contribute to its attractiveness as a working fluid. Notably, these anticipated advantages were suggested in the introduction and served as a primary motivation for this investigation. The CFD results now, provide strong evidence in support of the initial hypothesis.

The higher values of Cp observed for SC-CO2 can be attributed to the high density as well as greater change in its value in SC-CO2 diffuser than in an air one (3.2% vs. 2.6%). By looking at the continuity equation ( $\dot{m} = \rho u A$ ), it is evident that both density and cross-sectional area increase will lead to velocity reduction. As in SC-CO<sub>2</sub>,  $\rho$  variation is larger, the velocity reduction will be higher than in air. Lower velocity translates to higher pressure due to kinetic energy - pressure exchange. Moreover, by inspecting Equation 1.1, it is clear that not only the flow deceleration dV is of importance but also the  $\rho$  value itself. Thus, a flow with its higher absolute value will achieve higher pressure recovery.

The influence of working fluid on separation can be best assessed by investigating the critical geometry. With the data in Figure 3.9, a linear function for maximum AR achievable without separation for given NW can be derived. It is given for SC-CO2 and air respectively:

$$AR_{max} = 0.35 \cdot NW + 1.58 \tag{3.3}$$

$$AR_{max} = 0.35 \cdot NW + 1.32 \tag{3.4}$$

As the slope of the two functions is the same, it can be deduced that the separation mechanism remained consistent between two fluids. However, in SC-CO<sub>2</sub>, the stall line is positioned above the result for air, indicating that the maximum allowable adverse pressure gradient that SC-CO2 can withstand is higher.

The delay in flow separation in SC-CO2 can be explained in two ways. First, more intuitive and qualitative, points to the fact that SC-CO2 flow carries more momentum, due to its high density. Thanks to that, it can withstand higher adverse pressure gradient, as it is more difficult to slow it down.

Second explanation is more quantitive and revolves around looking at Equation 2.5. The first compatibility equation, a check of the boundary layer profile at the wall, provides good insight into how SC-CO2 properties may affect the separation onset. Firstly, investigating the viscosity of SC-CO2, it is found to be higher, than for air. The sum of the two terms on the RHS of Equation 2.5 is positive just before separation as the profile is already concave due to adverse pressure gradient.



However, with higher viscosity, the magnitude of the RHS is lower. Thus, higher pressure gradient is needed to make it "excessively" concave to actually produce flow reversal. Thus higher viscosity of SC-CO2 adds more stability to the boundary layer.

Secondly, looking at the second term of the RHS of Equation 2.5 the influence of turbulence can be assessed. As explained before, it plays an essential role in delaying flow separation due to the product  $\overline{u'v'}$  being negative in boundary layers. The value of that product is consistently significantly higher in SC-CO2 than in air as suggested by eddy viscosity results. Moreover, also density is significantly higher. Thus the second term in the RHS of Equation 2.5 will be larger for SC-CO2 than for air, allowing for higher pressure gradient without excessively concave boundary layer, leading to separation.

#### 3.2.3 Radial diffuser

Proceeding to the evaluation of the radial diffuser, the three design points previously examined using the 1D model in Section 3.1.2 are now analysed through CFD simulations. In order to ensure a meaningful comparison between the two modelling approaches, an effort was made to maintain consistent inlet conditions across both methods. However, as indicated in Figure 3.2, the boundary conditions that provided satisfactory convergence in the CFD simulations were specified as inlet velocity and outlet static pressure.

As a consequence, the resulting inlet thermodynamic properties exhibit some variation due to pressure recovery based on diffuser geometry. They are summarized in Table 3.4. Despite this, the maximum deviation in inlet pressure across the design points remains below 4%. This relatively small discrepancy suggests that the operating conditions remain within the same flow regime, and thus the results from CFD and 1D models can be considered comparable for the purpose of performance analysis.

| AR   | NW   | V [m/s] | M [ - ] | P [ <b>Pa</b> ] | T [K] |
|------|------|---------|---------|-----------------|-------|
| 1.00 | 5.42 | 135.8   | 0.50    | 134.92 e5       | 364   |
| 1.65 | 5.42 | 135.8   | 0.50    | $132.75 \ e5$   | 364   |
| 2.00 | 5.42 | 135.8   | 0.50    | 133.75 e5       | 364   |

Table 3.4: Radial Diffuser Alpha = 65[deg] inlet properties

In the same manner that CFD contour plots were discussed in section 3.2.1 of the conical diffuser, this section will provide insight for radial diffuser. The Figure 3.10 provides flow contour plots of pressure, velocity and density for one flow with benign change due to low AR (1) and the second for a case where significant separation occurred (2). Notable difference in the radial contour plots is that the flow is actually swirling throughout the diffuser, thus, to simplify the visualisation of a flow path, black and red lines were added, showing 2D and 3D streamlines respectively.

The CFD results for the attached flow case exhibit several key characteristics across multiple flow variables. Firstly, the pressure distribution in Figure 3.10 (A.1) shows a smooth and nearly one-dimensional profile, with negligible pressure gradient in the direction normal to the walls. The gradual deceleration of the flow allows a consistent conversion of kinetic energy into pressure, with the most pronounced pressure increase occurring near the diffuser inlet, which is consistent with predictions from the 1D model. The near one-dimensional nature of the pressure field confirms that the assumptions underlying the 1D model are valid in this regime.

As explained before, in a straight wall diffuser, the area does not scale linearly with radius. Thus for the AR = 1, the initial geometry exhibits a slight increase in cross-sectional area, which promotes flow expansion and pressure recovery. Moreover, as explained before, in radial diffusers, also the length of the diffuser strongly influences pressure recovery (due to term RR in Equation 1.6). This

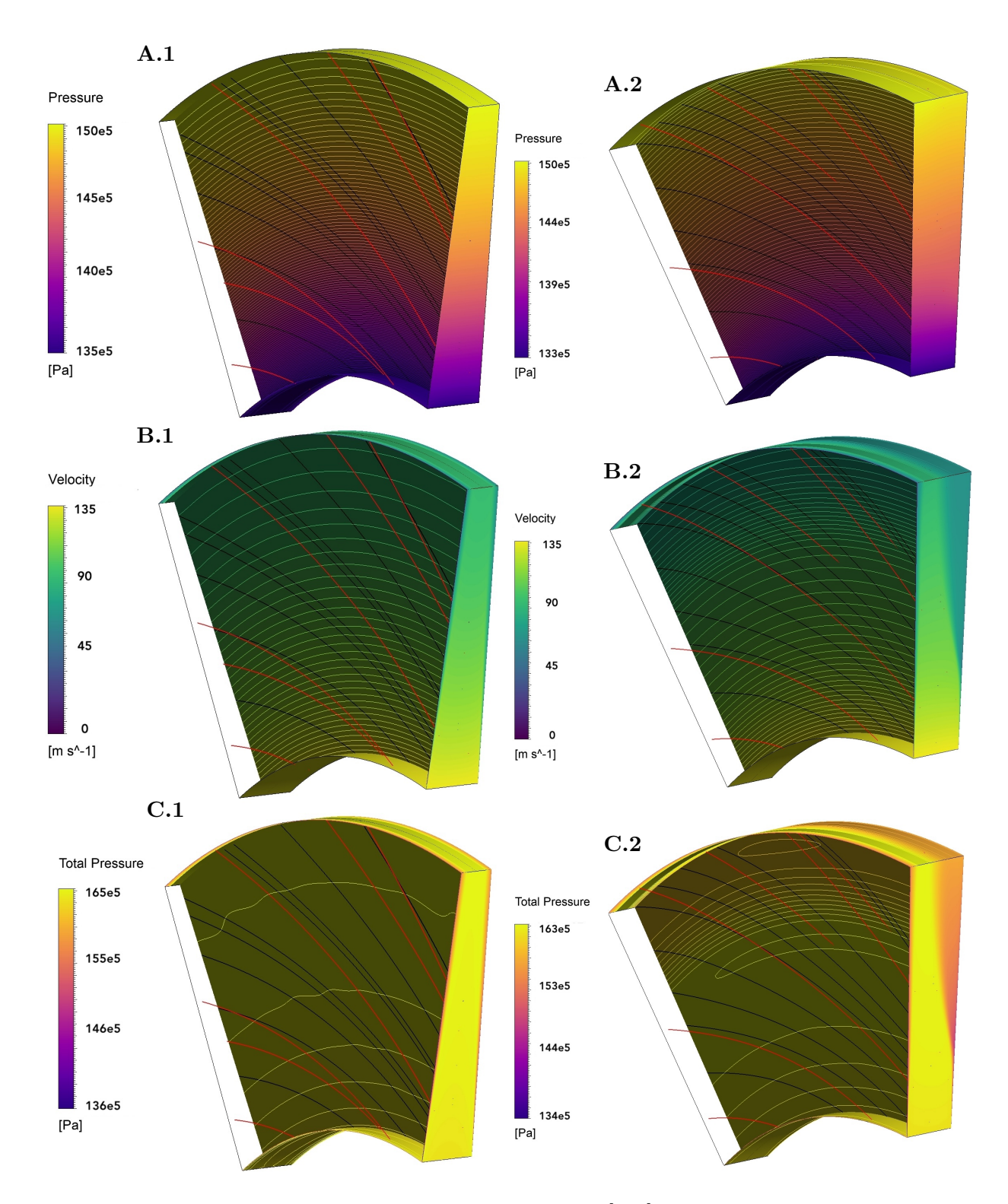


Figure 3.10: SC-CO2 flows in radial diffusers with  $\alpha_{in} = 65 [\deg] NW = 5.52$  and fully attached AR = 1.00 (1) and separated AR = 2.00 (2). Fields of: (A) Pressure, (B) Velocity, (C) Total Pressure. Black and red lines are flow 2D and 3D streamlines respectively.



was explained to take place because of the decrease of the flow angle  $\alpha$ . It is now possible to validate that hypothesis by inspecting the streamlines obtained from CFD, visible in contour in Figure 3.10 (A.1). Both 2D and 3D streamline deflect significantly from a constant angle shape cure. It may be difficult to state that just by visual observation, however, with access to the CFD data the  $\alpha_{out}$  was measured and it was indeed lower than  $\alpha_{in}$ . Therefore, the 1D model's observations concerning the evolution of  $\alpha$  are supported by the CFD findings.

For the velocity field Figure 3.10 (**B.1**) is addressed. No tangential velocity gradient is observed, and the boundary layer remains thin throughout. Furthermore, the low AR leads to a weak adverse pressure gradient, which in turn results in slow boundary layer growth. The gradual reduction in velocity is facilitated by the changing of the  $\alpha_{in}$ , as explained above. The smooth profile of pressure and velocity fields point to this case being appropriate for modelling with a 1D model, such as introduced before.

Regarding total pressure from Figure 3.10 (C.1), the core flow maintains a nearly constant value, with marginal increase in the core as shown with the iso-lines in the side view, particularly near the outlet. This effect is again attributed to limitations of the barotropic model. As with the conical diffuser, total pressure losses are primarily confined to the boundary layer, where elevated velocity gradients enhance viscous dissipation.

In the case of separated flow, the pressure field Figure 3.10 ( $\mathbf{A.2}$ ) remains remarkably uniform in the direction normal to the walls, even in the presence of unsteady separation. This observation implies that the pressure measured at the centreline of the flow width, as shown in Figure 3.11 ( $\mathbf{A}$ ), remains representative of the overall pressure distribution. Consequently, comparisons with 1D model that assumes uniform pressure across the cross-section remain valid despite the presence of flow separation.

The velocity field Figure 3.10 (**B.2**) reveals that the flow becomes asymmetrically attached to one side of the channel, with the boundary layer dominating the outlet region. This behaviour arises from flow separation induced by excessive expansion, leading to a quasi-transient state. As a result, the simulation residuals do not fully converge, indicating the presence of unresolved unsteady behaviour. A transient simulation would be required for a more accurate capture of these dynamics. Additionally, boundary layer growth is significantly more pronounced than in conical diffusers. Although the NW may be of similar order, the effective path length in radial diffusers is extended due to the swirling flow, which enhances boundary layer development. Furthermore, the larger AR also contributes to the effective flow path length significantly.

The total pressure field Figure 3.10 (C.2) closely resembles the velocity field and exhibits non-uniformity in both radial and axial directions. This correspondence can be explained by the barotropic gas model, where total pressure is given by Equation 1.2. Since pressure (and thus density) is approximately constant in the width-wise direction, spatial variations in total pressure are governed predominantly by the velocity distribution. The non-uniformity observed in the tangential direction is likely attributable to the unsteady flow regime and the incomplete convergence of residuals, which remained above 1e-6.

To facilitate comparison between the 1D model results from Figure 3.3 and CFD results, two plots showing core flow values and one with averaged values are presented in Figure 3.11.

Pressure evolution observed in Figure 3.11 (A) increases throughout the domain for all three design points. Each case has different inlet pressure and the same outlet pressure due to selection of boundary conditions in CFD. However, as explained before, the regime is comparable.

Among the results for three geometries, the case with the highest area ratio AR = 2, which exhibits flow separation as discussed before from Figure 3.10 (**B.2**), is the only one where the pressure gradient trend changes mid-domain. This occurs around R = 0.047[m] and can be indicative of a location of onset of boundary layer reversal. The pressure evolution for AR = 2 highlights that, despite its larger AR, the separated flow design performs worse in terms of pressure recovery due to separation losses

accumulation, clearly visible through the pressure difference ( $\Delta P$ ) between inlet and outlet.

Furthermore, the pressure gradient is steepest near the inlet, which corresponds to the rapidly increasing cross sectional area in this region, and inducing of the  $\alpha$  change as was hypothesised in the 1D model results.

Similarly to the fixed outlet pressure in Figure 3.11 (A) between different AR, the inlet velocity is fixed in Figure 3.11 (B) due to inlet boundary condition of flow velocity. Inspection of the velocity evolution indicates that velocity profiles for the non-separated cases closely mirror the corresponding pressure trends, as measured at the core flow. However, for the separated case (AR = 2), a notable deviation occurs: the point of abrupt change in the velocity profile does not align exactly with the pressure trend break. This discrepancy stems from the unsteady nature of the separated flow in this example, where the core flow becomes asymmetric, often attaching to one wall. As a result, the flow field becomes quasi-transient and convergence is not fully achieved. During separation, the boundary layer grows to occupy a significant portion of the diffuser width and crosses into the center line. Therefore, velocity measured at the channel midline no longer represents true core flow conditions.

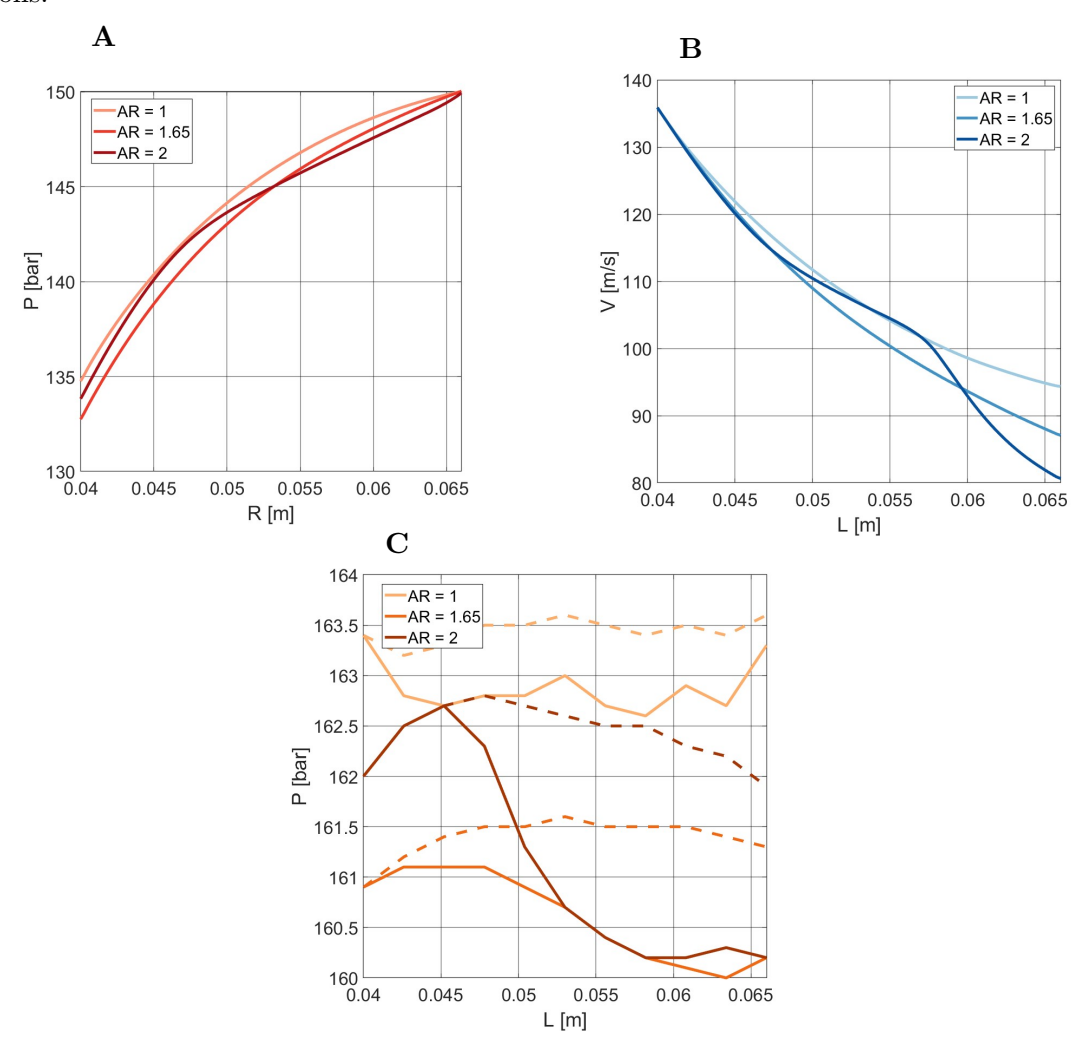
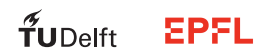


Figure 3.11: SC-CO2 CFD Results for NW = 5.42 at the centreline of the profile. Plots of: (A) Pressure, (B) Velocity, (C) Total Pressure where dashed line is mass-flow-averaged and solid is area-averaged result.

Comparing area-averaged and mass-flow-averaged total pressure plots from Figure 3.11 ( $\mathbf{C}$ ) reveals a few interesting features. The initial values are different for each case. This is due to having fixed



velocity and different static pressure between the designs. A general trend is that area-averaged values are consistently lower due to the influence of boundary layer regions where total pressure is reduced. However, mass-flow averaging assigns lower weight to these low-velocity (and thus lower  $P_0$ ) boundary layer zones, resulting in higher averaged values.

In the AR=1 case, where the flow remains largely attached and losses are minimal, distinguishing trends in total pressure is more challenging. As shown in Figure 3.10 ( $\mathbf{C}$ ), the boundary layer thickness increases towards the outlet, thinning the core region. Therefore, if inlet and outlet mass-averaged values remain equal, the total pressure in the core must have increased, suggesting again shortcoming of barotropic model in prediction of total pressure. It is not possible to see the effect of friction just by inspection of the plot.

The prediction of the increase of mass-flow averaged total pressure across all the designs is in general attributed to the barotropic model assumption of incompressibility between static and total values.

Regarding, the separated case (AR = 2), it is partially in line with expectations. It shows the highest drop in total pressure value. This is a case for area as well as mass-flow averaged result. The trends are comparable to the AR = 1.65 design, suggesting that the losses due to separation may be looked at as the difference between results of the two (normalized with their  $P_0$  inlet values).

### 3.2.4 Effect of Inlet Flow Angle on Pressure Recovery

Another parameter of interest in radial diffuser flow is the the inlet flow angle,  $\alpha_{in}$ . It plays a crucial role in determining the pressure recovery performance and stall characteristics of radial diffusers. While increasing  $\alpha_{in}$  can, in theory, enhance Cp by extending the flow path and promoting more effective diffusion, it also introduces the risk of flow separation and stall.

Figure 3.12 presents the influence of inlet flow angle  $(\alpha_{in})$  on the pressure recovery coefficient (by means of Cp) for a fixed-geometry radial diffuser. The CFD results indicate that increasing  $\alpha_{in}$  initially improves Cp, as longer streamlines enhance flow turning and facilitate more effective kinetic energy pressure conversion. This behaviour aligns with the idealized trend predicted by Equation 1.6, where a higher  $\alpha_{in}$  increases  $C_p$ .

However, the ideal relation assumes  $\alpha_{in}$  can increase without bound, peaking at  $\alpha_{in} = 90^{\circ}$ , which corresponds to a fully tangential flow. This scenario is clearly unrealistic. CFD simulations reveal that beyond  $\alpha_{in} \approx 75^{\circ}$  for diffuser with AR = 1 and NW = 5.42, flow separation occurs, causing a sharp decline in Cp. The onset of stall can be attributed to a reduction in radial momentum, which compromises the flow's ability to counteract the adverse pressure gradient. Moreover, higher  $\alpha_{in}$  leads to longer streamlines and increased boundary layer development, eventually reducing the effective core flow area. As shown in Figure 3.10 (B.2), this boundary layer thickening can cause the core flow to vanish entirely, even though the local pressure gradient may remain modest. However, the true nature of the critical inlet angle is more complex and the analytical modelling of that phenomenon could be a subject of a separate study(29). This points to the difficulty or even implausibility of capturing stall effect in 1D modelling.

Additional parametric studies (presented in the appendix) confirm that higher Cp values can be achieved at lower  $\alpha_{in}$  when combined with larger AR. These findings underline the critical role of radial stall in diffuser performance and demonstrate that reducing  $\alpha_{in}$  has a stabilizing effect, delaying separation and improving overall pressure recovery.

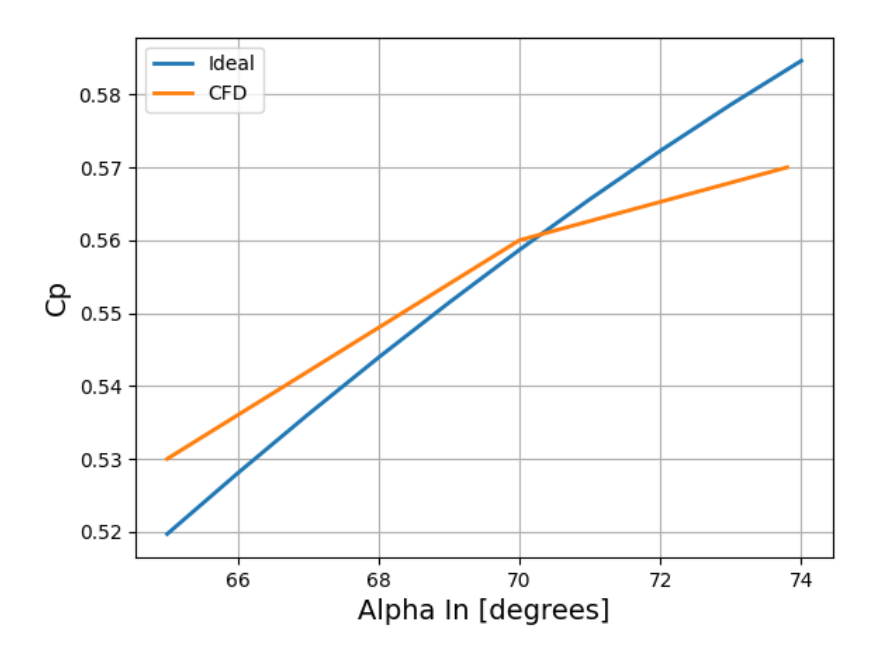


Figure 3.12: Effect of inlet angle  $\alpha_{in}$  on pressure coefficient in radial diffuser with AR = 1 and NW = 5.42

## 3.2.5 Radial geometry based study SC-CO2 vs. Air

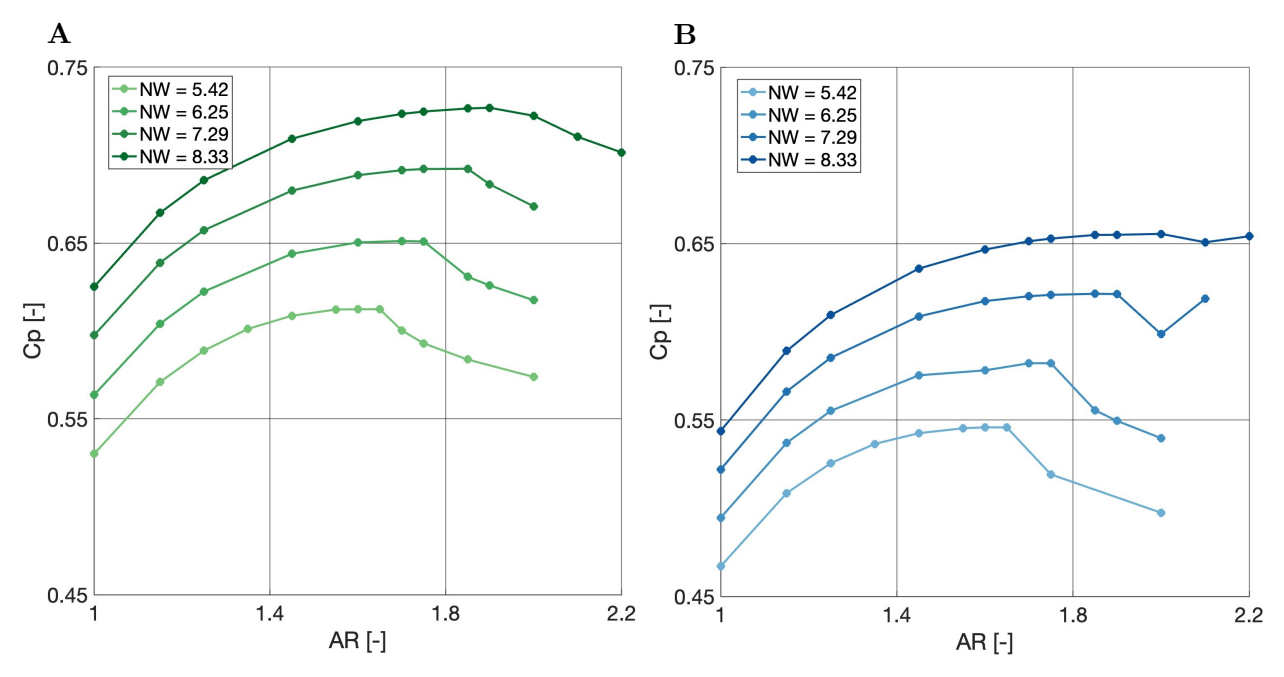


Figure 3.13: CFD Parametric study for  $M_{in} = 0.5$  at  $\alpha_{in} = 65 [\deg]$  (A) SC-CO2 and (B) Air.

Finally, the crucial findings of the study are presented. The CFD analysis reveals that the maximum pressure recovery,  $Cp_{max}$ , for air occurs at approximately the same area ratio,  $AR_{max}$ , as for SC-CO2 when the NW, is fixed. However, the magnitude of Cp achieved with SC-CO2 is significantly higher than that for air, underscoring the enhanced compressibility and expansion characteristics of the supercritical fluid leading to greater capacity for flow deceleration as explained when discussing the conical diffuser.



Furthermore, increasing NW shifts  $AR_{max}$  to higher values, a trend contrary to predictions from the 1D separation model. Notably, higher values of NW result in substantially greater  $C_p$  values. Furthermore, the trend outlined by the ideal relation (Equation 1.6) and 1D model of positive influence of the length of the diffuser on pressure recovery is confirmed.

The critical geometry can be again benchmarked with a trend that fits the dataset best. In case of a conical diffuser, a linear trend was sufficient, however, in radial diffuser, a quadratic trend seems to be more appropriate. Given the results in Figure 3.13, SC-CO2 seem to be limited by the same  $AR_{max}$  for given NW, despite a bit higher values at NW = 7.29 and NW = 8.33 for air. Thus, only one expression that is said to fit both is provided.

$$AR_{max} = -0.019 \cdot NW^2 + 0.34 \cdot NW + 0.33 \tag{3.5}$$

These findings suggest that the critical geometry of radial diffusers does not need to be fundamentally altered when switching from air to SC-CO2, as the underlying stall mechanisms, driven by the similar maximum adverse pressure gradient, remain similar.

## 3.3 1D vs. CFD Performance Prediction Comparison

In the two previous sections, results for 1D and CFD models were presented separately. Certain trends in flow evolution were discussed and some differences between models highlighted. Thus, the major shortcomings of the 1D model, such as: lack of upstream effects, boundary layer growth neglection, lack of pressure recovery modelling after separation, no turbulence and viscosity inclusion other than through Cf, semi-empirical assumption on total pressure drop, and more, are clear. In this section, the effects of those assumptions are portrayed through a systematic assessment via a performance metric Cp and underlying frictional effects via Cf.

#### 3.3.1 Friction Coefficient in Axial Flow

The CFD model, was firstly used to compare friction models from literature to a result obtained from a simulation. The objective here was to determine the influence of the friction solely, thus a simulation for AR = 1, a straight pipe, was conducted. In a pipe, flow does not experience expansion and losses due to adverse pressure gradient boundary layer build up and separation. Thus, the measured loss can be said to be stemming only from friction.

As the simulations was conducted with a RANS k-omega SST model, the shear stress measured in the flow is evaluated through Equation 1.8, which will include the effect of viscosity as well as turbulence. This will also have consequence for total pressure evolution throughout the pipe, that is expected to decrease more than it would just because of viscosity. However, as modelled eddy viscosity is an approximation of the true complexity of a turbulent flow, it is important to visualise how it relates to experimental data, for which the models from literature were derived. In the Figure 3.14 results from CFD simulations are compared to the values for corresponding flow conditions determined with friction models from literature.

In the Figure 3.14 there are two results addressed 'CFD 1' and 'CFD 2'. They are both from the same simulation, but they were calculated using different expressions. The 'CFD 1' was evaluated by first obtaining friction factor f using the semi-empirical expression with total pressure drop from Equation 1.11 and then converting it into Cf with Equation 1.12. The 'CFD 2' was found by using the more analytical expression based on the shear stress at the wall as given by Equation 1.9.

The CFD results reveal several key observations. First, in both simulation approaches, the skin friction coefficient Cf decreases along the pipe length. Secondly, the shear-stress-based method yields a lower Cf value compared to the method derived from total pressure loss. Additionally, the Cf models from literature appear nearly constant at the scale of the tunnel, with variations so minor that

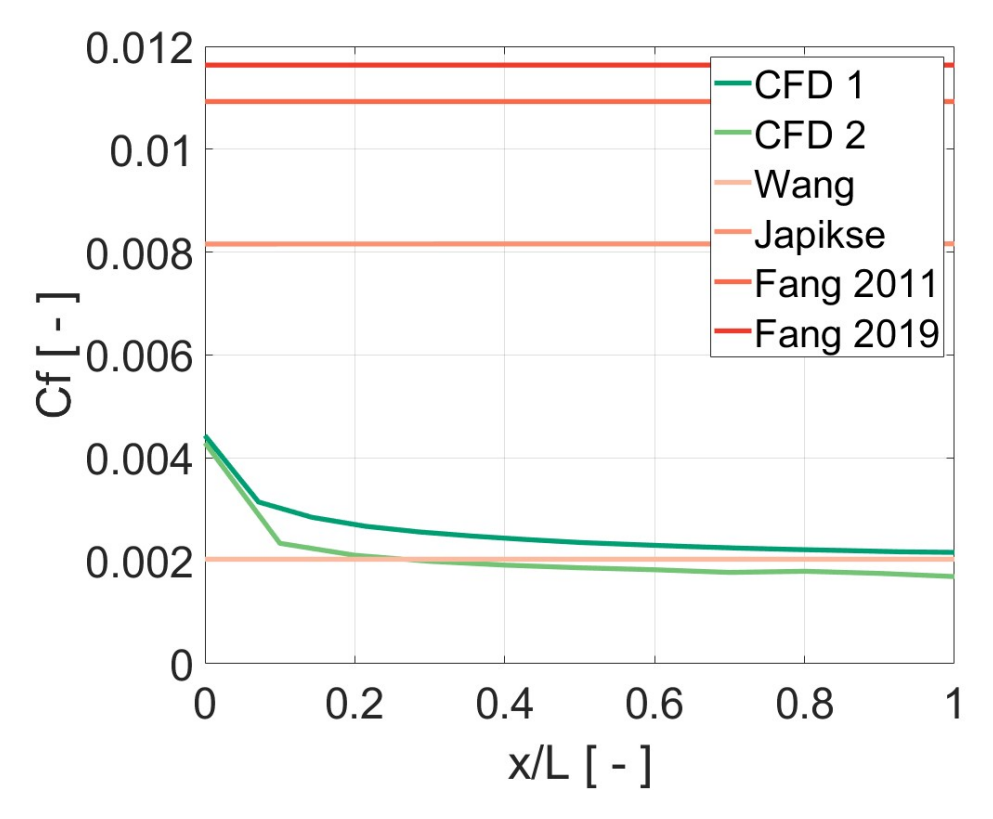


Figure 3.14: Comparison of friction coefficient Cf along a pipe for SC-CO2 flow. Result CFD 1 calculates Cf from the total pressure drop between monitoring stations, while CFD Case 2 derives Cf from the wall shear stress. Additional Cf values were obtained using friction models from literature, based on the same inlet flow conditions as the CFD simulations.

they are not visually distinguishable in the plots. Among these, the model proposed by Wang et al. demonstrates the closest agreement with the CFD - based Cf values.

This behaviour can be explained as follows: the initial section of the pipe experiences the highest velocity gradient  $(\frac{du}{dy})$  near the wall due to boundary layer development, resulting in elevated shear stress and, consequently, a greater initial drop in total pressure. As the flow progresses, the boundary layer thickens, reducing the local velocity gradient and wall friction, which in turn lowers the Cf. As flow is not experiencing any expansion induced by changing cross sectional area, the boundary layer remains almost constant after x/L = 0.3. Hence the Cf profile predicted by both CFD methods.

Moreover, the total pressure drop is influenced not only by wall shear stress  $\tau_{wall}$  but also by the losses in the entire boundary layer, which are a consequence of shear stresses in a larger region of the flow. As a result, the Cf derived from total pressure loss (despite not having accurate values due to barotropic model) is higher than that calculated purely from shear stress at the wall.

Most literature-based models for Cf are primarily functions of geometry and exhibit only weak sensitivity to fluid properties, which are included through Re (and Ch in Fang et. al 2020). The strong agreement of Wang's model with the CFD-derived Cf suggests it may be the most appropriate choice for use in the 1D conical model. This is likely because Wang's correlation was developed specifically for SC-CO2, whereas the models: Fang 2011, and Fang 2019 were formulated for a broader range of supercritical fluids. Interestingly, the Japikse model, despite being originally developed for ideal gas flows, shows second best agreement with CFD results.



### 3.3.2 Conical geometry based study 1D vs. CFD

To assess the predictive capability of 1D modelling approach in conical diffuser, a comparative study was conducted against CFD results. To achieve that goal, the metric of Cp was adopted. The analysis is carried out across the range of area ratios AR tested previously with CFD. The Figure 3.15 presents the comparison of 1D model predictions with different friction models against CFD results for two representative cases: NW = 3 and NW = 5. These cases provide insight into the influence of channel length on flow behaviour and model fidelity.

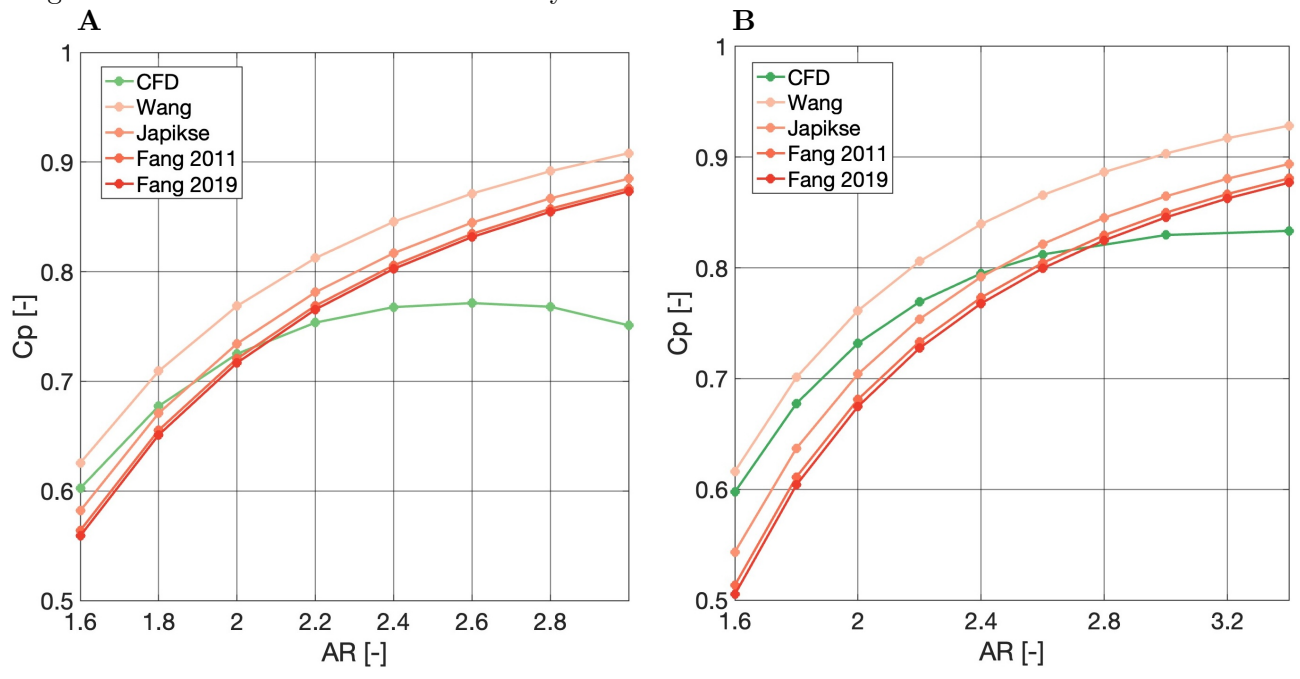


Figure 3.15: Pressure recovery as a function of AR, comparison with 1D model results with Cf models from literature. (**A**) NW = 3 (**B**) NW = 5.

The comparison of 1D and CFD results shows that, for lower area ratios AR, the predictions from the 1D model align closely with those from CFD. At low AR geometries, boundary layer development is limited and separation losses are minimal. In such cases, the flow resembles pipe flow conditions, for which SC-CO2 friction models used in the 1D simulations, were originally formulated. As a result, the inclusion of frictional effects provides an accurate approximation.

For longer channel, NW=5, the agreement between the 1D model and CFD results improves further, even at higher AR values leading up to separation. This trend is evident in Figure 3.15(**B**), where separation is delayed due to the extended diffuser length, allowing the flow to remain attached for longer, and separate less abruptly. Thus, influence of the boundary layer build up and separation is visible later, allowing 1D modelling to predict the flow better.

Among the friction models assessed, Wang's model exhibits the best overall agreement with CFD data, followed by Japikse's model. The superior performance of Wang's correlation is likely due to the nature of the experimental database on which it was based as suggested before. It was the only model developed specifically for SC-CO2. This is again consistent with the result found from Figure 3.14.

### 3.3.3 Friction Coefficient in Radial Flow

Similarly to the section 3.3.1, it is important to verify if the friction models from literature are suitable for radial diffuser flow by comparing them with values from CFD. The notable difference between axial, pipe flow and the radial flow is that boundary layer and flow turbulence could be significantly different, leading to different values of Cf as per Equation 1.8. In order to assess purely the effect of friction, not influenced boundary layer growth due to expansion, a geometry of a radial diffuser with AR = 1 was tested. As shown before, such a geometry will still develop pressure recovery due to the changing angle  $\alpha$  of the flow, however, the change with respect to boundary layer is still relatively benign. In the Figure 3.16 Cf value extracted from the CFD simulation is presented against the models found in literature.

The CFD result in the Figure 3.16 was obtained through the relation for  $\tau_{wall}$ . The initially higher values are again indicative of boundary layer formation at the beginning. Further, as the boundary is more developed it does not grow as fast, leading to relatively constant value of Cf measured.

The value found in radial diffuser is indeed different to the one shown in a pipe flow (Figure 3.14), however, this difference is marginal. Thus, one more time, the Wang's model proves to be the best fit.

What merits attention, is the model of Japikse predicts some variation in Cf as the flow develops throughout the diffuser. As Japikse is specifically intended for use in radial diffusers, this evolution could be intended by the design, to account for higher losses at the outlet where boundary layer grows higher. Thus, including implicitly more losses than just friction.

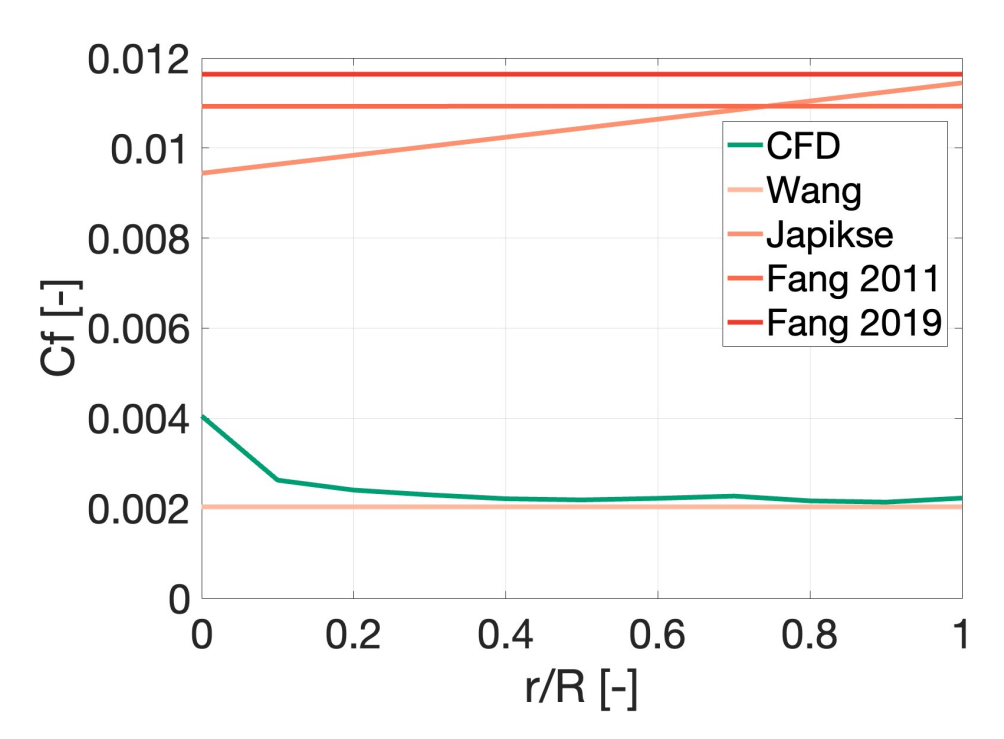
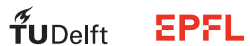


Figure 3.16: Comparison of friction coefficient Cf along radius of radial diffuser for SC-CO2 flow. Result CFD derives Cf from the wall shear stress. Additional Cf values were obtained using friction models from literature, based on the same inlet flow conditions as the CFD simulations.

M. Dabrowski 39 of 56 June 2025



### 3.3.4 Radial Geometry based study 1D vs CFD

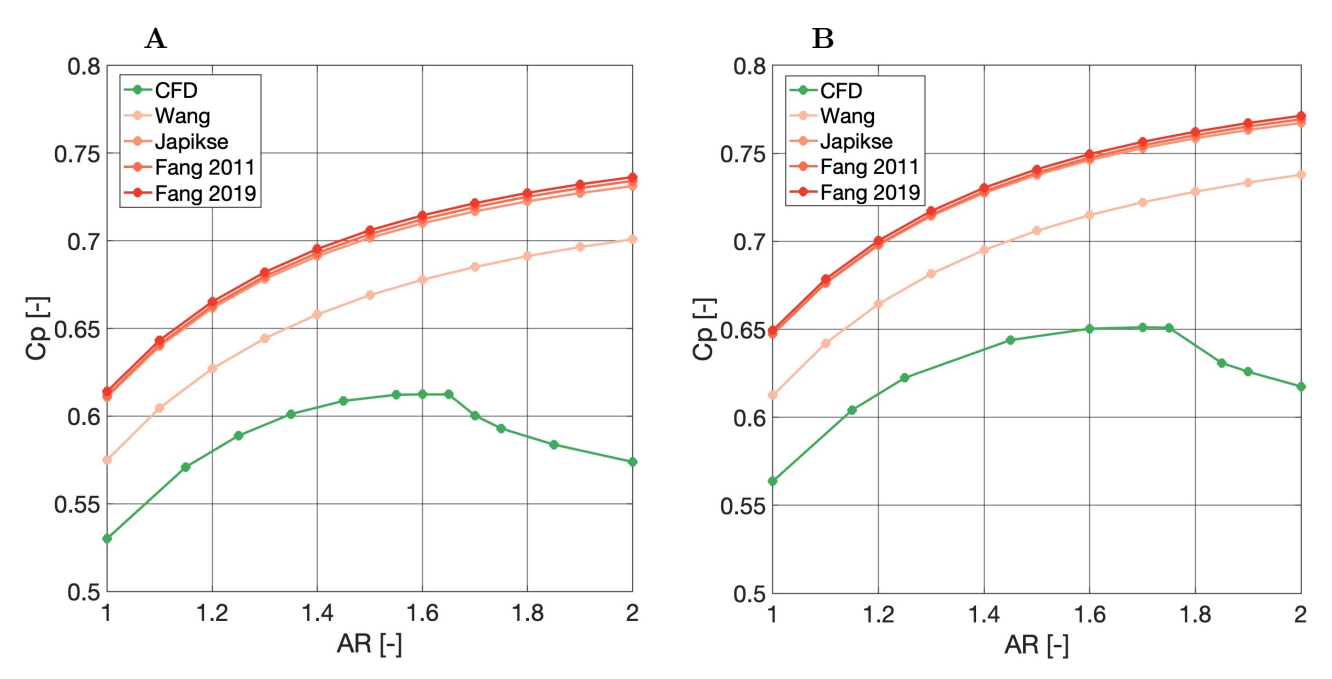


Figure 3.17: Pressure recovery as a function of AR at  $\alpha_{in} = 65[\deg]$ , comparison with 1D model results with Cf models from literature.( **A**) NW = 5.42 (**B**) NW = 6.25.

The analysis in Figure 3.17 shows that all evaluated 1D friction models tend to overpredict the pressure recovery largely when compared to CFD results. It is likely attributable to the dual application of the friction coefficient, Cf, within the 1D framework. In the current implementation, Cf is used both to calculate wall shear stress,  $\tau_{wall}$ , and to estimate the loss in total pressure,  $dP_0$ . As it was shown in Figure 3.16, the shear wall value predicted by Wang's model is very close to the CFD result, suggesting that the limitation resides in the calculation of  $dP_0$  in the 1D model.

This discrepancy becomes more pronounced as AR increases, indicating a growing deviation between 1D predictions and real flow behaviour under greater expansion. This happens as the boundary layer grows, and the flow approaches separation, which is not modelled by 1D. Specifically, the 1D model overestimates flow deceleration and compressibility, assuming that the entire cross sectional area is filled up by fluid. Furthermore, variations in the NW appear to have little influence on the accuracy of 1D predictions.

Among the models tested, Wang's correlation exhibits the closest agreement with CFD results across all configurations. This again is due to the model being developed specifically for CO2 supercritical flow and being the closest to the CFD extracted value, Figure 3.16.

Interestingly, a result opposite to the conical case can be observed, namely, the higher the Cf value, the higher the Cp predicted by 1D model. This result is counter-intuitive and indeed, is a major limitation of the model, likely stemming from the calculation of  $dP_0$  that assumes proportionality to hydraulic diameter of the section. This simplification was not a problem in conical case where axial flow passing through a cone is more similar to a straight pipe.

Furthermore, the systematic overprediction of  $C_p$  by the 1D model provides a plausible explanation for why the 1D-based separation check anticipates stall earlier than observed in CFD.

Whereas the agreement between 1D and CFD was deemed acceptable in the conical diffuser, in radial geometry it is highly unsatisfactory. For that reason, an effort was made to adapt the 1D model to achieve a better fit. However, the issue was that values for  $dP_0$  could not be derived from CFD due to the local nature of  $P_0$ . Thus, through an iterative process, certain correction factors were applied to find such, that provide best results. As the dual nature of the Cf was appointed to be the source



of the problem, the correction factors were applied as follows:

$$Cf_{\tau} = Cf_{Wang} * 0.6 \tag{3.6}$$

$$Cf_{dP_0} = Cf_{Wang} * 5 (3.7)$$

where  $Cf_{\tau}$  is to be used in tangential momentum equation to evaluate Ct and  $Cf_{dP_0}$  is to be applied to evaluate total pressure drop. The values were determined solely based on the agreement with the results. The influence of the changed Cf values is visible with the MD curve in the Figure 3.18.

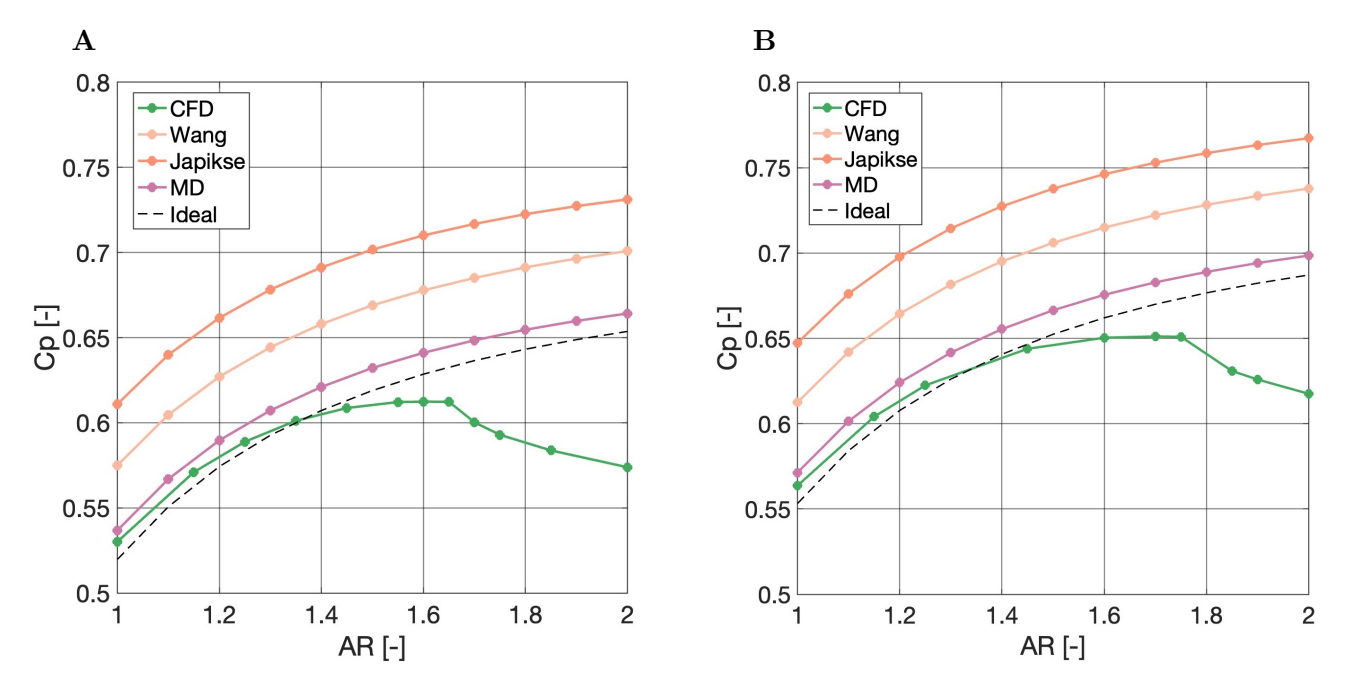


Figure 3.18: Pressure recovery as a function of AR, CFD comparison with 1D model results with a new Cf model. (A) NW = 5.42 (B) NW = 6.25.

What is remarkable is that the ideal value for Cp as evaluated through Equation 1.6 shows outstanding agreement with CFD data. This is naturally a result of the ideal method highly overpredicting the results for incompressible flow due to neglection of friction and as such, does not merit any scientific basis for being a suitable model. Yet, it is a fortunate result that may suggest using the ideal expression for initial calculations in a design process.

M. Dabrowski 41 of 56 June 2025



# 4 Final Thoughts on Modelling Assessment

This section presents a more in-depth and critical evaluation of the results, with particular emphasis on assessing their validity and the implications of the methodological assumptions introduced in section 2. While some points may reiterate earlier discussions, the aim here is to consolidate key insights and provide a comprehensive perspective on the findings.

## 4.1 1D Model Assessment

Several important limitations of the 1D modelling approach must be highlighted to critically assess the accuracy and applicability of the results.

First, in inlet and outlet sections of the conical diffuser, (straight pipe geometry), velocity is expected to increase as the density decreases due to decreasing pressure. However, the iterative solver often accepts errors larger than the actual velocity variation, particularly when operating near the critical point. For instance, operating the same geometry at ambient conditions indeed predicts velocity increase. Reducing the accepted error threshold can improve accuracy but frequently leads to numerical instabilities under SC-CO2 conditions.

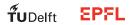
Viscous losses are accounted for solely through the skin friction coefficient,  $C_f$ , and total pressure loss,  $dP_0$ , which are evaluated based on either average or hydraulic diameters of the cross section under consideration. This expression is in nature semi-empirical and thus, an approximation. Also, the model does not account for upstream flow development or geometric discontinuities at the inlet and outlet, where abrupt changes can occur.

By construction, the 1D model assumes a single representative result per section. This simplification ignores the coupled evolution of the boundary layer and core flow. Consequently, pressure recovery is not diminished in the lead-up to separation, which contradicts physical expectations observed in more detailed simulations. Once separation occurs, the model cannot resolve downstream flow fields, as this would require solving the full boundary layer equations which was deemed beyond the scope of the current framework. Thus, the change of gradient of pressure recovery was not captured by 1D modelling.

The solver also neglects the upstream effects stemming from adverse pressure distribution. It was demonstrated in the CFD analysis section that in a conical diffuser, the effect of area change in expansion zone was visible at the end of the inlet. Making the transition between inlet and expansion zone smooth. In 1D solver, this effect is not captured as only one iteration for the diffuser geometry is evaluated.

In radial diffusers, discrepancies are further exacerbated by the dual use of  $C_f$  definitions. While literature-based values of  $C_f$  are derived from correlations involving  $dP_0$ , the 1D model also employs  $C_f$  in the tangential momentum conservation equation (from Stanitz model found in appendix), which relies on wall shear stress,  $\tau_{\text{wall}}$ . This mismatch introduces inconsistencies. As noted in Agormayor et al. (1), applying  $C_f$  from straight-channel studies to radial geometries is generally discouraged. However, the CFD simulations revealed that the  $C_f$  correlation from Wang et al. showed very good agreement with the swirling flow value from the simulations, pointing to the use of the Wang's model in obtaining  $\tau_{\text{wall}}$  to be justified. Thus, it is believed that the semi-empirical  $dP_0$  expression is the source of the discrepancy. To improve accuracy of the estimation of 1D model, the entire procedure presented by Agromayor et al. could be followed.

The Stratford criterion, after calibration of the  $\beta$  parameter, provides reasonably accurate predictions of flow separation in conical diffusers even when using SC-CO2. However, as explained before, due to its simplistic assumptions and max Cp limitations, cannot be applied reliably in wide range of operation. Furthermore, its application to radial diffusers reveals even more discrepancies. The underlying assumption of similarity to flat-plate boundary layers becomes invalid due to the complex



flow behaviour inherent to radial expansion, resulting in poor predictive capability even after tuning through  $\beta$ .

## 4.2 CFD Model Assessment

A number of key modelling assumptions and limitations must be considered to critically evaluate the accuracy and physical fidelity of the CFD simulations presented in this study.

Firstly, the mesh quality and near-wall resolution were assessed using the dimensionless wall distance,  $y^+$ . The simulations maintained  $y^+$  values within an acceptable range for most of the domain, ensuring the validity of wall-function-based turbulence modelling. However, locally, especially at the inlet in radial diffuser simulations, the maximum  $y^+$  often reached values of above 80. Even though a local occurrence, this may have affected flow field further downstream, influencing final pressure and velocity distribution.

The CFD simulations employed a barotropic gas model, which assumes a fixed functional relationship between pressure and density. As a result, the same  $p - \rho$  relation governs flow behaviour at the inlet, outlet, and within the expansion region. This approximates the friction loss process in straight pipe geometry.

Barotropic model simplification allows for higher computational efficiency, however, it omits thermal effects, as the energy equation is not solved. Consequently, any flow features driven by heat transfer or temperature gradients are not captured. As the flow simulated in a diffuser is not at high velocity, aerodynamic heating is deemed negligible. However, CFD cannot validate that without solving energy equation. Thus, model's applicability may be questioned in other flow simulations involving significant work or heat transfer.

Furthermore, turbulence modelling was performed using an eddy viscosity approach through use of k-omega SST model. As a result, the turbulence effects captured in simulations are analogous to those in air, although the final values in SC-CO2 simulations were higher than in corresponding air simulations. A dense fluid such as SC-CO2, has drastically different molecular structure to air, which could point to its microscale mixing being different as well. Thus, extracting Cf from RANS simulation with eddy viscosity model cannot be treated as a final validation even if energy equation was incorporated.

Lastly, transient flow phenomena, particularly in the context of separation, merit attention. Effects such as rotating stall or asymmetric flow attachment were observed in CFD but cannot be adequately resolved in steady-state simulations that were key in this study. Capturing accurately these dynamics would require unsteady (transient) simulations to properly characterize the evolution and impact of such instabilities. Only then, final answer could be provided to what happens to pressure recovery of SC-CO2 flow after separation.

Overall, while the CFD methodology offers valuable insight into flow behaviour, it is constrained by modelling assumptions that should be addressed through advanced turbulence models and transient analyses for comprehensive validation. This study would therefore benefit from a few transient LES simulations with very fine meshes.



# 5 Conclusions and Suggestions

Throughout this study, the development, performance and limitations of 1D and CFD modelling methods were presented with the goal of assessing their applicability in the design process of SC-CO2 operating diffusers. This section will highlight the key findings and conclusions. Finally, it will also provide a few recommendations for future research and further validation ideas.

It was confirmed with CFD simulations that use of SC-CO2 in vaneless radial and conical diffuser promotes higher pressure recovery compared to air. This effect was attributed to large density and higher expansion of SC-CO2 fluid. Furthermore, in the conical diffuser it was found that the flow separation is delayed, reaching maximum pressure recovery for slightly higher AR. It was motivated by the fact that the turbulence and viscosity in SC-CO2 is higher, making the boundary layer profile more resistant to separation, allowing for higher maximum adverse pressure gradient. Those findings point to the guidelines changes that can be done for conical diffusers, as indicated by the expression for critical geometry. For radial diffuser, the difference in stall in air and SC-CO2 was not visible, and the critical geometry was suggested to be kept unaltered.

Furthermore, using CFD results, the value for Cf was obtained for axial and radial flows. It emerged that the closest model from literature was the one proposed by Wang et al.(27). This was the case for both flow types that showed very similar Cf values, contrary to the initial scepticism that swirling flow would have very different (higher) value.

Regarding 1D modelling, the conical prediction using Wang et al. model was deemed satisfactory for geometries far from stall. This being attributable to similarity of axial flow within pipe and conical diffuser. The friction influence is comparable and until the boundary layer growth is not significant, the prediction of 1D model provides meaningful results. This is despite it not accounting for boundary layer interaction and upstream effects.

In the case of radial diffuser, the agreement between 1D and CFD model was initially weak. The reason for that was identified to be the use of friction coefficient to obtain total pressure drop via pipe relation with hydraulic diameter. To improve the prediction, correction factors were successfully applied that changed the friction coefficient magnitude depending on its use. Moreover, it was discovered that the incompressible, inviscid relation for pressure coefficient provided remarkably close results to CFD. This was explained to be a coincidental outcome, resulting from the ideal expression significantly overpredicting the air simulation results.

The effort of implementing a separation criterion in 1D modelling was deemed unsuccessful due to Stratford condition oversimplifying the boundary layer profile and its limited applicability to relatively low pressure coefficient values.

Finally, a few recommendations for further research can be made. It would be insightful to redo the radial diffuser simulations with a 1D model based on full Stanitz equations (25) transformed for non-ideal gas(1). This routine could be followed with the friction model of Wang et al. as it proved to be close to the friction values extracted from CFD.

Regarding CFD simulations, to gain better insight into turbulence dynamics specific to SC-CO2 a Reynolds stress model or an LES study should be conducted. Also, to better understand the pressure recovery after separation, transient simulations should be performed.

A deeper study into Mach number influence should also be performed. In this research only one value was tested per diffuser, however, it is expected that as compressibility effects become more significant at higher Mach numbers, the SC-CO2 will promote even higher pressure recovery compared to air

Lastly, the study would benefit from more simulations assessing  $\alpha_{in}$  influence on stall. Based on the simulations performed, it was assumed that for  $\alpha_{in} = 65[\deg]$  the critical geometry for SC-CO2 and air radial diffusers does not vary significantly. Moreover, it was assumed that the geometry varies quadratically. However, a deeper study into stall phenomena in radial flow would be beneficial.



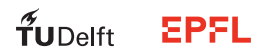
## REFERENCES

1. R. Agromayor, B. Müller, L. O. Nord, One-Dimensional Annular Diffuser Model for Preliminary Turbomachinery Design. *International Journal of Turbomachinery, Propulsion and Power* 4, 31, ISSN: 2504-186X, (2025; https://www.mdpi.com/2504-186X/4/3/31) (Sept. 17, 2019).

- 2. J. D. Anderson, J. D. Anderson, Fundamentals of aerodynamics, OCLC: ocn463634144 (McGraw-Hill, New York, 5th ed, 2011), 1106 pp., ISBN: 9780073398105.
- 3. Ansys CFX Academic Research, Release 2024 and 2025, ANSYS, Inc. (Canonsburg, PA, USA).
- 4. ANSYS, Inc., Release 2021 R2, Ansys CFX-Pre User's Guide.
- 5. ANSYS, Inc., Release 2021 R2, Ansys CFX-Solver Theory Guide.
- 6. N. D. Baltadjiev, "An Investigation of Real Gas Effects in Supercritical CO2 Compressors" (Massachusetts Institute of Technology, Sept. 2012).
- 7. W. B. Brown, G. R. Bradshaw, "Methods of Designing Vaneless Diffusers and Experimental Investigation of Certain Undetermined Parameters", tech. rep. (Flight Propulsion Research Laboratory, Cleveland, Ohio, Sept. 1947).
- 8. C. F. Colebrook, C. M. White, Experiments with fluid friction in roughened pipes. *Proceedings of the Royal Society of London. Series A-Mathematical and Physical Sciences* **161**, 367–381 (1937).
- X. Fang, L. Xu, Y. Chen, W. Chen, Correlations for friction factor of turbulent pipe flow under supercritical pressure: Review and a new correlation. Progress in Nuclear Energy 118, 103085, ISSN: 01491970, (2024; https://linkinghub.elsevier.com/retrieve/pii/S0149197019301866) (Jan. 2020).
- 10. X. Fang, Y. Xu, X. Su, R. Shi, Pressure drop and friction factor correlations of supercritical flow. Nuclear Engineering and Design 242, 323-330, ISSN: 00295493, (2024; https://linkinghub.elsevier.com/retrieve/pii/S0029549311009149) (Jan. 2012).
- 11. E. Feher, The supercritical thermodynamic power cycle. Energy Conversion 8, 85–90, ISSN: 0013-7480, (https://www.sciencedirect.com/science/article/pii/0013748068901058) (1968).
- 12. B. Grossman, "Fundamental Concepts of Real Gasdynamics" (Virginia Polytechnic Institute and State University, Jan. 2000).
- 13. A. Guardone, P. Colonna, M. Pini, A. Spinelli, Nonideal Compressible Fluid Dynamics of Dense Vapors and Supercritical Fluids. Annual Review of Fluid Mechanics 56, 241-269, ISSN: 0066-4189, 1545-4479, (2025; https://www.annualreviews.org/doi/10.1146/annurev-fluid-120720-033342) (Jan. 19, 2024).
- 14. A. Kumar et al., Numerical Analysis of a Two-Phase Turbine: A Comparative Study Between Barotropic and Mixture Models. Journal of Engineering for Gas Turbines and Power 147, 051013, ISSN: 0742-4795, eprint: https://asmedigitalcollection.asme.org/gasturbinespower/article-pdf/147/5/051013/7404475/gtp\\_147\\_05\\_051013.pdf, (https://doi.org/10.1115/1.4066819) (Nov. 2024).
- J. Lee, J. I. Lee, H. J. Yoon, J. E. Cha, Supercritical Carbon Dioxide turbomachinery design for water-cooled Small Modular Reactor application. *Nuclear Engineering and Design* 270, 76-89, ISSN: 0029-5493, (https://www.sciencedirect.com/science/article/pii/S0029549313007371) (2014).
- 16. E. W. Lemmon, I. Bell, M. L. Huber, M. O. McLinden, NIST Standard Reference Database 23: Reference Fluid Thermodynamic and Transport Properties-REFPROP, Version 10.0, National Institute of Standards and Technology, 2018, (https://www.nist.gov/srd/refprop).



- 17. D. Mimic, C. Jätz, F. Herbst, Correlation between total pressure losses of highly loaded annular diffusers and integral stage design parameters. *Journal of the Global Power and Propulsion Society* 2, I9AB30, ISSN: 2515-3080, (2024; https://journal.gpps.global/a/I9AB30/) (Aug. 27, 2018).
- 18. L. F. Moody, Friction Factors for Pipe Flow. *Journal of Fluids Engineering* **66**, 671–678, ISSN: 0097-6822, (2025; https://asmedigitalcollection.asme.org/fluidsengineering/article/66/8/671/1153865/Friction-Factors-for-Pipe-Flow) (Nov. 1, 1944).
- 19. Nieuwstadt, Boersma, Westerweel, *Turbulence* (Springer Berlin Heidelberg, New York, NY, 2016), ISBN: 9783319315973.
- 20. L. R. Reneau, J. P. Johnston, S. J. Kline, Performance and Design of Straight, Two-Dimensional Diffusers. Journal of Basic Engineering 89, 141-150, ISSN: 0021-9223, (2024; https://asmedigitalcollectiasme.org/fluidsengineering/article/89/1/141/397580/Performance-and-Design-of-Straight-TwoDimensional) (Mar. 1, 1967).
- 21. J. Schiffmann, PhD thesis, Lausanne, EPFL, 2008, (2025; https://infoscience.epfl.ch/handle/20.500.14299/25781).
- 22. Schlichting, Gersten, Boundary-layer theory (Springer Berlin Heidelberg, New York, NY, 2016), ISBN: 9783662529171.
- 23. L. Seshadri, P. Kumar, Vaneless Diffuser Modeling for Real Gas Supercritical Carbon Dioxide Flows: Need for a Data-Driven Approach. Journal of Engineering for Gas Turbines and Power 147, 041027, ISSN: 0742-4795, eprint: https://asmedigitalcollection.asme.org/gasturbinespower/article-pdf/147/4/041027/7411892/gtp\\_147\\_04\\_041027.pdf, (https://doi.org/10.1115/1.4066709) (Nov. 2024).
- 24. R. Span, W. Wagner, A New Equation of State for Carbon Dioxide Covering the Fluid Region from the Triple-Point Temperature to 1100 K at Pressures up to 800 MPa. *Journal of Physical and Chemical Reference Data* (1996).
- 25. J. D. Stanitz, "One-dimensional compressible flow in vaneless diffusers of radial and mixed-flow centrifugal compressors. including effects of friction, heat transfer and area change" (National Advisory Committee for Aeronautics, Lewis Flight Propulsion Laboratory Cleveland, Ohio, Jan. 1952).
- 26. B. Stratford, "The Prediction of Separation of the Turbulent Boundary Layer" (National Gas Turbine Establishment, Farnborough, 1958).
- 27. Z. Wang, B. Sun, J. Wang, L. Hou, Experimental study on the friction coefficient of supercritical carbon dioxide in pipes. *International Journal of Greenhouse Gas Control* **25**, 151–161, ISSN: 17505836, (2024; https://linkinghub.elsevier.com/retrieve/pii/S1750583614000978) (June 2014).
- 28. A. Whitfield, N. C. Baines, *Design of radial turbomachines* (Longman J. Wiley and sons, Harlow New York, 1990), ISBN: 9780582495012 9780470216675.
- 29. L. Zhang et al., Stall Evolution Mechanism of a Centrifugal Compressor with a Wide-Long Vaneless Diffuser. Journal of Thermal Science 33, 899-913, ISSN: 1003-2169, 1993-033X, (2025; https://link.springer.com/10.1007/s11630-024-1951-y) (May 2024).



# A Ideal Pressure Recovery

Ideal pressure recovery is often used to give initial estimate of performance of a diffuser. It assumes that the flow has not losses such as fiction and it incompressible.

The ideal pressure recovery in conical diffuser is a derivative of two equations, conservation of mass and Bernoulli, summarised as follows:

$$\rho V_1 A_1 = \rho V_2 A_2 \tag{A.1}$$

$$p_1 + \frac{1}{2}\rho V_1^2 = p_2 + \frac{1}{2}\rho V_2^2 \tag{A.2}$$

assuming incompressible flow, from the continuity equation velocity can be evaluated and substituted into Bernoulli to fully express pressure. By considering two stations 1 and 2, the pressure at the latter follows:

$$p_2 = p_1 + \frac{1}{2}\rho V_1^2 - \frac{1}{2}\rho (V_1 \frac{A_1}{A_2})^2 \tag{A.3}$$

by further recalling the definition of pressure coefficient:

$$Cp = \frac{p - p_{\infty}}{\frac{1}{2}\rho V^2} \tag{A.4}$$

pressure recovery in conical diffuser can be summarized as a function of area ratio (AR):

$$Cp = 1 - \frac{1}{AR^2}.$$
 (A.5)

In the radial diffuser, the following relations are used to derive ideal recovery:

$$\rho C_1 \cos \alpha_1 A_1 = \rho C_2 \cos \alpha_2 A_2 \tag{A.6}$$

$$p_1 + \frac{1}{2}\rho C_1^2 = p_2 + \frac{1}{2}\rho C_2^2 \tag{A.7}$$

$$R_1 C_1 \sin \alpha_1 = R_2 C_2 \sin \alpha_2 \tag{A.8}$$

which are continuity in radial flow, Bernoulli and conservation of angular momentum in absence of friction. The velocity at station 2 can be derived by solving the system of the first and the last equations after some trigonometric manipulations it is given as:

$$C_2 = C_1 \cos \alpha_1 \frac{1}{AR} \sqrt{\left(\tan \alpha_1 \left(\frac{b_2}{b_1}\right)\right)^2 + 1} \tag{A.9}$$

where b stands for diffuser width. After substituting it into the Bernoulli equation and Cp definition, some mathematical manipulations yield:

$$Cp = cos^{2}(\alpha_{1})(1 - \frac{1}{AR^{2}}) + sin^{2}(\alpha_{1})(1 - \frac{1}{RR^{2}})$$
 (A.10)

where RR stands for radii ratio.



# B Cross-sectional area in diffusers

In a conical diffuser where the profile is assumed to have straight walls, the radius varies linearly with length:

$$R(x) = \frac{R_2 - R_1}{L} x + R_1 \tag{B.1}$$

and the area follows:

$$A(x) = \pi R^2(x) \tag{B.2}$$

thus in a straight conical profile, the AR is not varying linearly with length.

In radial diffuser with straight walls, width scales with:

$$b(r) = \frac{b_2 - b_1}{R_2 - R_1}r + b_2 - \frac{b_2 - b_1}{R_2 - R_1}R_2$$
(B.3)

and the area follows:

$$A(r) = 2\pi r b(r) \tag{B.4}$$

thus in radial diffuser, the straight wall profile results in quadratic cross sectional area evolution as a function of characteristic length.

# C Stanitz Radial Diffuser Flow Model

Stanitz states that "Even with relatively low friction coefficients and neglecting mixing losses near the impeller tip, the friction losses in most vaneless diffuser designs are considerable [...] and these losses result from the usually large ratios of wetted surface to flow area in vaneless diffusers." Stanitz proposed a model that includes the effects of friction (25). It is summarised by the following equations: Radial momentum conservation:

$$\frac{1}{\rho}\frac{dP}{dr} + C_m \frac{dC_m}{dr} - \frac{C_\theta^2}{r} + C_f \frac{C^2 \cos \alpha}{b} = 0 \tag{C.1}$$

Tangential momentum conservation:

$$C_m \frac{dC_\theta}{dr} + \frac{C_m C_\theta}{r} + C_f \frac{C^2 \sin \alpha}{b} = 0 \tag{C.2}$$

Continuity conservation:

$$\frac{1}{\rho} \frac{d\rho}{dr} + \frac{1}{C_m} \frac{dC_m}{dr} + \frac{1}{b} \frac{db}{dr} + \frac{1}{r} = 0$$
 (C.3)

Energy equation:

$$T_0 = T + \frac{\gamma - 1}{2\gamma R} C^2 \tag{C.4}$$

Ideal EOS:

$$P = \rho RT \tag{C.5}$$



## D USE OF NON-IDEAL GAS MODEL

Firstly, the flow of the gas itself is addressed in a straight pipe. Assuming that the flow is inviscid, adiabatic and without body forces the energy and momentum conservation equations dictate:

$$dh + udu = 0 (D.1)$$

$$dp + \rho u du = 0. (D.2)$$

It is important to realise here that they do not differ to the relations in ideal flow as they stem from conservation of fundamental concepts. Thus, when applied in the Gibbs equation an interesting result is observed:

$$ds = 0 (D.3)$$

which says that in such a flow, the non-ideal effects themselves do not produce any losses, a result that was not visible from the Equation E.16. It follows then that the same as for the ideal gas flow, the total properties (enthalpy and pressure) are conserved along a streamline in absence of viscosity (friction), body forces and heat/work exchange. Naturally, the same conclusion can be made by just investigating the energy and momentum equations.

In general, total enthalpy of the fluid is constant even with addition of friction and viscosity as the loss of momentum of fluid (which is postulated by the total pressure drop) is manifested in the increase in average kinetic speed of agitated molecules, that is temperature. Thus, the same statement as for the ideal flow can be made, that total enthalpy can be only changed by the means of energy transfer - heat or work.

In order to evaluate properties in an adiabatic (also with no work) real gas flow, the iterative scheme suggested by Grossman can be applied (12). To use that method, a library of thermophysical properties is necessary. Ideally, for  $CO_2$  one derived from SW model should be used. Database contained in REFPROP developed by NIST or an open source CoolProp library are two known sources. Such a library will be able to derive all properties of a point in gas based on two others.

Firstly, given the  $p, T, \rho$  at the inlet of the flow, the entropy is evaluated through a real gas library, here referred to as RealGasLib:

$$s = RealGasLib(p, T) \tag{D.4}$$

which is a crucial result as according to the definition of total properties it is the same for static and total properties of a given point (total/stagnation property is defined as property which is slowed done isentropically). Having obtained that, the total enthalpy is now derived:

$$h_{tot} = h_{stat} + \frac{u^2}{2} \tag{D.5}$$

that is constant along the streamline. Now, to obtain the conditions at the outlet, the continuity equation can be introduced to obtain  $u_{out}$  in order to evaluate  $h_{stat}$ . That, together with s from the Equation D.4 will be sufficient to evaluate all the static properties at the outlet through:

$$p, h, T, \rho = RealGasLib(h_{stat}, s). \tag{D.6}$$

However, there is a major problem with that procedure as the continuity equation relates not the  $u_{in}$  to  $u_{out}$  only but  $\rho_{in}u_{in}$  to  $\rho_{out}u_{out}$  (assuming known geometry). As the EOS in a linear form is not available an analytical solution cannot be,  $\rho$  can be only derived from RealGasLib. Instead an iterative searching scheme must be applied that based on a guess of  $u_{out}$  will evaluate  $\rho_{out}$  through RealGasLib and then check if the continuity equation is satisfied (up to a certain desired error). Thus, it is necessary to use iterations to find a solution, which noticeably increases computational time. The effect of friction on losses can be added by relating friction effects to total pressure drop.

# E IDEALISED REAL GAS

As explained before, the supercritical gas has significantly different compressibility compared to the ideal case. In an attempt to capture the deviation a variable Z called compressibility factor can be introduced. It is defined as:

$$Z = \frac{v}{v_{ideal}} \tag{E.1}$$

thus it compares the ideal specific volume predicted by the ideal EOS to the real one. Based on that definition, the EOS can be amended to:

$$pv = ZRT.$$
 (E.2)

Naturally, use of this expression instead of ideal EOS will not produce results that fully capture the complexity of the real gas as Z is not constant across different thermoproperties. Yet, it will significantly improve the simplistic, ideal EOS.

Having defined Z, its use can be employed in further derivation of non-ideal gas flow relations. Firstly, the compressibility  $\beta$  is derived for two cases:

$$\beta_T = -\frac{1}{v} \left( \frac{\partial v}{\partial p} \right)_T = \frac{1}{p} - \frac{1}{Z} \left( \frac{\partial Z}{\partial p} \right)_T, \tag{E.3}$$

$$\beta_p = \frac{1}{v} \left( \frac{\partial v}{\partial T} \right)_p = \frac{1}{T} + \frac{1}{Z} \left( \frac{\partial Z}{\partial T} \right)_p. \tag{E.4}$$

With those relations, Maxwell relations can be evaluated to lead to the caloric equations in terms of enthalpy and internal energy as:

$$dh = c_p dT + \left[v(1 - T\beta_p)\right] dp \tag{E.5}$$

$$du = cvdT + \left[ p \left( \frac{\beta_p T}{\beta_T p} - 1 \right) \right] dv.$$
 (E.6)

Subsequently, to be able to evaluate total properties, isentropic exponents are introduces. It is assumed that relations of form:

$$pv^{n_s} = const. (E.7)$$

$$Tp^{-m_s} = const. (E.8)$$

exist, so that the isentropic (and adiabatic) derivation give:

$$n_s = \frac{\gamma}{\beta_T p} \tag{E.9}$$

$$m_s = \frac{\gamma - 1}{\gamma} \frac{\beta_T p}{\beta_p T}.$$
 (E.10)

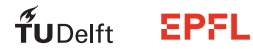
With those exponent the isentropic relations between total and static conditions can be derived to give:

$$\frac{p_{tot}}{p} = \left(\frac{M^2(n_s - 1)}{2} + 1\right)^{\frac{n_s}{n_s - 1}} \tag{E.11}$$

and

$$\frac{T_{tot}}{T} = \left(\frac{p_{tot}}{p}\right)^{m_s} = \left(\frac{v_{tot}}{v}\right)^{-n_s m_s}.$$
 (E.12)

It is crucial to remark that to obtain the expressions above, it was assumed that the isentropic exponents are constant between total and static conditions:  $p_{tot}v_{tot}^{n_s} = pv^{n_s}$ . This is not strictly the case for supercritical flow in which compressibility changes depending on conditions. However, to



obtain an analytical model, this assumption is necessary. Furthermore, the speed of sound can be expressed as:

$$a = \sqrt{n_s pv} = \sqrt{n_s ZRT}. (E.13)$$

Based on the Equation E.11, Equation E.12 and Equation E.13 properties of inviscid, adiabatic with no body forces flow type can be evaluated. By assuming total properties are constant across channel, a system of equations with continuity equation to get Mach number and an isentropic relation can be solved. Thus, an analytical model can be used that is solved in the same manner as the one for ideal gas flow.

Furthermore, losses in form of entropy, for a real gas flow can be addressed. Starting from the Gibbs as in the Equation E.14:

$$dh = Tds + vdp (E.14)$$

and substituting enthalpy as found through the Maxwell relations in the Equation E.5 the following relation is obtained:

$$c_p dT + [v(1 - T\beta_p)]dp = Tds + vdp$$
(E.15)

and can be rearranged to:

$$ds = \frac{c_p}{T}dT - v\beta_p dp \tag{E.16}$$

which is an analytical formula for expressing losses. However, in reality it does not have a direct application as evaluating an integral of  $v\beta_p$  would be a major challenge.

Lastly, in order to visualise further the non-ideality of the real gas, one can look at the fundamental (also called Landau) derivative  $\Gamma$ . It is defined as:

$$\Gamma = \frac{c^4}{2v^3} \left( \frac{\partial^2 v}{\partial p^2} \right)_s \tag{E.17}$$

and for ideal gas it simplifies to  $\Gamma = \frac{1}{2}(\gamma + 1)$  as  $pv^{\gamma} = const$  which gives a value  $\Gamma > 1$ . The value of the derivative shows the curvature of the isentropes in p - v space. For real gases however, the value of  $\Gamma$  drops below 1. This effect is represented in for instance behaviour of M due to v. In ideal gas, for expanding channel with M > 1 the M will increase monotonously. However, for real gases, is is not the case.

# F STRATFORD CRITERION

Using the theory outlined above it is still a major challenge to determine the risk of separation in a flow at adverse pressure gradient. It often involves solving a system differential equations without simple solutions for more complex flows. To simplify that procedure an alternative solution was proposed by Stratford.

This condition is said to be a rapid method for prediction of flow separation in turbulent boundary layer that, as in case of boundary layer theory by Prandtl, is a result of approximate solution of equations of motion. Stratford's method only requires a single empirical factor. Stratford starts by distinguishing two layer in the turbulent boundary layer, outer and inner. It is important to remark that the notation used by Stratford omits the bar above variables to express their average, as commonly used when describing turbulent flows. Despite that, it is still believed that the relations suggested below are meant for the averaged values.

## Outer region

Firstly, for the outer layer, it was determined that the increase of pressure downstream has effect of lowering the dynamic head  $\frac{1}{2}\rho u^2$  however, the shape of the boundary layer in the outer region is unaffected. This is said to be a consequence of low shear forces compared to the stronger inertia forces



(or pressure gradient) for a rapid pressure rise. The solution for the outer boundary layer velocity profile is obtained by comparison of a case with and without pressure gradient. The flow properties for constant pressure flow will be denoted with a dash e.g. P'. The two considered flows have the same static and total pressures at  $x_0$ . Also, the distribution of  $\frac{\partial \tau}{\partial y}$  at  $x_0$  will be identical far from wall and it is assumed that it is the same for two cases also downstream (not too far from  $x_0$ ). Starting with the Bernoulli equation for total pressure including shear forces:

$$\frac{\partial P}{\partial s} = \frac{\partial \tau}{\partial y} \tag{F.1}$$

where P denotes total pressure and s is the path along the streamline. It is paramount not to mistake it for entropy despite the same symbol being used in the rest of this review. The Equation F.1 can be integrated to:

$$P(x,\psi) = P(x_0,\psi) + \int_{x_0}^{x} \frac{\partial \tau}{\partial y} ds$$
 (F.2)

where  $\psi$  is used as a parameter to distinguish the outer layer:

$$\psi = \int_0^y u dy. \tag{F.3}$$

Due to the assumption that the  $\frac{\partial \tau}{\partial y}$  profile is the same for constant and adverse pressure flows, the total pressures will be equal at x downstream of  $x_0$  for  $\psi_i \leq \psi$ :

$$P(x,\psi) = P'(x,\psi) \tag{F.4}$$

rewriting it by expanding total pressure into static and dynamic (head):

$$p + \frac{1}{2}\rho u^2(x,\psi) = p' + \frac{1}{2}\rho u'^2(x,\psi)$$
 (F.5)

also, for the flow with constant static pressure  $p' = p_0$  and  $p_0$  is identical for two cases:

$$\frac{1}{2}\rho u^2(x,\psi) = \frac{1}{2}\rho u'^2(x,\psi) - (p-p_0)$$
 (F.6)

Thus, the dynamic pressure (head) can be evaluated at a given point by subtracting pressure rise from dynamic pressure in constant pressure flow. This includes the viscosity as its effect is hidden in the head loss  $\frac{1}{2}\rho u'^2(x,\psi)$ . For the outer boundary layer profile it carries an important consequence as by differentiation of the Equation F.6 the following result is found:

$$\left[\frac{\partial u}{\partial y}\right]_{(x,\psi)} = \left[\frac{\partial u'}{\partial y'}\right]_{(x,\psi)} \tag{F.7}$$

meaning that the boundary layer velocity profile for a case where adverse pressure gradient exists is the same as fro the case of constant static pressure for the outer layer of the boundary layer. This is effect of the assumption that  $\frac{\partial \tau}{\partial y}$  is the same for two cases. Having proved that the shape of the outer boundary layer region is unaffected by rapid pressure rise, the standard solution for boundary layer without pressure rise can be used. Stratford proposes the following semi-empirical model:

$$\frac{u'}{U_0} = \left(\frac{y'}{\delta'}\right)^{(1/n)} \tag{F.8}$$

$$\delta' = \frac{(n+1)(n+2)}{n}\theta' \tag{F.9}$$

$$\theta' = 0.036xRe^{-\frac{1}{5}} \tag{F.10}$$

which assumes the power law for the velocity profile. Its accuracy was questioned before by the Nieuwstadt et al. (19), thus, the solution for the outer region can be improved. Also, the common value taken for n is 7, however, in reality it varies moderately with Re.

### Inner region

Contrary to the outer layer, in the inner layer the fluid inertia is too small to balance the back pressure. The flow has significantly lower velocity close to the wall with u=0 at the wall. Thus, the pressure force is assumed to be balanced purely by the gradient of the shear force. At the wall, the momentum conservation dictates:

 $\frac{\partial p}{\partial x} = \frac{\partial \tau}{\partial y}$  at y = 0. (F.11)

The no-slip condition is the very reason why at the inner layer the sudden pressure rise causes not only the lowering of the dynamic head but also changes the shape of the profile due to its "anchored" outset u = 0 at y = 0.

Further analysis makes use of the mixing length theory to portray a profile of the inner layer. For very small distance y from the wall with positive  $\partial u/\partial y$  (thus still not separated flow) shear stress is given by:

$$\tau = \rho K^2 y^2 \left(\frac{\partial u}{\partial y}\right)^2 \tag{F.12}$$

as given by Durand in 1943. The constant K denoted the Karman constant. Now, the assumption of flow just beginning to separate is made so that  $\partial u/\partial y = 0$  and  $\tau_s = 0$ . With that the Equation F.11 can be integrated to:

$$\tau = y \frac{\partial p}{\partial x} \tag{F.13}$$

by assuming that pressure gradient is constant along y. By combining and integrating the two expressions for shear stress, the following expression for velocity profile at the inner layer is found:

$$u = \left(\frac{4}{\rho K^2} \frac{\partial p}{\partial x}\right)^{\frac{1}{2}} y^{\frac{1}{2}}.$$
 (F.14)

This expression shows the velocity profile of the inner layer when the flow starts to separate. However, this is an idealised result as pressure gradient effect on the mixing length is not included. Thus, to account for it, Stratford, suggests introducing an experimental factor  $\beta$  to obtain:

$$u = \left(\frac{4}{\rho(\beta K)^2} \frac{\partial p}{\partial x}\right)^{\frac{1}{2}} y^{\frac{1}{2}}.$$
 (F.15)

The factor  $\beta$  is the single empirical factor that has to be introduced from pertinent experiments.

### Merging point

The outer layer can be explicitly determined based on the pressure gradient and boundary layer theory for a flat plate. The inner profile, however, was derived for a flow that is starting to separate. Thus, it can be said that when two profiles agree at the intersection, the flow experiences separation. At the joining point  $\psi_i$  the flows are compared by equating their  $\psi(\partial u/\partial y)^3$  and  $u^2/(\psi\partial u/\partial y)$ . Also, as explained before, for the shape of the outer layer, the relation for a flat plate is used at the same position. Based on the above, the separation condition is given as:

$$(2Cp)^{\frac{n-2}{4}} \left( x \frac{dCp}{dx} \right)^{\frac{1}{2}} = 1.06\beta (10^{-6}Re)^{\frac{1}{10}} \quad \text{for } \left( Cp \le \frac{n-2}{n+1} \right)$$
 (F.16)

where the Karman constant K = 0.41 and an approximation was made for a polynomial of n. They Reynolds number Re is calculated for the local value of x and peak velocity  $U_0$  (appears from Equation F.10 so the same values should be used as in that model). The pressure coefficient Cp is defined

as:

$$Cp = \frac{p - p_0}{\frac{1}{2}\rho U_0^2} \tag{F.17}$$

where following the convention from the Equation F.6 p is the static pressure due to the pressure gradient and  $p_0$  is the static pressure at the outset. The condition given for Cp is the limiting case for which the merging point of inner and outer layers would occur at the boundary layer edge. Regarding the value of  $\beta$ , Stratford conducted extensive experiments and found that it is independent of Cp; however, there exists influence of its second derivative  $d^2p/dx^2$ :

$$\beta = 0.66 \quad \text{for } \frac{d^2p}{dx^2} < 0,$$

$$\beta = 0.73 \quad \text{for } \frac{d^2p}{dx^2} \ge 0.$$
(F.18)

Lastly, the value taken for n stems from the comparison with flat plate case as it is used to approximate the velocity profile of the outer layer. Stratford suggests to use values between 6-7 and claimed that the Equation F.16 is not sensitive to n. However, for more educated choice of the value the it was advised to follow:

$$n = log_{10}Re_s \tag{F.19}$$

where  $Re_s$  is the Reynolds number on a flat plate at separation point  $x_s$ :

$$Re_s = \frac{x_s U_0}{\nu} \tag{F.20}$$

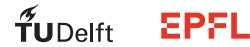
Thus, Stratford has preposed a convenient method for evaluating the risk of flow separation with the Equation F.16. The method is said to be more conservative as predicting too low pressure gradients necessary for flow separation. However, it is stated that the results are at most 10% too low, which is deemed acceptable.

# G CFD

## G.1 Conical diffuser

Barotropic model based on 1D solution of a diffuser with AR = 3.03 and NW = 3. With inlet properties of M = 0.29, P = 80[bar] and T = 310[K] derived with Fang 2011 Cf model.

```
if(AbsolutePressure >= 8.436500E + 06[Pa], \\ 1.2955467673048429e + 02 + 2.4751250978659324e - 05 * AbsolutePressure/1[Pa], \\ if(AbsolutePressure >= 7.943296E + 06[Pa], \\ -1.0778470282123003e + 02 * (AbsolutePressure/7.943296E + 06[Pa])^2 + \\ 4.2554739711782531e + 02 * (AbsolutePressure/7.943296E + 06[Pa])^1 + \\ 7.9837911343779506e + 00 * (AbsolutePressure/7.943296E + 06[Pa])^0, \\ 3.2574648543097322e + 02 * exp((AbsolutePressure/7.9432961048442917e + 06[Pa] - 1.0)/ \\ (1.5530793999479489e + 00)))) * 1[kg/m^3]
```



## ANSYS CFX VISCOSITY EXPRESSION

```
\begin{split} &if(Absolute Pressure>=8.4364999630011152e+06[Pa],\\ &1.0687230265575134e-05+1.6655069773502198e-12*Absolute Pressure/1[Pa],\\ &if(Absolute Pressure>=7.9432961048442917e+06[Pa],\\ &-3.8351689368471245e-06*(Absolute Pressure/7.9432961048442917e+06[Pa])^2+2.1375733548013965e-05*(Absolute Pressure/7.9432961048442917e+06[Pa])^1+6.3615247446601546e-06*(Absolute Pressure/7.9432961048442917e+06[Pa])^0,\\ &2.3902089355826994e-05*exp((Absolute Pressure/7.9432961048442917e+06[Pa]-1.0)/(1.7450588761362522e+00))))*1[Pa*s] \end{split}
```

# G.2 RADIAL DIFFUSER

Barotropic model based on 1D model solution of a diffuser with AR = 1.65 and NW = 5.42. With inlet properties of  $\alpha_{in} = 73.79^{\circ}$  C = 175.52, P = 133.58[bar] and T = 364.76[K] derived with Fang 2019 Cf model.

## ANSYS CFX DENSITY EXPRESSION

```
\begin{split} &if(AbsolutePressure>=1.704426E+07[Pa],\\ &1.5686260109187032E+02+1.1533292713961627E-05*AbsolutePressure/1[Pa],\\ &if(AbsolutePressure>=1.335823E+07[Pa],\\ &-6.1011234753138332E+01*(AbsolutePressure/1.335823E+07[Pa])^2+\\ &3.0931203744973470E+02*(AbsolutePressure/1.335823E+07[Pa])^1+\\ &5.8103518188663834E+01*(AbsolutePressure/1.335823E+07[Pa])^0,\\ &3.0640432088526023E+02*exp((AbsolutePressure/1.3358225381853979E+07[Pa]-1.0)/\\ &1.6568387176101111E+00)))*1[kg/m^3] \end{split}
```

## ANSYS CFX VISCOSITY EXPRESSION

```
\begin{split} &if(AbsolutePressure>=1.7044262304828115E+07[Pa],\\ &1.4788488361044561E-05+8.4342987536865194E-13*AbsolutePressure/1[Pa],\\ &if(AbsolutePressure>=1.3358225381853979E+07[Pa],\\ &-2.5078729096669038E-06*(AbsolutePressure/1.3358225381853979E+07[Pa])^2+1.7648199187172545E-05*(AbsolutePressure/1.3358225381853979E+07[Pa])^1+1.0728986375899744E-05*(AbsolutePressure/1.3358225381853979E+07[Pa])^0,\\ &2.5869312653405386E-05*exp((AbsolutePressure/1.3358225381853979E+07[Pa]-1.0)/\\ &2.0636692451961496E+00)))*1[Pa\cdot s] \end{split}
```

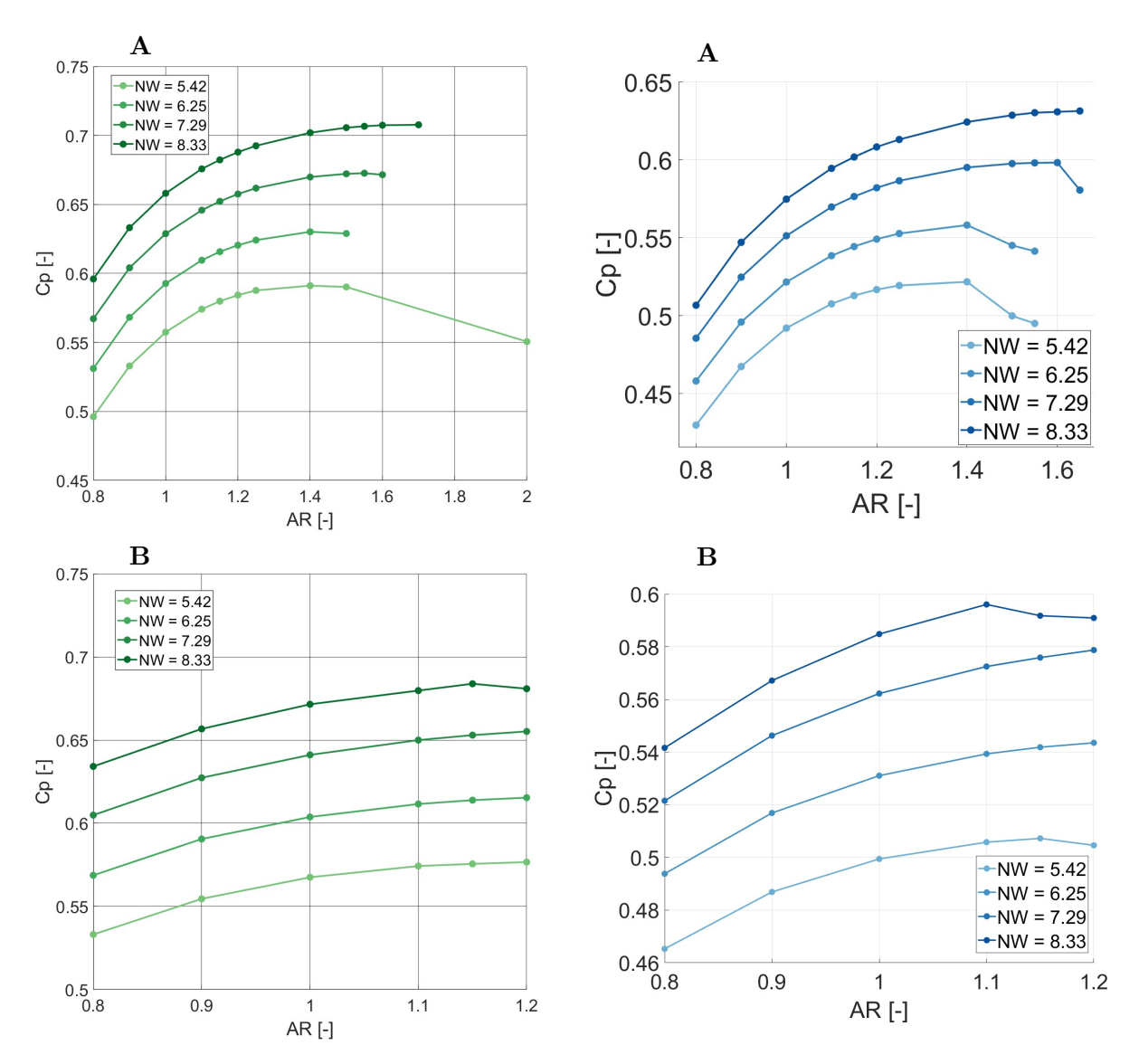


Figure G.1: SC-CO2 (in green) and Air (in blue) flows comparison of CFD results ( $\mathbf{A}$ ) Inlet Alpha =  $70[\deg]$ , ( $\mathbf{B}$ ) Inlet Alpha =  $73.8[\deg]$ .